Ethynyl-1,1’-Biphenyl Derivatives as Amyloid Beta Aggregation Inhibitors

by

Amna El Shatshat

A thesis
presented to University of Waterloo
in fulfillment of the
thesis requirement for the degree of
Master of Science
in
Pharmacy

Waterloo, Ontario, Canada, 2019

Author's Declaration

I hereby declare that I am the sole author of this thesis. This is a true copy of the thesis, including any required final revisions, as accepted by my examiners.

I understand that my thesis may be made electronically available to the public.

Abstract

Alzheimer's disease (AD) is a progressive, neurodegenerative disorder, with characteristic symptoms including memory loss and cognitive decline. AD is characterized by the formation of dense amyloid β (Aβ) plaques and neurofibrillary tangles (NFTs) in the central nervous system (CNS). The amyloid β cascade hypothesis states that an increase in insoluble amyloid β aggregates initiates the neurodegenerative cascade observed in AD. The objective of this project was to design, synthesize and evaluate novel ethynyl-1,1'-biphenyl ring scaffolds in the prevention of $A\beta_{1-40/42}$ aggregation, through the utilization of medicinal chemistry principles. In this regard, the structure-activity relationship (SAR) data for a library of 17 small molecules based on an ethynyl-1,1'-biphenyl compound library (**5a**-**j**, **9a**-**g** and **14**) were obtained. Ethynyl-1,1'-biphenyl derivatives (**5a**-**j**, **9a**-**g** and **14**) with varying steric and electronic properties were synthesized, characterized and screened through anti-$A\beta_{1-40/42}$ aggregation kinetics study and transmission electron microscopy (TEM) experiments to determine their inhibition profile. Lead candidates were identified, and molecular docking studies were conducted to investigate the binding modes of these lead derivatives to understand their binding interactions in Aβ dimer and oligomer models. The most potent $A\beta_{1-40}$ inhibitor was **5i** (4-(4-ethynylphenyl)pyridine; ($A\beta_{1-40}$ inhibition: 79%), followed by **5e** (4'-ethynyl-(1,1'-biphenyl)-4-ol; ($A\beta_{1-40}$ inhibition: ~67%). All the ethynyl-1,1'-derivatives were more potent inhibitors of $A\beta_{1-42}$ aggregation, with compound **9g** ((3'-ethynyl-(1,1'-biphenyl)-4-yl)(methyl)sulfane) exhibiting greater inhibitory activity (($A\beta_{1-42}$ inhibition: ~87 %), closely followed by **5i** (4-(4-ethynylphenyl)pyridine; ($A\beta_{1-40}$ inhibition: 86 %). These investigations demonstrate that biphenyl ring templates with ethynyl-substituents possess anti-Aβ aggregation properties, which can be useful to study Aβ aggregation and also may serve as useful templates in designing novel class of anti-AD agents.

Acknowledgements

I would like to thank the Faculty of Science, Office of Research, the School of Pharmacy at the University of Waterloo, NSERC-Discovery, Canada Foundation for Innovation (CFI-JELF), Ontario Research Fund (ORF) and Early Researcher Award, Ministry of Research and Innovation, and the Government of Ontario, Canada for financial support of this research project.

I would like to express my deep gratitude to my supervisor, Dr. Praveen P. Nekkar Rao, for his valuable support, encouragement, and enthusiasm during the planning and development of this work. His willingness to give his time and energy so generously has been greatly appreciated. I would also like to extend my appreciation to my committee advisors, Dr. Gary Dmitrienko and Dr. Tejal Patel. Thank you for your guidance and patience throughout this project.

I would also like to extend my thanks to my lab members and fellow grad students for their constant motivation, their support throughout this project, and for always keeping me laughing.

Finally, a special thanks to all my loved ones for their constant care and strength. None of this would have been possible without you.

Table of Contents

List of Figures

Chapter 1

Chapter 2

Chapter 3

Chapter 4

List of Tables

Chapter 4

List of Abbreviations

^1H NMR = Proton NMR

Aβ = Amyloid-β protein

ACID = APP intracellular domain

ACh = Acetylcholine

AChE = Acetylcholinesterase

AD = Alzheimer's disease

ADAM = Disintegrin and metalloproteinase

ADL = Activities of daily life

ADRDA = Alzheimer's Disease and Related Disorders Association

AICD = Amyloid precursor protein intracellular domain

APH-1 = Anterior pharynx defective 1

APP = Amyloid precursor protein

BACE = Beta-site APP cleaving enzyme

BBB = Blood brain barrier

BPT = Biphenyl-3,3',4,4'-tetrol

BuChE = Butyrylcholinesterase

CAA = Cerebral amyloid angiopathy

ChAT = Choline acetyltransferase

ChE = Cholinesterase

cLogP = Partition coefficient

CNS = Central nervous system

COX = Cyclooxygenase

DCM = Dichloromethane

DMSO = Dimethyl sulfoxide

DSM-IV-TR = Diagnostic and Statistical Manual of Mental Disorders, fourth edition

EGFR = Epidermal growth factor receptor

FCSRT = Free and Cued Selective Recall Reminding Test

^{18}FDG = ^{18}fluorodeoxyglucose

FTD = Fronto-temporal lobar degeneration

GB = Grober-Buschke

HPLC = High performance liquid chromatography

IWG = International Working Group

LC-MS = Liquid chromatography mass spectrometry

MCI = Mild cognitive impairment

MP = Melting point

MMSE = Mini-Mental State Examination

MoCA = Montreal Cognitive Assessment

MS = Mass spectrometry

MRI = Magnetic resonance imaging

MTA = Medial temporal lobe atrophy

NFT = Neurofibrillary tangles

NIA-AA = National Institute on Aging-Alzheimer's Association

NINCDS-ADRDA = National Institute of Neurological and Communicative Disorders and Stroke-Alzheimer's Disease and Related Disorders Association

NMR = Nuclear magnetic resonance

NMDA = N-methyl-D-aspartate

NRG1 = Neuregulin-1

NSAIDs = Nonsteroidal anti-inflammatory drugs

PEN-2 = Presenilin enhancer 2

PET = Positron emission tomography

PFC = Prefrontal cortex

PiB = Pittsburgh Compound B

PS1 = Presenilin1

PS2 = Presenilin 2

p-tau = Phosphorylated tau

RBF = Round-bottom flask

RFUs = Relative fluorescence units

ROS = Reactive oxygen species

s-APPα = Soluble APP α protein

s-APPβ = Soluble APP β protein

SAR = Structure-activity relationship

SPECT = Single photon emission computed tomography

TEM = Transmission electron microscopy

THF = Tetrahydrofuran

ThT = Thioflavin T

TLC = Thin-layer chromatography

t-tau = Total tau

UPW = Ultra pure water

List of Schemes

Chapter 1

Chapter 3

Chapter 1: Introduction

1.1 Background on Alzheimer's Disease

Over the course of the twentieth century, the life expectancy of the world's population has increased and correspondingly, a surge in senile dementia has been observed.[1] Approximately 40 million individuals worldwide are afflicted with dementia, and it is presently one of the largest health care challenges.[1, 2] Alzheimer's disease (AD) is the most common neurodegenerative disorder, accounting for 60% of dementia cases, with over half a million Canadians identified to be living with AD.[3, 4] This amount is estimated to double every 20 years until 2050.[2] It is further estimated that the number of individuals afflicted with AD, or other dementias, will continue to grow, as the population of North Americans aged 65 years or older is expected to double from 48 million to 88 million by 2050.[1, 5] In the past decades, AD and dementia has become a critical public health issue, causing a significant increase in economic, health and social care costs.[6]

Consequently, priority has been given toward understanding and developing strategies in an attempt to prevent and treat AD and dementia. Dementia is an umbrella term, defined as a wide range of symptoms related to memory decline, in addition to impairment observed in communication and cognition.[7] To have AD, one must exhibit this cognitive impairment, which gradually interferes with the ability to function, and/or activities of daily life (ADL), and is accompanied by a decline from a previously functioning baseline.[5, 8] It is important to note that this cognitive impairment and decline is not caused by other factors, including delirium or a psychiatric disorder, and that AD diagnosis is typically conducted through the exclusion of other health conditions.[8] Therefore, AD diagnosis should not be applied if there is substantial evidence of vascular dementia caused by cerebrovascular disease, dementia with Lewy bodies, or fronto-temporal lobar degeneration (FTD).[5, 8] As previously mentioned, AD is the most common form of dementia, with pathological features including senile plaques, neurofibrillary tangles (NFTs), and cerebral atrophy.[9] AD is the most common cerebral proteopathy; however, it is only through autopsy findings that one can conclusively confirm the presence of AD, based on the accumulation of senile plaques and NFTs in a patient's brain.[5, 8] Currently, clinical assessment is the major tool used to diagnose AD.[8, 10]

The neuritic senile plaques seen in AD brain are composed of extracellular deposits of amyloid β proteins (Aβ), which are deposited in the grey matter of the brain. In addition, NFTs are hypothesized to be composed of abnormally hyperphosphorylated tau protein; a microtubule-associated protein found in neuronal axons.[5, 8] A number of studies involving human AD patients and transgenic mice models have demonstrated that early accumulation of Aβ protein and hyperphosphorylated tau protein can trigger other adverse down-stream effects including: mitochondrial dysfunction,[10, 11] microgliosis and astrocytosis,[12] free radicals formation, oxidative stress and hyperphosphorylation of tau protein,[12, 13] synaptic dysfunction and neurotransmitter deficits,[12,14] ultimately resulting in cognitive decline.[12, 13, 15]

First-generation therapies for AD involved the development of cholinesterase (ChE) inhibitors, based on the well-studied cholinergic hypothesis.[16-18] The cholinergic hypothesis states that AD pathology is observed due to an overall deficiency of a central neurotransmitter, acetylcholine (ACh).[17] The cholinergic pathway involves cognitive function and ACh is often used by sympathetic and parasympathetic neurons. Through the choline acetyltransferase (ChAT) enzyme, ACh is synthesized and released into the synaptic cleft wherein, it binds to muscarinic and/or nicotinic ACh receptors, initiating different neurotransmission cascades.[19, 20] This ACh is hydrolyzed by cholinesterase enzymes to release choline, which is recycled for ACh synthesis.[20]

The cholinesterase enzyme exists as two isoforms: acetylcholinesterase (AChE) and butyrylcholinesterase (BuChE).[20] Hippocampal ACh plays a significant role in memory function, with evidence including, but not limited to, the upregulation of ChAT during special memory tasks, and ACh levels within the hippocampus are associated with memory function, wherein, age-related cognitive decline also correlates to a decrease in this hippocampal ACh.[19, 21-23] In postmortem brains of AD patients, there is a significant decline in ACh concentrations, and it was hypothesized that this decline in cholinergic neurotransmitter activity results in an overall increase in impaired cognitive function.[21, 24] As a result, the cholinergic hypothesis for AD was developed, and it remains the oldest and most studied hypothesis for pathogenesis of AD.[20] The hypothesis indicates that there is an increased rate of ACh degradation in the cholinergic region of the brain, due to an increase in cholinesterase activity.[21, 22] This led to the development of therapeutics to treat AD patients with cholinesterase inhibitors (ChEIs) which are capable of increasing ACh concentrations, thus promoting ACh-mediated neurotransmission.[19] Current marketed AD therapies include donepezil, rivastigmine and galantamine, all of which are ChE inhibitors.[25] Another drug used in AD therapy is memantine, which is an N-methyl-D-aspartate (NMDA) receptor antagonist. All these therapies act to stabilize cognitive performance in AD patients. However, they fail to show improvements in AD patients in the long-term and generally provide a short period of symptomatic relief.[20, 25] Unfortunately, there is not a single therapeutic which can either prevent the disease progression or offer a potential cure for AD. These factors, coupled with an aging population and increasing life span, will contribute in increasing the prevalence of AD.[26]

1.2 Amyloid Hypothesis

The pathophysiology of AD is highly complex, and while various hypotheses have been posited to explain this perplexing disease, our collective understanding of AD pathogenesis is very limited. Through studying the physical and behavioral patterns of AD patients, various hypotheses have been suggested to describe the pathological route of the disease.[7, 26] Among the various AD hypotheses, the Aβ cascade hypothesis has been put forth, wherein an increase in insoluble Aβ aggregates initiate the neurodegenerative cascade observed in AD.[17, 26] This Aβ cascade hypothesis has provided the basis for which much of current AD research is built on.

In AD, cognitive decline is observed in patients as a result of multiple factors, including: synaptic loss, an increase in inflammatory signaling, an accumulation of neuritic senile plaques and NFTs, which results in overall neuronal deterioration.[7, 17, 26, 27] These neuritic senile plaques are composed of extracellular deposits of Aβ proteins (A$\beta_{1\text{-}40/42}$), that are deposited in the grey matter of the brain.[5, 7, 17, 26, 27] A number of studies involving human AD patients and transgenic mice models have demonstrated that early accumulation of this extracellular deposit of Aβ protein can trigger other adverse down-stream effects including, mitochondrial dysfunction,[10, 11] microgliosis and astrocytosis,[12] free radicals formation, oxidative stress, hyperphosphorylation of tau protein,[12, 13] synaptic dysfunction and neurotransmitter deficits,[12, 14] ultimately resulting in cognitive decline.[12, 13, 15]

1.2.1 Amyloid precursor protein

Amyloid precursor protein (APP) is a highly conserved, integral protein expressed in the synapse of neuronal tissue.[17] APP cleavage results in the release of amyloid β (Aβ) protein, the main component of senile plaque formation, and thus, APP has been studied predominately for its role in Aβ protein production.[17, 28] APP is a constitutively expressed glycoprotein, with various isoforms found throughout the body. The primary role for APP is not fully understood. It has a range of physiological roles including, neuritogenesis, glucose homeostasis, synaptogenesis, neuroprotection, and regulation of intracellular signaling.[24, 29-33] While many isoforms exist throughout the body, APP is highly expressed in neuronal and glial cells in the CNS, with physiological roles involving cell adhesion and metal ion homeostasis, all of which contribute to the maintenance of neuronal plasticity and synapse formation.[17, 28] The gene for APP is located on chromosome 21, and alternative splicing yields various isoforms of the protein, ranging in length from 695 to 777 amino acids.[28, 33] APP is a large transmembrane protein, with a larger extracellular domain. However, the first proteolytic cleavage of APP occurs in the transmembrane region.[17]

1.2.2 APP Metabolism and Processing

APP undergoes transmembrane cleavage, via a series of secretase enzymes, to produce soluble monomeric Aβ peptides.[17] These monomeric Aβ peptides aggregate to form insoluble toxic fibrils that accumulate in the brain and induce inflammatory responses to activate neurotoxic pathways, ultimately resulting in neuronal cell death.[17, 34, 35] Specifically, these neurotoxic Aβ peptides are produced through cleavage of BACE-1 and γ-secretase on APP. The transmembrane proteolytic enzyme cleavage of APP generates one of two species: soluble and non-toxic peptides, via the non-amyloidogenic metabolic pathway, or the neurotoxic Aβ peptides, via amyloidogenic metabolic pathway (Figure 1.1).[17, 27, 34, 35]

The non-amyloidogenic metabolic pathway is a constitutive secretory pathway. It is also the predominant pathway involving the α-secretase enzyme, which cleaves this transmembrane APP protein to release the soluble APP α protein (s-APP α),[17, 27, 34, 35] as displayed in Figure 1.1. The s-APPα protein is observed to play a role in development, with exhibited neurotrophic and neuroprotective properties, as well as growth promoting functions. However, the exact mechanism of actions for s-APPα is not fully understood.[17, 34, 36] Previous studies have also indicated that the overexpression of α-secretase activity reduces amyloidogensis, or the accumulation of neurotoxic Aβ species.[17, 27, 34, 35] This cleavage also releases another protein fragment, termed CT83 peptide, which is not observed to have neurotoxic properties. This CT83 is further cleaved via γ-secretase to release the P3 peptide and the amyloid precursor protein intracellular domain (AICD), which are involved in normal metabolic pathways (Figure 1.1).[17, 27, 34, 35] This P3 fragment degrades rapidly, and is widely accepted to have minor functionality.[37]

In contrast, the amyloidogenic pathway involves the enzyme β-site APP cleaving enzyme 1 (BACE-1) and γ-secretase cleavage of APP. BACE-1 competes with α -secretase for the same location, however BACE-1 is observed to have a range of substrates.[38] Further, BACE-1 expression increases during cellular stress, or oxidative stress.[38, 39] In the amyloidogenic pathway, BACE-1 initially cleaves APP to release another soluble APP protein, termed s-APPβ.[27, 34] Unlike s-APPα protein, s-APPβ has no observable neurotrophic or neuroprotective properties, and cleaving this protein produces the CT99 peptide. This CT99 peptide contains the neurotoxic Aβ peptide, and upon γ-secretase activity, a 4 kDa amyloid peptide ($A\beta_{1\text{-}40/42}$) and AICD is liberated (Figure 1.1).[17, 27, 34, 35] While AICD is liberated from both amyloidogenic and non-amyloidogenic pathways, the length of this AICD peptide varies, although still maintaining the consensus motif required for binding to different adapter proteins.[37, 40] AICD is observed to participate in an array of biological actions, however a clear role for the AICD domain has not been established outside of its role as a domain within the full length APP protein.[37] This observation has been extended towards the other domains within the full length APP protein, indicating that the various domains have higher biological activity together within the APP protein, rather than on their own.[41]

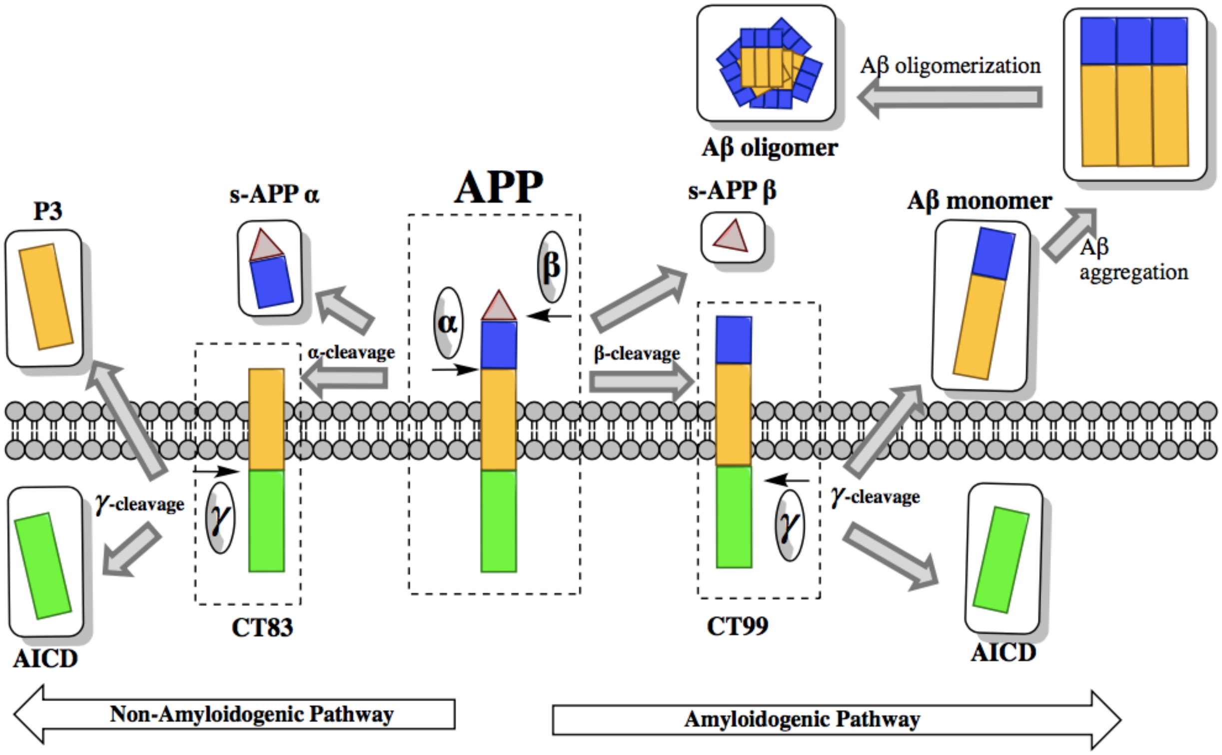

Figure 1.1. APP processing and cleavage products. Amyloidogenic and non-amyloidogenic APP processing pathways are displayed. The non-amyloidogenic pathway involves α-secretase and γ-secretase activity to release products s-APPα, AICD, and P3. The amyloidogenic pathway involves β-secretase and γ-secretase activity to release products s-APPβ, AICD, and toxic Aβ monomers that aggregate to form neurotoxic species leading to AD pathology.

1.2.3 Secretase Enzymes

APP α-secretase cleavage occurs constitutively, and α-secretase activity is associated with a family of proteins, known as disintegrin and metalloproteinase (ADAM) proteins.[42] ADAM proteases are membrane bound or secreted proteins of the metzincin family, containing a prodomain, a metalloproteinase domain, a disintegrin domain, a cysteine-rich region, and an epidermal growth factor repeat region.[42] Proteins within the ADAM family are involved in the activation of many signalling pathways, and while α-secretase acts upon APP, it also acts on other substrates, including notch, cadherin, and tumor necrosis factor-α.[43-45]

Moreover, β-secretase activity is directed by BACE-1, which cleaves APP to release s-APPβ and produce CTF99.[36] Interestingly, β-secretase activity is found throughout the body, and within majority of cells and tissues. However, highest concentrations of BACE-1 are observed in neural tissues.[36, 46] In addition, BACE-1 shares a homologue, BACE-2, and the two share approximately 64% amino acid similarity.[46] While both β-secretase homologue mRNAs are expressed throughout the body, BACE-2 mRNA is expressed in low levels and is untraceable in the brain; whereas, BACE-1 mRNA is expressed highest within the brain and pancreas.[46] In addition, BACE-1 mRNA expression is observed at a higher rate along with a large increase in BACE-1 protein in AD patient brains.[47] Similar to α-secretase, BACE-1 acts on substrates other than APP, and while the physiological role of this protein is still unclear, studies have identified proteins neuregulin-1 (NRG1) and voltage-gated sodium channels (VGSCβ subunits) which are involved in the regulation of neuronal function as BACE-1 substrates.[46, 47]

The γ-secretase enzyme is involved in the final cleavage of APP in both amyloidogenic and non-amyloidogenic pathways. It is a multi-subunit protease complex, belonging to a family of intramembrane cleaving proteases. Accordingly, γ-secretase cleaves within the intra-membrane region of APP to release $A\beta_{1-40/42}$ or p3 and AICD.[48] Hence, γ-secretase requires at least four proteins to come together for the any activity to be observed.[48] These four domains include presenilins (PS1 or PS2), nicastrin, anterior pharynx defective 1 (APH-1), and presenilin enhancer 2 (PEN-2).[37] PS1 and PS2 play a key role in the protease activity, with PS1 representing the major presenilin in the brain.[40] The four domains cross-regulate one another, wherein, a deficiency in one domain causes the destabilization of other domains, thus, altering the production and trafficking of the other domains.[41] Over fifty γ-secretase substrates have been identified, including APP, notch, the neuregulin binding partner ErbB4, and N-cadherin, to name a few.[40, 41, 48, 49]

1.2.4 Aβ Peptide

The amyloidogenic pathway involves the cleavage of APP via β-secretase and γ-secretase to produce the Aβ peptide, which is the main component of senile plaques. While different isoforms of this protein exist within the brain, this neurotoxic 4 kDa Aβ peptide is often cleaved in the form of $A\beta_{1\text{-}40}$, with the release of $A\beta_{1\text{-}42}$ occurring less frequently.[17, 27, 34, 35] While isoform $A\beta_{1\text{-}40}$ differs from $A\beta_{1\text{-}42}$ by two amino acids at the C-terminal, the properties differ, in that, $A\beta_{1\text{-}42}$ is more insoluble and prone to aggregation at a faster rate than $A\beta_{1\text{-}40}$.[17, 27, 34, 35] Although the size of these released Aβ peptides may differ slightly, there are important domains within the peptide sequence that remains constant, which are also essential in AD pathogenesis. Within the sequence exists a metal-binding domain, near the N-terminus; a hydrophobic domain, referred to as the site of aggregation; and a larger hydrophobic domain near the C-terminus.[50-52] The metal binding domain undergoes interactions with copper and iron metals, and this metal coordination increases the redox chemistry within the brain, thus, increasing the production of reactive oxygen species (ROS).[53] The site of aggregation, or the KLVFFA domain, is a hydrophobic sequence that has been extensively studied and identified to drive the aggregation process to form various forms of Aβ species, including oligomers and fibrils.[52] The hydrophobic domain located at the C-terminus has also been identified to drive the fibrillogenesis to form higher order Aβ species, thereby facilitating the maturation of oligomer species into fibrils.[50, 52] Monomeric $A\beta_{1\text{-}40/42}$ peptides aggregate to form insoluble toxic fibrils that accumulate in the brain and induce inflammatory responses and activate neurotoxic pathways, resulting in neuronal cell death.[54-56]

$A\beta_{1-40/42}$ peptides can take on many forms, starting with the soluble monomeric form (Figure 1.2). The aggregation pathway of $A\beta_{1-40/42}$ peptides is similar to that of other amyloidogenic proteins.[20] At higher concentrations, the biochemical properties of the peptide allows for self-assembly; wherein the monomeric Aβ attaches to one another to form larger soluble aggregates, like dimers and oligomers; and these aggregates grow to form insoluble protofibrils and finally, mature fibrils.[35] These insoluble mature fibril aggregates are the main component of dense and insoluble neuritic senile plaques.[26]

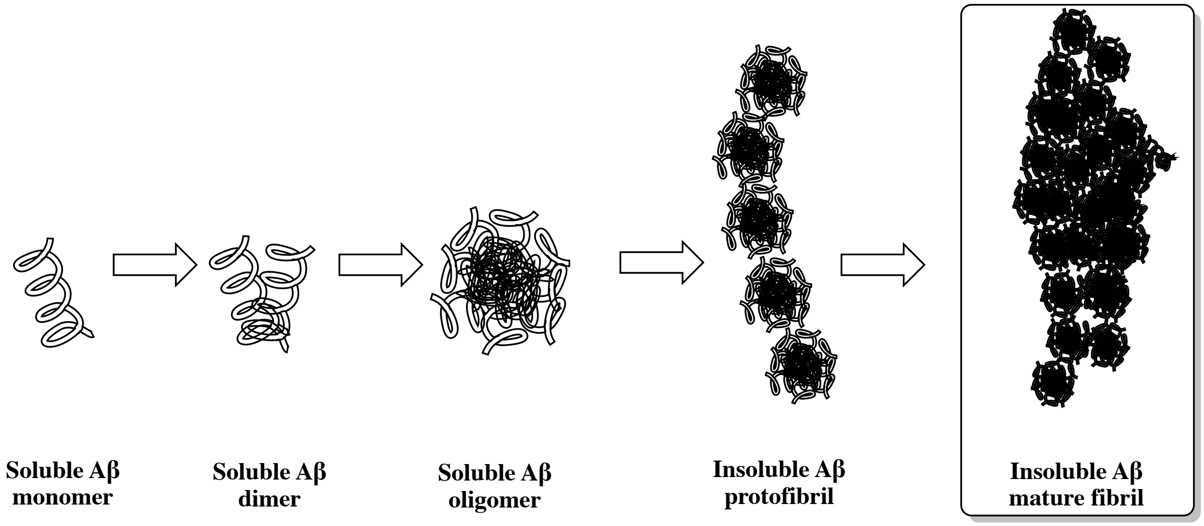

Figure 1.2. Aggregation pathway of soluble Aβ monomers to insoluble Aβ fibril.

Interestingly, there is a multitude of Aβ species that exist, wherein prefibrillar multimers, or oligomers, of complexes ranging from dimers to 24-mers have been identified.[35] These oligomers are classified as low molecular weight oligomers, consisting of less than 8 Aβ subunits, and high molecular weight oligomers, with Aβ aggregates approximately 42 kDa to 1 mDa in molecular weight.[35] Protofibrils, composed of β-sheets, are more ordered than smaller oligomers and are considered to be high molecular weight oligomers, appearing as twisted threads on electron microscopy. Protofibrils are substructures of fibrils, and these insoluble fibrils end the aggregation process.[35] Among various Aβ species, soluble oligomeric are noted to be the more neurotoxic species, inhibiting many critical neuronal functions.[34, 35] Recent studies have pointed to this prefibrillar Aβ oligomer species as the major intermediate in the neurodegeneration observed in AD patients.[34, 35] These mechanism of Aβ oligomer formation *in vivo* is still unclear, and multiple complex Aβ oligomer conformations has led to the hypothesis that many different pathways produce these Aβ species.[34, 35] Of these different pathways, extracellular Aβ oligomer formation is one that has been studied extensively. Extracellular Aβ oligomers can interact with GM1 ganglioside, a sphingolipid involved in the regulation of developing and mature neurons, and induce neuronal cell death mediated by nerve growth factor (NGF) receptors.[57, 58] Further, Aβ oligomers have been observed to bind NMDA-type glutamate receptor (NMDAR), resulting in disrupted calcium homeostasis; this ultimately leads to an increase in oxidative stress and synaptic dysfunction.[59, 60] More simply, membrane pores can be formed by Aβ oligomers, causing cell membrane destabilization via an increased flow of ions across the membrane.[61, 62] While extracellular Aβ species have been noted as the main component of extracellular neuritic senile plaques, the identification of intracellular Aβ proteins has been debated. However, studies have indicated the generation of intracellular Aβ species via intracellular production within endoplasmic reticulum and trans-Golgi network. This generation is through the cleavage of APP in endosomes, generated from the endoplasmic reticulum; or the re-entry of extracellular Aβ species through various receptors and transporters; as well as an accumulation of Aβ species in lysosomes within AD patient brains.[63-65] These noted pathways can result in the existence of intracellular Aβ species within the cytosolic compartment. While the toxicity mechanisms for intracellular Aβ oligomers remains unclear, it has been suggested that interactions of Aβ species with other biomolecules, such as molecular chaperones and lipids, can result in neurodegeneration.[63, 64]

It is important to note, however, that the monomeric Aβ species itself is not toxic.[66, 67] The neurotoxicity arises through the formation of the β-sheet structure in Aβ oligomers.[66, 68] The Aβ monomeric species consists of a string of aromatic residues that are involved in pi-stacking interactions. These pi-stacking interactions have been suggested to be fundamental for the self-assembly of the Aβ species, thus enhancing the fibrillogenesis.[68] Non-AD individuals produce this monomeric Aβ species, albeit at lower concentrations than AD patients, and with a clearance rate higher than that of its production rate.[67] At this low picomolar concentration, which is typical under normal physiological conditions, Aβ monomers have been identified to play many biological roles, including aiding in neuronal growth and glucose metabolism.[69-72] Further, under normal physiological conditions, Aβ concentrations are maintained at optimal levels; wherein, Aβ species are cleared through transport mechanisms or degraded via peptidase action or microglial-mediated degradation.[73, 74] Monomeric Aβ species can undergo misfolding, triggering a self-induced aggregation process leading to the formation of higher order toxic Aβ species.[59, 66] Native, unfolded Aβ monomers exist as random coils and, as aggregation proceeds, a conformational transition from random coil and α-helix to β-sheet is observed.[52] This misfolding occurs through various hydrophobic interactions and metal coordinating interactions, which allows for the stabilization of this misfolded complex. The dimerization of this complex, however, occurs more readily than the monomeric misfolded native Aβ species, as it is more energetically favourable.[52] The dimeric species quickly recruits more misfolded Aβ monomers to form low molecular weight oligomers, and continues to recruit to form larger protofibrils.[52]

Various techniques have been developed in order to determine the morphology and structural conformation of different Aβ species. These different aggregated Aβ species can be visualized via microscopic techniques, including light microscopy, electron microscopy, and atomic force microscopy. Of these microscopic techniques, electron microscopy is often employed in order to study plaque morphology, as well as to obtain structural information of higher order aggregated Aβ species.[35] Similarly, techniques have been further developed in order to determine the kinetic characteristic of Aβ species, based on spectroscopy. Various techniques based on fluorescence microscopy allow for the observation of the Aβ fibrillization process in real time. These techniques include, but are not limited to, turbidity measurements, thioflavin T (ThT) and Congo Red dye based assays.[35]

In healthy individuals, both non-amyloidogenic and amyloidogenic pathways occur as a part of normal metabolism, with the non-amyloidogenic pathway occurring more frequently, as well as efficient clearing of the $A\beta_{1\text{-}40/42}$ peptides products from the amyloidogenic pathway.[7, 26] However, there occurs an imbalance in the APP metabolic pathways, resulting in a disproportionate amount of $A\beta_{1\text{-}40/42}$ peptides produced and cleared. This shift from the non-amyloidogenic to amyloidogenic pathway is the main cause for the increased accumulation and subsequent aggregation of $A\beta_{1\text{-}40/42}$ peptides.[7, 20] The cause for this shift is still unclear; however, various biochemical events, such as decrease in Aβ-degrading enzymes and an increase in the action of receptors responsible for shuttling soluble Aβ species into the extracellular space from blood stream, may play a role in this shift.[50, 73]

1.3 AD Causes and Risk Factors

In the past decade, AD research has repeatedly produced evidence for both, the misfolding of Aβ protein, as well as tau protein, as causative agents for neuritic senile plaque and NFT formation. Evidence from clinical, observational and pathological studies have highlighted the complexity of this disorder, as well as the multifactorial nature of AD.[2]

1.3.1 Genetic Factors

AD cases can be divided into categories depending on type of onset and family history. First, AD is divided into early-onset form, wherein individuals younger than 60 – 65 years are affected; or late-onset form, with individuals older than 60 – 65 years.[5] Depending on family history, AD cases are further classified as familial, autosomal dominant, or sporadic.[5] Familial AD studies provide the strongest evidence for Aβ and tau proteins as causative agents for AD pathology.

Although most cases of AD are late-onset and sporadic, familial AD is a rare form of AD, accounting for less than 5% of all AD cases, with an early-onset and symptoms developing much earlier than typical AD.[5] Through mutations in one of three genes related to APP, PS1 and PS2; AD is infrequently inherited as an autosomal dominant. As stated in earlier sections, these proteins are involved in APP processing. The mutations within these domains affect Aβ cleavage and aggregation. The γ-secretase requires four proteins to come together in order to function, with PS1 and PS2 acting as subunits for γ-secretase.[48] PS1 and PS2 play a key role in the protease activity, and as mentioned previously, deficiency in one domain causes the destabilization of other domains.[40] PS1 mutations occur more frequently than PS2 mutations, and accounts for the majority of autosomal dominant cases.[75] Mutations within the APP gene, on chromosome 21, are found within or near the short Aβ coding domain on the gene, clustering the β- and γ-cleavage sites. These mutations may enhance β-secretase activity or modify γ-secretase cleavage, resulting in an increase in Aβ protein production.[76, 77] Other APP mutations involve increasing the production of AICD, or other C-terminal proteins, causing a disruption in intracellular mechanisms leading to apoptosis.[77] Contrasting to APP, PS1 mutations are located throughout gene, and it has been hypothesized that it is through this loss in functionality of the γ-secretase protein, does AD pathogenesis occur.[78] As mentioned in earlier sections, γ-secretase can act on an array of substrates, and this loss in functionality due to mutations within PS1 or PS2, may cause a variety of toxic outcomes.[77] All APP and PS mutations have negative implications on APP metabolism and Aβ processing, resulting in an increase in Aβ peptide production. Limited familial AD studies to date have shown an increase in soluble and insoluble $A\beta_{1\text{-}42}$ peptide in genetic AD brain tissue, in comparison to sporadic AD brain tissue.[79-81] Further, APP mutations are also associated with severe cerebral amyloid angiopathy (CAA), resulting in cerebral haemorrhage or stroke.[26] In some cases, CAA is also observed in individuals with PS mutations, although less frequently.[26]

Early in the 1990s, a link between late-onset AD and the *APOE* gene was identified.[82, 83] Since, the gene has been studied extensively and is associated with late-onset AD pathogenesis.[82, 83] Late-onset AD has a large genetic component, with heritability estimates of 58 – 79%.[84] *APOE* gene codes for apolipoprotein E, a lipoprotein found prominently in the brain that associates with cholesterol and phospholipids, and is responsible for lipid transport and cholesterol homeostasis.[85] Three common alleles of *APOE* include, *ε*2, *ε*3, *ε*4; and these correspond to six different phenotypes.[5] The *ε*4 allele is associated with AD, wherein the presence of this allele increases the risk, as well as reduces the age at onset of AD.[5] For example, individuals that are homozygous carriers of two *APOE* ε4 alleles have a higher risk and earlier onset than heterozygous individuals, however, *APOE* ε4 allele is neither necessary nor sufficient for developing AD.[5, 84] Studies have indicated the association of the *APOE* ε4 allele with blood brain barrier (BBB) disruption, as well as cholesterol dysregulation.[86, 87] There has been an emphasis on the importance of cholesterol in many cellular mechanisms and its effect on increased Aβ production.[89] In addition, the APOE ε4 isoform has been implicated in the amplification of detrimental pathways due to its interference on Aβ clearance, as well as modulating Aβ induced effects on inflammatory receptor signaling.[87-89]

1.3.2 Environmental Factors

While extensive research on genetic factors has been conducted, majority of AD cases have no genetic basis.[5] What has been understood is that AD is a multifactorial disorder, with an interplay of various environmental factors that come together to play a role in sporadic AD. The most established risk factor is increasing age, although ageing is not necessarily a direct cause of AD.[90] Many studies have shown an exponential increase in AD incidence rates between the ages of 65 and 85 years, followed by a cumulative decreased risk of developing AD for men; whereas, women are associated with a higher relative risk.[90]

Other modifiable risk factors have been identified, including vascular and metabolic disorders.[5] Epidemiological and clinical studies have suggested that high levels of serum cholesterol, as well as raised blood pressure, increase the risk of developing AD later in life.[91, 92] Various links between cellular mechanisms and pathways related to hypertension or hypercholesterolemia and AD pathology have been identified. Vascular changes caused by these pathways can lead to cerebral hypoperfusion or these changes can converge to trigger the neurodegenerative pathways observed in AD pathology.[91, 92] It has also been noted that obesity, diabetes, and impaired glucose tolerance increase the risk of developing dementia.[91, 92] The vascular hypothesis suggests that cerebrovascular disease can add to the severity of AD, wherein various vascular risk factors are involved in the neurodegeneration and progression of AD.[91, 92] This hypothesis, like many AD hypotheses, is a debatable one, as both cerebrovascular disease and AD exist in elderly patients.[91, 92] Another interesting hypothesis is the cognitive reserve hypothesis, wherein an increase in mental, social and physical activity levels correlate to a decreased risk of AD.[93] The hypothesis suggests that brain stimulation through educational tools can lead to a more flexible use of neuronal networks, as well as life style components like stimulating environments and physical activity, can act as protective factors against AD.[93]

The number of risk factors suggested continues to increase as new knowledge gets accumulated on this complex disorder. Migraines, increased intake of saturated fat, high serum homocysteine, fibrinogen concentrations, peripheral inflammation, atrial fibrillation, and head injuries are just a few that have been identified.[94-100]

1.4 Clinical Diagnosis

Initially, AD was defined as a clinical-pathological disorder: only diagnosed in life as probable AD and definitively diagnosed after death. While pathologic AD findings may assist with diagnosis, ultimately, AD dementia is a clinical diagnosis that requires accurate and timely diagnosis.[101]

1.4.1 First Approach and Neuropsychological Evaluation

Clinical diagnosis of AD relies on patients' history, neuropsychological testing, and symptom assessment at the time. AD dementia clinical diagnosis can reach an accuracy rate of 95%, when established by experienced clinicians with comprehensive follow up.[5] This rate decreases, however, outside of specialized centers, wherein the presence of co-morbidities, inaccurate self-reporting, and a lack of information related to patients' previous baseline cause diagnoses to be more unreliable.[5]

In 1984, the first criteria for AD diagnosis was proposed by National Institute of Neurological and Communicative Disorders and Stroke (NINCDS) and the Alzheimer's Disease and Related Disorders Association (ADRDA), termed the NINCDS-ARDRA original criteria.[102] The criteria includes tiers of probability for AD diagnosis, with the highest tier referred to as "definite AD," involving autopsy confirmation; the second tier as "probably AD," defined by progressive amnestic disorder with dementia that affect two areas of cognition and functional impairment, without other causes identified; and the last tier, "possible AD," as progressive amnestic disorder with dementia, that may have other factors contributing to this observed cognitive impairment.[8,102] This original criteria utilizes patients' medical history, clinical examination, neuropsychological testing, and laboratory assessments for reliable AD diagnose.[102] Clinical tests should, ideally, identify patients with a disorder correctly, as well as correctly identify patients without the disorder.[103] The sensitivity of a clinical test demonstrates the ability to identify patients with the disorder correctly. Similarly, the specificity demonstrates the ability of a clinical test to correctly identify patients without the disorder.[103] Throughout over a dozen clinical pathological studies, the sensitivity of the NINCDS-ARDRA original criteria was observed to be 81%, with a specificity 70%.[104]

AD diagnosis is also based on criteria found in the Diagnostic and Statistical Manual of Mental Disorders, fourth edition (DSM-IV-TR). Similar to the NINCDS-ARDRA criteria, criteria found in DSM-IV-TR include deficits in memory and another cognitive domain. In addition, the DSM-IV-TR emphasizes the requirement for these deficits to cause an impact on social function or activities of daily life (ADL).[5] Several screening tools to detect dementia are available and the Mini-Mental State Examination (MMSE) is a popular one.[105] The MMSE is a neuropsychological test assessing memory, executive functions, language, praxis, visuo-spatial abilities.[105] However, issues have arisen with difficulties in the MMSE in detecting early dementia.[105]

AD diagnosis is based on criteria identified by these two sources. However, AD cases are often discovered late in the disorder's progression. As a result, in 2011, revision of the NINCDS-

ARDRA criteria was conducted by the National Institute on Aging and Alzheimer's Association (NIA-AA). The NIA-AA was able to create a new set of diagnostic guidelines for the prodromal stages of AD, in other words, the long pre-dementia clinical stage of AD. During the preclinical phase of AD, it is observed that patients experience a long asymptomatic phase, characterized by normal cognitive ability, with the occurrence of neuropathological changes, which are much more difficult to detect.[6] This preclinical phase is followed by a pre-dementia phase, involving the symptomatic stage of increased cognitive impairment, ultimately leading to the characteristic symptoms of functional impairment in overt dementia. Mild cognitive impairment (MCI) refers to the state preceding dementia, in between normal cognitive aging and dementia, wherein ADL is normal.[105] MCI exists as a mixed entity, including both AD patients, as well as patients with cognitive impairment related or unrelated to other neurodegenerative causes. Studies in the neuropathology and imaging of AD support the transient nature of MCI, and so, further characterization of MCI subtypes have been created. Prodromal AD is one of these subtypes, referring to the individuals who are observed to be on the AD spectrum of clinical disease.[5] The criteria for prodromal AD involves experiencing consistent episodic memory disturbance, as well as biomarker positivity. Biomarker positivity criteria can be obtained via structural imaging, cerebrospinal fluid (CSF), molecular imaging or the knowledge of a dominant mutation within immediate family.[5]

Neuropsychological evaluation via standardized testing is utilized to identify and characterize MCI patients. However, due to lack of access to these tests, or to tertiary care memory clinics, identifying MCI patients becomes difficult.[105] The Montreal Cognitive Assessment (MoCA) was developed as an additional screening tool to identify patients who perform within the normal range on the MMSE, however present traits found for MCI patients.[105] The MoCA neuropsychological test incorporates assessing executive functions, higher-level language abilities, and complex visuospatial processing, which can be mildly impaired in MCI patients.[105] In contrast to MMSE, the MoCA tests involve fewer learning trials, more demanding tasks, and a longer delay before recall; all of which have increased the sensitivity of the MoCA screening tool to diagnose MCI.[105] Differentiating MCI from dementia, conclusively, depends on ADL impact.[5] The Disability Assessment for Dementia, the Bristol ADL, and the AD8, are informant-based questionnaires that have been shown to effectively assess ADL in order to differentiate MCI patients from dementia patients.[106] Other neuropsychological evaluations include, Grober-Buschke (GB) paradigm, which identifies memory impairment due to the initial stages of AD or other causes; and the Free and Cued Selective Recall Reminding Test (FCSRT), used to identify prodromal AD patients with MCI, with 79.7% sensitivity and 89.9% specificity.[5, 107]

1.4.2 Role of Biomarkers

Not only did the NIA-AA publish recommendations related to AD preclinical stages, the diagnosis of MCI due to AD, as well as the diagnosis of dementia due to AD; the NIA-AA also recommended the integration of biomarker information within their criteria for MCI, prodromal, and AD diagnosis.[5] Biomarkers can be defined as a measurable substance or process that may effect changes within the body and can be observed from outside the patient, in order to understand the prevalence of a disorder in the body.[108] While there is still work to be done to understand the importance and implementation of biomarkers for AD diagnosis in clinical samples, it has been observed that AD biomarkers allow for the discovery of AD pathology in patients with preclinical AD, who do not present cognitive impairment symptoms clinically. [5] The major AD biomarkers are categorized based on biomarkers related to Aβ protein deposition processes: low levels of $A\beta_{1-42}$ in CSF and positive positron emission tomography (PET) amyloid imaging; and biomarkers related to downstream neurodegeneration: high levels of tau protein, total tau, phosphorylated tau in CSF, decreased uptake of 18fluorodeoxyglucose (FDG) in PET in temporo-parietal cortex, as well as disproportionate atrophy on structural magnetic resonance imaging (MRI) in medial, basal, lateral temporal lobe, medial parietal cortex.[5, 108]

In the past decade, there has been a huge surge in the implementation of fluid biomarkers for AD diagnosis in clinical studies, with high consistency and diagnostic accuracy for AD diagnosis, as well as prodromal AD diagnosis.[109] Core CSF biomarkers have been demonstrated to have high diagnostic accuracy in identifying prodromal AD, with a sensitivity and specificity values ranging from 85 to 90%.[110, 111] The core CSF biomarkers for AD include $A\beta_{1\text{-}42}$, which demonstrates cortical amyloid deposition; total tau (t-tau), exhibiting the intensity of neurodegeneration; and phosphorylated tau (p-tau), which relates to neurofibrillary pathological changes.[109] CSF t-tau has become an indicator for the intensity of neurodegeneration, as t-tau levels are very high and continue to increase after acute neuronal damage, and a distinct increase in CSF t-tau levels is observed in AD dementia patients.[110, 111] More specifically, tau proteins within the CSF that have been phosphorylated, i.e. p-tau, correlate more closely with NFT counts.[112-114] Additionally, CSF p-tau levels do not change with acute neuronal damage, or with other neurodegeneration unrelated to NFTs, suggesting that p-tau counts reflect the state of phosphorylated tau more than the amount of neurodegeneration.[112, 113] CSF t-tau and p-tau are highly interrelated, with increased levels found in earlier disease stages, such that, high levels are observed even within patients with preclinical or prodromal AD.[112, 114] Studies also indicate a connection between CSF t-tau and p-tau levels with neuritic plaque counts. However, CSF $A\beta_{1\text{-}42}$ levels remain the most accurate measure for these plaque counts. In contrast to t-tau measurements, initial efforts to identify and compare total CSF Aβ levels showed no or negligible difference, when comparing AD patients and healthy individuals.[115] Recalling the features of Aβ peptides in previous sections, various Aβ species exist in CSF, the predominant species being $Aβ_{1-40}$, which is found at concentrations ten times of those for $Aβ_{1-42}$.[116] Further analysis, measuring only CSF $Aβ_{1-40}$ yielded similar results as total Aβ levels, with minor differences when comparing AD to non-AD patients. The $Aβ_{1-42}$ species is also one that is deposited early in plaques, and when measured in AD patients and healthy individuals, there was a noticeable decrease in CSF $Aβ_{1-42}$ levels from AD patients to control. What was determined here was an association between high neuritic plaque counts and a reduced level of CSF $Aβ_{1-42}$.[117] Hypotheses for this phenomenon are based on the physiochemical features of the $Aβ_{1-42}$ species. This $Aβ_{1-42}$ species is a more hydrophobic peptide, when comparing it to the $Aβ_{1-40}$ species. Thus, aggregation of these $Aβ_{1-42}$ peptides occur more rapidly, resulting in plaque formation, with lower amounts of $Aβ_{1-42}$ species present to be secreted into the extracellular space and CSF, resulting in lower levels in CSF. Further, due to the large difference in concentrations between $Aβ_{1-40}$ and $Aβ_{1-42}$, the CSF $Aβ_{1-40}$ measurements acts as a substitute for total Aβ levels, and measuring the ratio of $Aβ_{1-40}$ to $Aβ_{1-42}$ levels provides a better measure of the reduction in CSF $Aβ_{1-42}$ levels, such that individuals with low total Aβ levels will not be deduced to have brain amyloidosis.[117, 118]

CSF biomarkers can strengthen decision making clinical settings, however, a lumbar puncture in the lower spine to acquire CSF is a painful procedure and is often inaccessible to perform in many memory clinics. Blood biomarkers are often a more desirable biomarker to develop, due to their accessibility in comparison to the CSF. However, development of AD blood biomarkers proves to be difficult due to the low concentrations of these aforementioned CSF biomarkers in the blood, as well as the large amounts of other proteins, lipids, carbohydrates; and the high concentrations of matrix proteins in blood that would cause assay interference.[102] Instead, the development of novel ultra-sensitive techniques may allow for the measurement of these key biomarkers.[106, 110]

In addition to CSF analysis, neuroimaging biomarkers that allow for the assessment of brain anatomy, can detect pathophysiological changes within the brain, as well as providing a diagnostic window for early AD diagnosis.[119] The various biomarkers derived from brain imaging techniques include magnetic resonance imaging (MRI), specifically medial temporal lobe atrophy (MTA); single photon emission computed tomography (SPECT); and positron emission tomography (PET), specifically 18F-fluorodeoxyglucose (FDG) and Pittsburgh Compound B (PiB).[5,120] MTA is a well characterized feature of AD brains and MRI techniques display these atrophies in regions related to cognitive deficits found in neuropsychological evaluation. Other non-AD related dementias have similar atrophies. However, in studies where diagnostic specificity of MTA was assessed in individuals with these non-AD related dementias, MTA was determined to be a highly accurate diagnostic marker for AD in autopsy confirmed AD patients, with a specificity of 94% and sensitivity of 91%.[121] SPECT is another method that evaluates different brain regions related to cognitive deficits, measuring cerebral blood flow. These regions will have poor functionality, and accordingly, a reduction in cerebral blood flow.[122] While SPECT is more widely available and more cost-effective than PET, it is observed to have poor diagnostic accuracy.[122]

The most widely used diagnostic imaging procedure for AD is FDG PET, a minimally invasive tool used to evaluate cerebral glucose metabolism, which acts as a marker for synaptic activity and neuronal function.[5] There are distinct metabolic characteristics for AD, including metabolic impairment within the posterior cingulate and temporo-parietal cortices, as well as conservation of glucose metabolism within the primary sensorimotor and visual cortices, basal ganglia, and cerebellum.[123] In other words, neurodegeneration is characterized by cerebral glucose hypometabolism, such that, FDG-PET scans will show higher degrees of FDG activity in areas that are metabolically active.[123] Another PET method involves the use of an amyloid-binding tracer, *N*-methyl-(11C)-2-(4-methylaminophenyl)-6-hydroxybenzothiazole (11C-PiB), or PiB. Many radiolabeled ligands with affinities toward fibrillar Aβ species within the brain have been developed, and while PiB has a very short half-life of 20 min, it remains the most researched and extensively used ligand.[120] AD patients are observed to have almost twice as much brain PiB uptake in comparison to healthy individuals, with CSF $A\beta_{1-42}$ concentrations decreasing with increased PiB uptake; an indication of the reduction of monomeric $A\beta_{1-42}$ into the CSF as more aggregation of fibrillar Aβ species occur.[124] PiB has a strong affinity toward fibrillar Aβ species, binding strongly within the prefrontal cortex (PFC), and this fibrillar Aβ species is one of the predominant Aβ species during the preclinical stages of AD, with little change in this fibrillar Aβ species level after the progression of AD.[124]

1.5 Anti-Amyloid Strategies

Of the various strategies employed to reduce toxic Aβ peptide load, anti-amyloid strategies involving the direct binding and subsequent prevention of $A\beta_{1-40/42}$ fibrils oligomerization have proven to be an effective approach.[7, 20, 55, 68]

1.5.1 Small Drug Molecules Targeting Secretases

In order to reduce the buildup of insoluble toxic Aβ aggregates, various small drug molecules have been developed to inhibit the secretase enzymes responsible for generating this toxic amyloid peptide.[20] As mentioned previously, the first step within the non-amyloidogenic pathway is the α-secretase cleavage of APP.[43] APP cleavage via α-secretase is beneficial, not only because it releases peptides that are observed to be neuroprotective agents, but also prevents the formation of toxic Aβ peptides.[43] As there is an observed decrease in α-secretase activity in AD patients, a strategy to prevent Aβ peptide formation has been proposed through increased activation of α-secretase, in an attempt to restore the balance to shift more toward the non-amyloidogenic pathway. Many compounds have been identified to increase α-secretase activity including phorbol esters, activators of protein kinase A and C, muscarinic agonists, neuropeptides, statins, and retinoids.[42] While these compounds act as α-secretase activators, issues arise with selectivity and toxicity which has halted the development of these compounds as AD treatments.[42] Furthermore, α-secretase acts on a variety of substrates involved in normal physiological functions which is expected to cause adverse effects in the event of an upregulation in α-secretase activity by modulators.[43]

Instead, more interest has been given to the other secretase enzymes involved in APP processing. BACE-1 is hypothesized to be the initiator of the amyloidogenic pathway, thus, BACE-1 remains the main drug target for Aβ production inhibition. However, similar to α-secretase inhibitor limitations, selectivity issues have been observed for potential small molecules to target BACE-1.[38, 47] As mentioned above, two β-secretase homologues exist and challenges have surfaced in developing BACE-1 inhibitors that do not cross-inhibit its homologue, BACE-2.[17, 20, 27] As a result, there is a possibility that BACE-1 inhibitory drugs may also cause BACE-2 mechanism-based side effects, which would result in various adverse effects.[7]

Similarly, due to the wide range of substrates γ-secretase acts on, targeting this enzyme proved to be problematic due to its involvement in various important cellular pathways.[17, 20, 68] The interference with normal physiological processes, such as the cleavage of other substrates, like notch, may result in severe adverse effects.[37, 41, 49] Instead, there has been a push toward the development of γ-secretase modulators, wherein compounds are developed to target γ-secretase to prevent Aβ production, without lowering the normal physiological levels of other γ-secretase substrates.[37, 125] Some γ-secretase modulators include subset of nonsteroidal anti-inflammatory drugs (NSAIDs). However, these compounds were observed to have low potency and unfavourable pharmacokinetic properties.[125, 126]

1.5.2 Small Drug Molecules Targeting Aβ species

Instead, more interest has been steered toward the development of small molecule inhibitors to prevent the conformational changes of lower order Aβ species from initial random coil to higher order β-sheet structures. As previously mentioned, low molecular weight Aβ oligomers were identified as possessing the most toxic properties, due to their greater solubility and ability to get into cells.[63-65] If a small molecule can form a stable complex with the monomeric Aβ species, this can reduce the rate of oligomerization and prevent protein misfolding.[63-65] In addition, small molecules which can promote the nontoxic forms of Aβ aggregates is considered as desirable in reducing Aβ-mediated toxicity.[127] Other methods involve the development of multifunctional small molecules, with dual activities.[20] For example, Aβ aggregation inhibitors that also contain metal ion chelation properties to reduce the formation of higher order Aβ species, as well as reduce the formation of ROS, have been proposed to be a more effective treatment option to consider.[20] Other examples include the incorporation of existing AD treatment strategies, such as AChEIs, with molecules exhibiting anti-Aβ aggregation properties.[128-130]

1.6 Biphenyl Derivative

The complexity of AD is well-established, with multiple pathologies suggested in order to develop effective therapeutic strategies to alleviate neuropsychiatric symptoms of AD patients. However, as mentioned earlier, current approved drugs provide only symptomatic relief and do not modify or prevent AD from progressing. In addition, since 2003, no new drugs have been approved, leaving many disheartened and searching for new strategies to approach this complex dilemma.[25]

1.6.1 Naturally Occurring Biphenyl Derivatives

The polytherapeutic approach, wherein multiple drugs have multiple targets in order to combat one disease, is one that has great promise.[131] The basis for this approach comes from the use of herbal mixtures that include hundreds of possible active principles, and have been used to treat a multitude of diseases and disorders for centuries before the beginning of modern medicine. Many natural compounds found in these crude herbal remedies include phenolics, such as resveratrol, curcumin (Figure 1.3).[131] Naturally occurring polyphenol-containing compounds are known for their anti-inflammatory, anti-oxidative, anti-aggregating and other protective properties and special interest has been given to studies investigating these compounds and their effect on AD pathogenesis.[68] These natural compounds have been largely investigated for their anti-Aβ aggregation activity, in an attempt to determine the key structures responsible for inhibiting Aβ aggregation.[22, 23] For example, curcumin ((1*E*,6*E*)-1,7-bis(4-hydroxy-3-methoxyphenyl)-1,6-heptadiene-3,5-dione, Figure 1.3), is a naturally occurring diferuloyl methane that has been observed to reduce Aβ levels in transgenic mice, through direct binding and inhibition of the Aβ oligomerization process.[132, 133] Resveratrol (3,5,4′-trihydroxystilbene, Figure 1.3) is another polyphenol which is also known to reduce Aβ load by direct binding, as well as other indirect mechanisms, like inhibiting BACE-1 activity and Aβ plaque disruption.[134, 135]

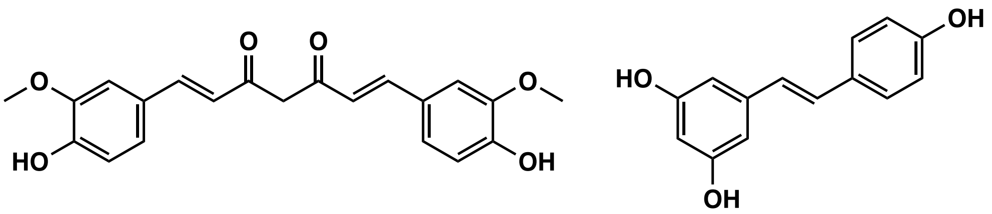

Curcumin **Resveratrol**

Figure 1.3. Chemical structures of curcumin and resveratrol.

The bark of *Magnolia* species is a natural remedy used in traditional Chinese and Japanese medicine, with many biologically active compounds including magnolol and honokiol (Figure 1.4).[136] Honokiol (3,5′-diallyl-4,2′-dihydroxybiphenyl) and magnolol (5,5′-diallyl-2,2′-dihydroxybiphenyl) are both biphenyls with reported features against inflammation, depression, anxiety, and oxidative stress, through scavenging free radicals.[136-140] These natural compounds were also observed to have neuroprotective properties from focal cerebral ischemia-reperfusion injury, NMDA-induced mitochondrial dysfunction, as well as protect neurons against Aβ induced toxicity.[141-143] In addition, these small molecules are capable of crossing the BBB in order to enter the CNS, a highly desirable feature required for drugs that target CNS diseases.[144]

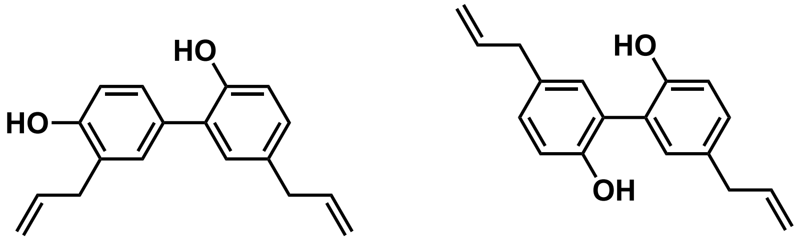

Honokiol **Magnolol**

Figure 1.4. Chemical structures of honokiol and magnolol.

1.6.2 Synthetic Biphenyl Derivatives

The biphenyl structure is an important building block used in organic synthesis. It consists of two benzene rings linked by a C-C bond at the 1,1'-position.[145] The biphenyl ring system is also a key pharmacophore present in many natural and synthetic molecules with biological activity.[145]

Many substituted biphenyl derivatives, with a wide range of activity, have been developed and have been observed to act as antimicrobial, antifungal, anti-proliferative, anti-diabetic, immunosuppressant, analgesic, and anti-inflammatory agents.[145]

In addition, several marketed anti-hypertensive agents, such as losartan, valsartan and telmisartan (Figure 1.5), are biphenyl derivatives.[146] All these anti-hypertensive agents act as angiotensin receptor blockers or antagonists.[149-151] Moreover, NSAIDs such as fluorbiprofen and diflunisal (Figure 1.5), which are used to treat pain disorders including rheumatoid arthritis and osteoarthritis, possess a biphenyl ring system and are known to act as cyclooxygenase (COX) inhibitors.[147-149]

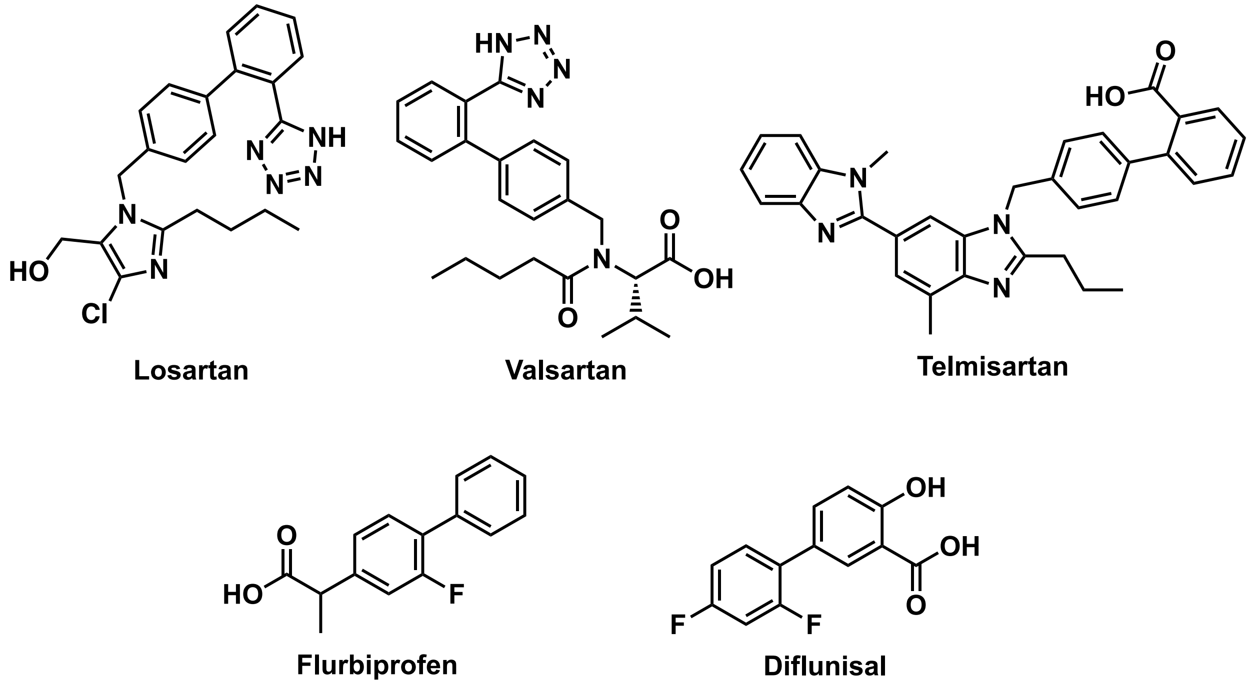

Figure 1.5. Chemical structures of some anti-hypertensive agents and NSAIDs.

With respect to anti-Aβ activity, recent studies have shown that the natural biphenyl derivatives honokiol and magnolol (Figure 1.4) inhibit Aβ aggregation, whereas another synthetic biphenyl derivative biphenyl-3,3',4,4'-tetrol (BPT) (Figure 1.6) displays inhibitory effects on Aβ aggregation, suggesting the potential application of biphenyl derivatives in treating AD.[150]

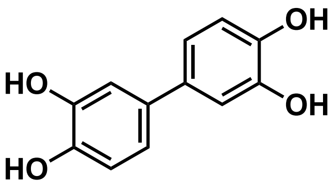

BPT

Figure 1.6. Chemical structure of synthetic biphenyl derivative biphenyl-3,3',4,4'-tetrol (BPT).

1.6.3 Biphenyl Synthesis

Biphenyls are used in the development pharmaceuticals, agrochemicals, ligands, polymers and organic materials. The synthesis of biphenyl compounds was key in the early development of carbon-carbon bond forming chemistries. Many methods today utilize the transition-metal catalyzed cross-coupling approach, an early approach that continues to be the most general and reliable method.[151] The most commonly used cross-coupling reaction is the Suzuki-Miyaura reaction, involving a palladium-catalysed cross-coupling between organoboronic acids and halides. While arylboronic acids have been traditionally used, as new methods have developed, the reaction partner is not limited to arylboronic acids, and includes arylsilicon, arylzinc, aryltin, arylmagnesium compounds, as well as alkyls, alkenyls and alkynyls.[151]

An alternative approach is the use of arynes (or benzynes), which are highly reactive, and the route to biaryls involves the addition of suitable aryl nucleophile to the electrophilic benzyne intermediate. There is a large range of adaptable methods to capture the electrophilic aryne moiety in a C–C bond forming event, wherein benzynes react efficiently with hard organometallics, like aryllithiums and Grignard reagents (e.g. phenylmagnesium bromide) and can participate in multi-component couplings mediated by transition metals such as copper, palladium and nickel. Metal-free aryl bond formation is also observed due to the reactivity of the strained triple bond in benzynes (Scheme 1).[151]

Biphenyls can also be synthesized by using Grignard reagent and aryllithiums with aryl halides, as well as through the Ullman reaction, which involves the coupling of aryl halides via the use of copper metal in thermal conditions.[152, 153] Other methods involve the coupling of aryl halides, through the utilization of a reducing agent in the presence of a catalyst and base, to give biphenyl as major product.[145] However, due to the accessibility and range of availability of arylboronates and reagents, as well as the mild reaction conditions which uses water as a solvent, it is no wonder that the Suzuki-Miyaura method of coupling of biphenyls is predominantly used.

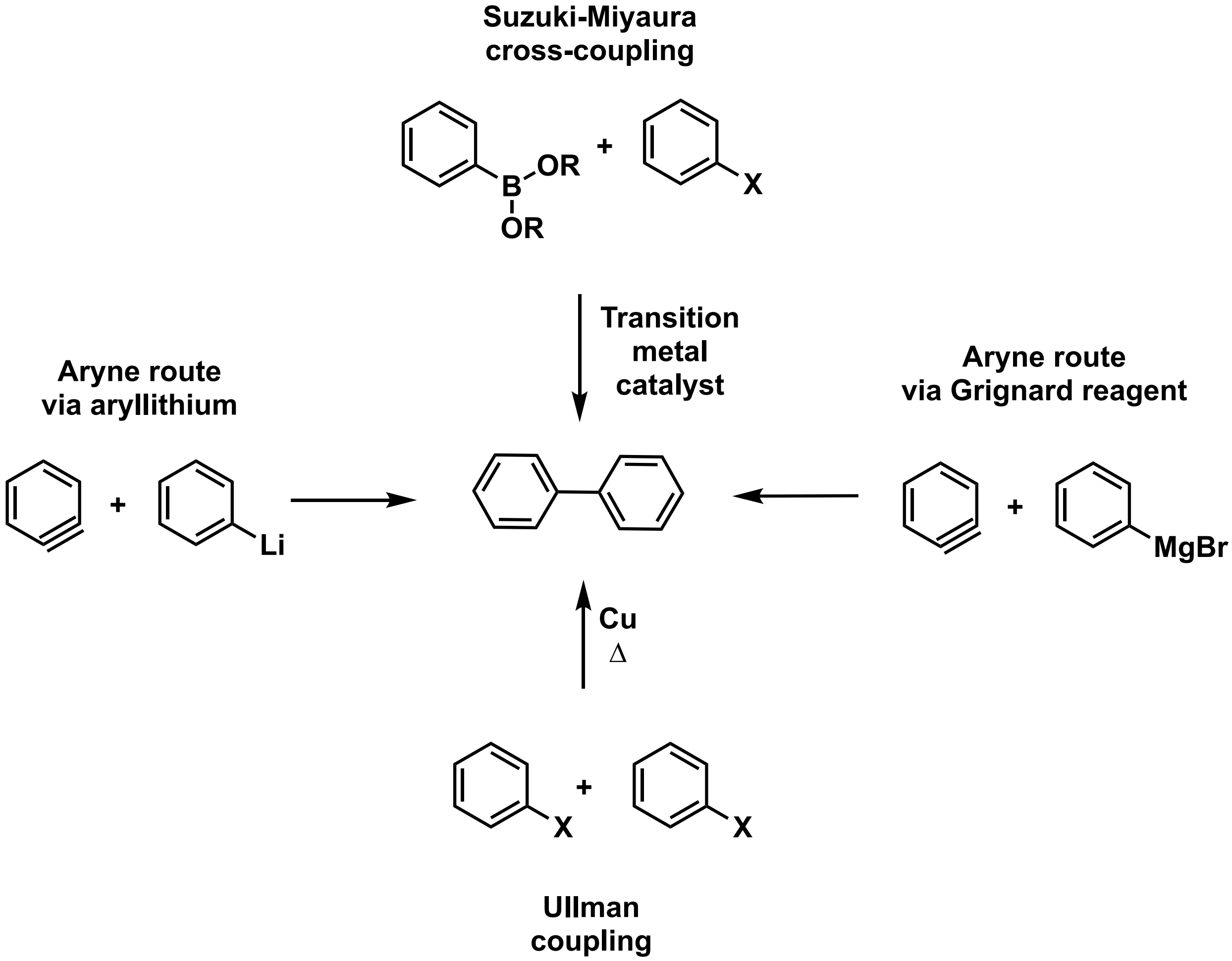

Scheme 1.1. General approaches to biphenyl synthesis.

1.6.4 Ethynyl Bioisostere

The ethynyl or alkyne moiety is a very resourceful two-carbon unit that can be transformed to have a range of functionalities. Ethynyl moieties are unsaturated hydrocarbons, consisting of a carbon-carbon triple bond, wherein the carbon atoms share a σ and two π orbitals between the two, resulting in a linear molecule.[154] While ethynyl containing compounds are predominant within the plant kingdom, they do not occur naturally in mammalian systems. However, these naturally occurring ethynyl containing compounds have been studied extensively for their antifungal and nematicidal activity.[155] These studies have resulted in the incorporation of ethynyl moieties in drug development, in order to improve the pharmacological and biological properties of the drug. The incorporation of ethynyl substituent into synthetic drugs, as in the contraceptives norethindrone and ethynylestradiol, is an example of the application of ethynyl substituents in drug development (Figure 1.7).[155-157]

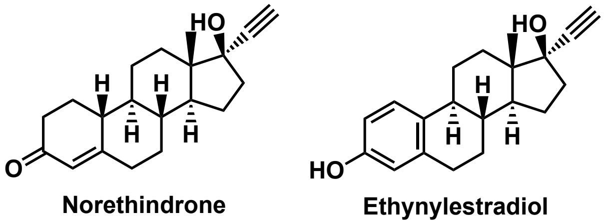

Figure 1.7. Chemical structures of norethindrone and ethynylestradiol.

Furthermore, the incorporation of a terminal unsubstituted ethynyl group on aromatic carbons to act as an electrophilic surrogate for halomethyl has enhanced the pharmacological properties of various drug molecules, as similarities in reactivity are observed between conjugated ethynyls and halomethyls.[158] Halomethyls are observed to enhance the therapeutic efficacy and improve the pharmacological properties of drug molecules, due to their electronegativity, size, lipophilicity, and electrostatic interactions.[159] However, an addition of these halogens can result in unfavourable cytotoxicity, phototoxicity, as well as reactive metabolite formation which can be a disadvantage in drug design.[160, 166] In this case, the use of an ethynyl moiety as a halogen bioisostere could offer a better alternative to the design of novel molecules. In addition, the molecular electrostatic potentials for halobenzenes and phenylacetylene are similar, wherein both exhibit a positive charge at the tip of the C-X/H bond, as well as an area of negative charge perpendicular to this bond; thus, allowing for the polarized ethynyl moiety acts as a weak hydrogen bond donor.[159]

Bioisosteric replacement of halogen moieties with ethynyl groups has been observed in various studies. Novel synthesis of a series of ethynylphenyl carbonates and carbamates, wherein a chloromethyl moiety was replaced with an ethynyl group to improve stability, was developed to target inflammation, as well as dually target AD through AChE inhibition and inflammation suppression.[159] Similarly, the bioisosteric replacement of chlorine moiety with ethynyl group was observed for two marketed drugs, epidermal growth factor receptor (EGFR) inhibitors gefitinib and erlotinib (Figure 1.8). EGFR mutations are oncogenic drivers in cancers, thus inhibitors to bind and block EGFR signalling are a key anti-cancer treatment.[161] The chlorine moiety was observed to undergo weak halogen bonding with a carbonyl oxygen on the binding site. The replacement of this chlorine with an ethynyl moiety, wherein the ethynyl mimicked that contact within the binding site, allowed for these bioisosteres to bind to all conformations of the receptors which was not possible with the corresponding chlorine containing compoound.[158, 161] These examples highlight the application of ethynyl moiety in drug design.

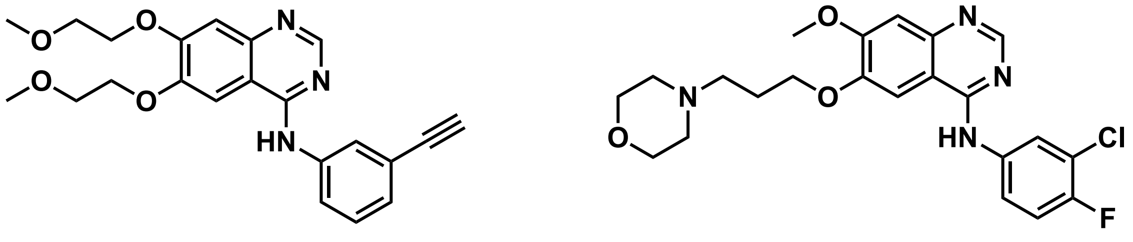

Erlotinib

Gefitinib

Figure 1.8. Chemical structures of erlotinib and gefitinib.

Chapter 2: Hypothesis and Rationale

2.1 Template Design

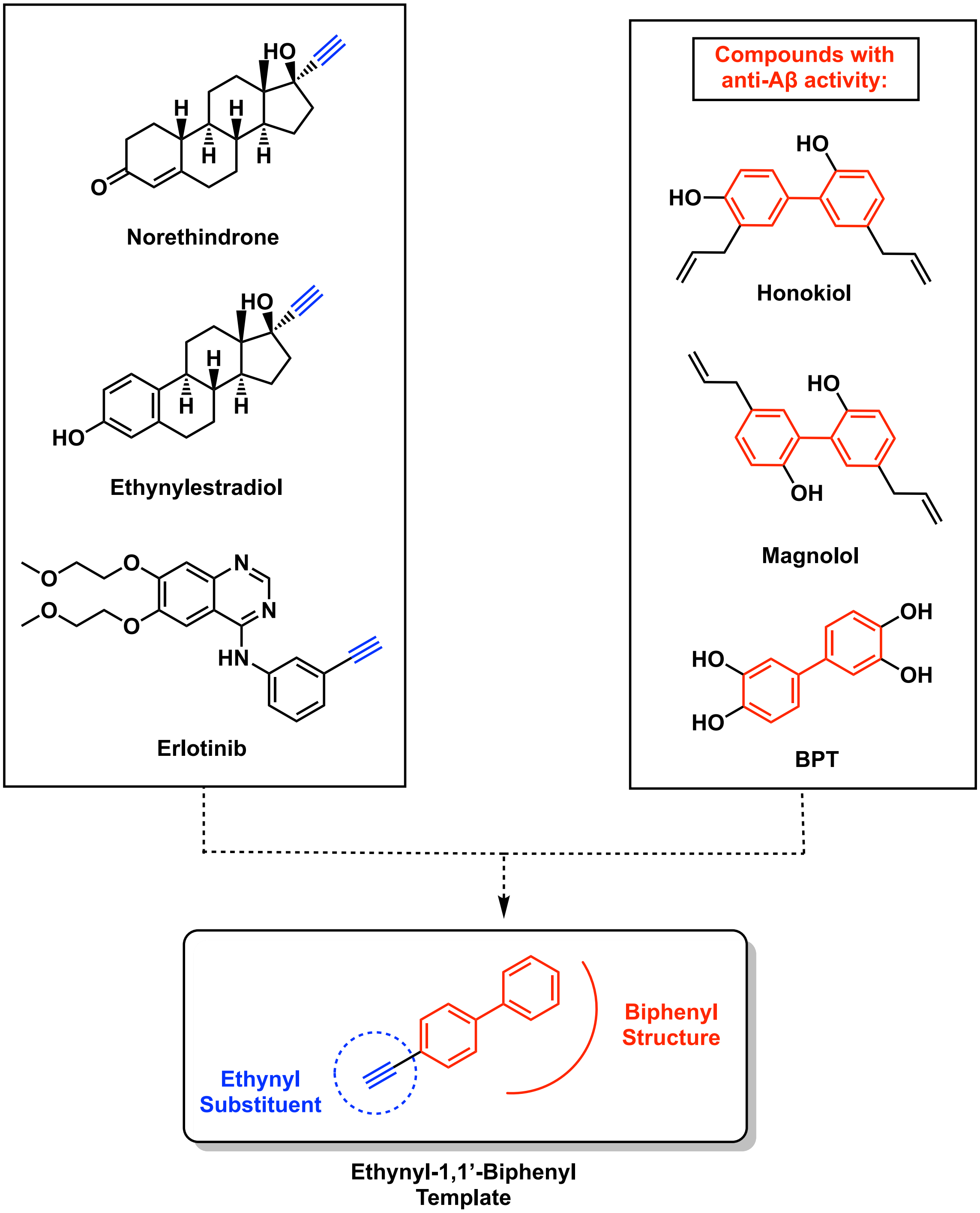

Figure 2.1. Ethynyl-1,1'-biphenyl template design concept based on key functional groups of natural and synthetic pharmacotherapies and other research candidates.

In designing small molecules for CNS diseases, it is critical to ensure that they exhibit optimum physicochemical properties to cross the blood-brain barrier (BBB). In this regard, Lipinski's rule of 5 states that drug candidates should have (i) molecular weights MW < 500 Daltons, (ii) lipohilicity or partition coefficient (cLogP) < 5, (iii) 5 or less hydrogen bond donors (HBDs) and (iv) 10 or less hydrogen bond acceptors (HBA) to exhibit good absorption, distribution, metabolism and excretion (ADME) properties.[162] Over the years, these rules have stood the test of time to develop drugs for non-CNS diseases.[163] As such, when developing potential therapeutics for CNS diseases, one has to consider BBB penetration which can be challenging due their tight junctions that are not easily permeable.[163] In order to optimize this penetration, adjustments in Lipinski's rules have been made, such as MW < 400, cLogP range from 1–4, 3 or less HBDs and 7 or less HBA, to develop CNS drugs with optimal BBB penetration.[162-166]

As previously mentioned, the biphenyl structure is a key pharmacophore that consists of two benzene rings linked by a C-C bond at the 1,1'-position. This pharmacophore is present in many natural and synthetic molecules with a range of biological activities, including properties related to antimicrobial, antifungal, anti-proliferative, anti-diabetic, immunosuppressant, analgesic, and anti-inflammatory function.[145] More interestingly, natural biphenyl derivatives, honokiol and magnolol, and synthetic derivative, BPT, have been observed to have anti-Aβ activity, in addition to a variety of other neuroprotective properties (Figure 2.1). Functionalized biphenyl derivatives can be efficiently synthesized, using suitable catalysts reagents and reactants, as mentioned in section 1.6.3 (Chapter 1).

The unique properties of the ethynyl structure makes it an ideal substituent to this biphenyl pharmacophore. Not only can the ethynyl moiety be easily introduced synthetically, but as identified in earlier sections, terminal unsubstituted ethynyl groups on aromatic carbons are able to act as a halogen bioisostere.[158] This implies that the observed reactivities between conjugated ethynyls and halomethyls are similar, and while halomethyls have favorable pharmacological properties in the design of small drug molecules; halomethyls, unfortunately, can also undergo unfavorable reactions, resulting in the formation of reactive metabolites.[160] The ethynyl group is an example of a non-classical bioisostere, wherein the π orbitals mimic an aromatic system, and the polarized -CH moiety is able to act as a weak hydrogen bond donor. The result is a molecular electrostatic potential that is similar to that of halobenzenes.[159] Moreover, the addition of an ethynyl substituent will prevent the formation of different stereochemical forms, as the ethynyl group is locked in a linear geometry.[165]

The goal of this research project was to design and evaluate a novel template capable of targeting the self-assembly of $A\beta_{1-40/42}$ peptides. We hypothesize that the combination of biphenyl pharmacophore with the ethynyl substituent provides an ideal small drug CNS candidate due to its favourable lipophilicity, and relative stability; as potential anti-AD agents (Figure 2.1).

2.2 Hypothesis and proposed ethynyl-1,1’-biphenyl derivatives

The unsubstituted ethynyl-1,1’-biphenyl ring is lipophilic, with a cLogP value of 4.30, which is suitable for BBB permeation and can be modulated by incorporating polar substituents, as shown in Figure 2.2.

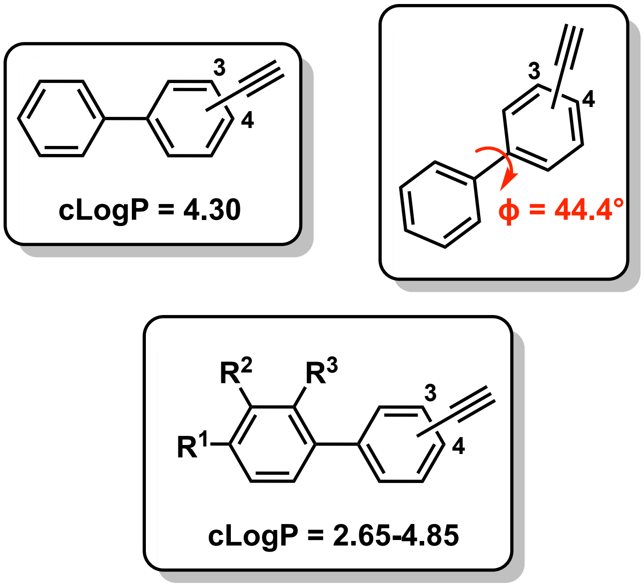

$R^1 = R^2 = R^3 = H$
$R^1 = OMe, R^2 = H, R^3 = H$
$R^1 = H, R^2 = H, R^3 = OMe$
$R^1 = R^2 = OMe, R^3 = H$
$R^1 = OH, R^2 = H, R^3 = H$
$R^1 = F, R^2 = R^3 = H$
$R^1 = SMe, R^2 = H, R^3 = H$
$R^1 = SO_2Me, R^2 = H, R^3 = H$

Figure 2.2. Target ethynyl-1,1’-biphenyl derivative library with noted properties.

The chosen ethynyl-1,1’-biphenyl design was hypothesized to bind effectively to the Aβ dimer species, thus, preventing further Aβ aggregation. Due to the mutually twisted planar properties of this ethynyl-1,1’-biphenyl structure, which contains a dihedral angle ϕ = 44.4° (in gas phase), it was hypothesized that this will allow the molecule to better position itself within the KLVFFA region of the Aβ dimer species (Figure 2.2). The aromatic rings are capable of undergoing van der Waals and hydrophobic interactions in the KLVFFA region of Aβ dimer species, consequently facilitating the anti-aggregating activity. In this regard, preliminary results of the computational analysis demonstrate that the proposed 4-ethynyl 1,1’-biphenyl derivatives exhibit favorable binding interactions with the amyloid dimer model (pdb id: 2LMN). Figure 2.3 shows the interactions of 4-ethynyl-1,1’-biphenyl in the $A\beta_{1-40}$ dimer model. The ethynylbiphenyl derivative underwent various interactions, including H-bond between Val18 amino group in the KLVFFA region and the unsubstituted phenyl ring (distance = 3.25 Å), hydrophobic interactions between Val18 and the unsubstituted phenyl ring (distance = 5.14 Å), and hydrophobic interactions between Phe19 and the unsubstituted phenyl ring (distance = 5.26 Å and 5.14 Å, respectively), suggesting its potential to bind and stabilize the dimer conformation.

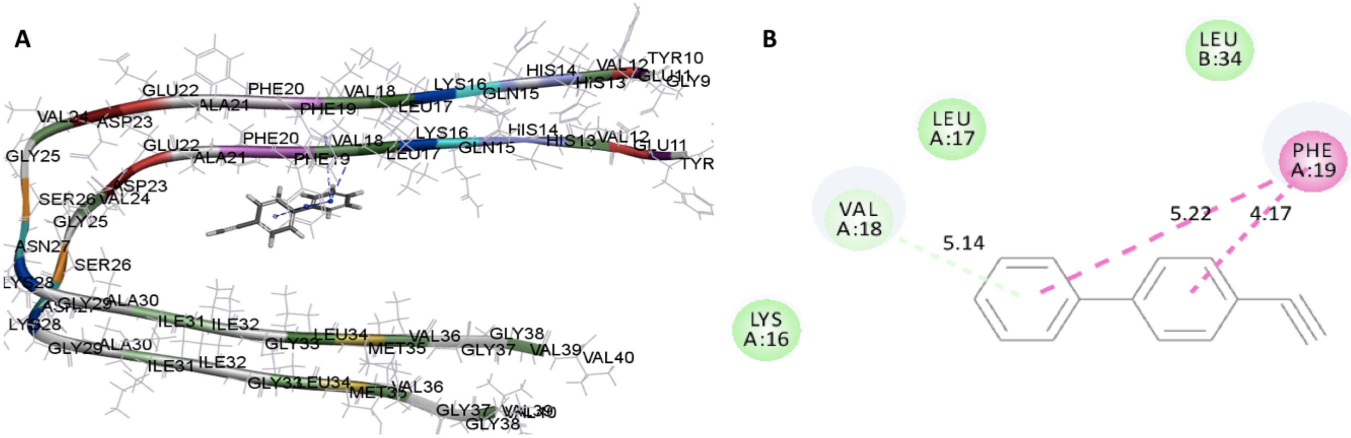

Figure 2.3. The binding mode of 4-ethynyl-1,1’-biphenyl (stick cartoon, Panel A) in the dimer model of $A\beta_{1-40}$ (PDB id: 2LMN). Hydrogen atoms in the $A\beta_{1-40}$ model are removed for clarity. Panel B shows the 2D interaction map of 4-ethynyl-1,1’-biphenyl, with key amino acids in the $A\beta_{1-40}$ dimer model.

It was hypothesized that increasing this dihedral angle of the twisted biphenyls to a perpendicular conformation was expected to favor better binding at the KLVFFA region of Aβ. Furthermore, the structure-activity relationship (SAR) data was obtained by changing the steric and electronic features to study the anti-Aβ activity. For example, the ethynyl-substituent was incorporated at either ortho, or meta or para-positions. In addition, the effect of incorporating substituents at either C3 or C4 (eg. H, F, OH, OMe, SMe or, SO_2Me) on one of the aromatic rings was investigated. Further, through the incorporation of known pharmacophores with anti-Aβ activity, such as 1,2-dimethoxybenzene substituents, it was hypothesized that these chemical features would enhance the anti-Aβ activity, in comparison to the unsubstituted ethynyl-1,1'-biphenyl. In another variation, one of the aromatic rings was replaced with a pyridine bioisotere. While similar to the phenyl ring in properties related to aromaticity, the pyridine ring is more electron-deficient due to the electron withdrawing nature of the nitrogen atom. These pyridine derivatives are noteworthy heterocyclic systems and are key scaffolds in biologically active and naturally occurring substances, due to their valuable pharmacological properties.

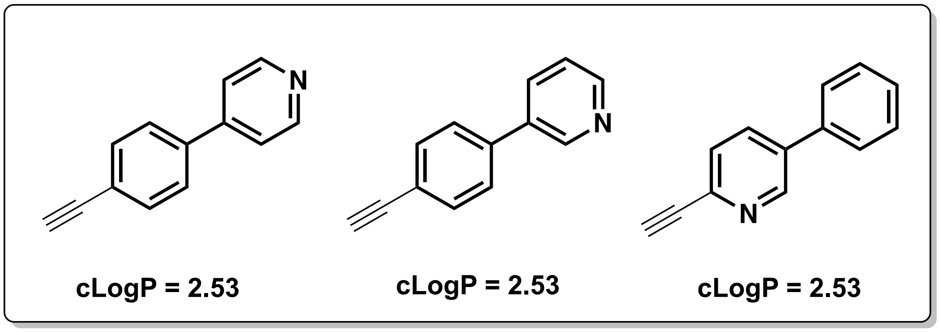

Figure 2.4. Pyridine containing ethynyl-1,1'-derivatives with partition coefficient (cLogP) values.

The addition of the pyridine structure also dramatically decreases the lipophilicity of the compound, which could enhance its oral absorption (Figure 2.4). As a result, it is useful to study and compare the effects of this key moiety to understand the SAR. It is anticipated that the SAR acquired will provide evidence on the suitability of ethynyl-1,1'-biphenyl derivatives in targeting the Aβ aggregation cascade and their potential as anti-AD agents.

Chapter 3:Methodology

3.1. Synthetic Chemistry

In order to synthesize the ethynyl-1,1’-biphenyl derivatives, the synthetic routes chosen were based on literature, with modifications made to optimize yields and to ensure efficient synthesis. After reaction optimization, a small library of 17 ethynyl-1,1’-biphenyl derivatives (**5a-j**, **9a-g** and **14**) were prepared and characterized.

3.1.1. 4-Ethynyl-1,1’-biphenyl derivatives synthesis (5a-h)

The general synthetic summary to prepare the 4-ethynyl-1,1’-biphenyl derivative library is shown below, in Scheme 3.1.

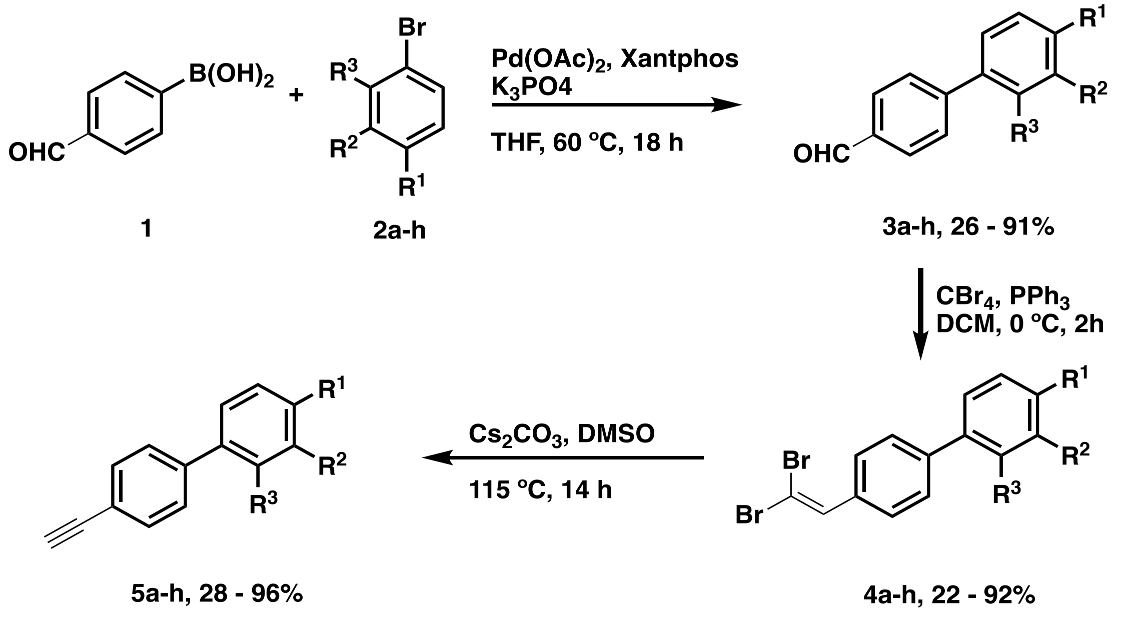

	R^1	R^2	R^3
a	H	H	H
b	OMe	H	H
c	H	H	OMe
d	OMe	OMe	H
e	OH	H	H
f	F	H	H
g	SMe	H	H
h	SO2Me	H	H

Scheme 3.1. General synthetic route for the preparation of 4-ethynyl-1,1'-biphenyl derivatives.

4-ethynyl-1,1'-biphenyl derivatives (**5a-h**) were synthesized by coupling substituted phenylboronic acids (**1**) with bromobenzene or substituted bromobenzene derivatives (**2**) via Suzuki-Miyaura cross-coupling reaction to form a new C-C bond between the two phenyl rings, and to afford carbaldehyde intermediates (**3a-h**).[168] In the next step, the carbaldehyde intermediates (**3a-h**) were brominated with CBr_4 in the presence of triphenylphosphine to obtain geminal dibromoalkenes (**4a-h**).[169] In the last step Cs_2CO_3 was used to generate the final 4-ethynyl-1,1'-biphenyl derivatives (**5**) possessing a terminal acetylene substituent (**5a-h**)[170] as shown in Scheme 3.1. The experimental details, reaction mechanisms and analytical data for all intermediates and final compounds are provided in the following sections.

To begin with, intermediate (1,1'-biphenyl)-4-carbaldehyde (**3a**) and the other biphenyl-4-carbaldehyde derivatives (**3b-h**) were obtained via Suzuki-Miyaura cross-coupling reaction. This reaction was run in tetrahydrofuran (THF), under argon (g), and refluxed for 18 h with stirring, at 60 °C. The resulting solution was evaporated in vacuo, re-dissolved in dichloromethane (DCM), and collected organic fractions were dehydrated using anhydrous magnesium sulfate ($MgSO_4$), filtered and evaporated in vacuo to afford a crude solid intermediate. Purification was performed via silica gel column chromatography with a suitable solvent system. Intermediate product yields ranged from 26 – 91%.

Figure 3.1 displays the palladium catalyzed coupling reaction mechanism to generate (1,1'-biphenyl)-4-carbaldehyde (**3a**).[168] The cross-coupling between the organoboronic acid and the bromobenzene compound is facilitated via a palladium catalyst, palladium (II) acetate. Palladium(II) complexes are generally more stable than the palladium(0) complex and exist predominately in these two oxidation states. In order to drive the reaction to completion and increase product yields, the ligand Xantphos was utilized, as it broadens the substrate scope.[168] As such, the conditions allow for the cross-coupling of a range of electron-rich, electron-poor and sterically hindered arylboronic acids.[168] Initially palladium (II) acetate undergoes reduction when it forms a complex with the Xantphos ligand, generating the palladium (0) complex. This palladium (0) complex is required for the next oxidative addition step to occur. Oxidative addition of the bromobenzene to the palladium(0) complex generates a palladium(II) intermediate. The base, K_3PO_4, facilitates the next step, transmetallation. The phenylboronic acid is activated with the base which enhances the polarization of the organic ligand, forming borate through a more nucleophilic salt complex. As a result, the palladium(II) intermediate undergoes transmetallation with the phenylboronate more readily, and the product (1,1'-biphenyl)-4-carbaldehyde (**3a**) is finally released via reductive elimination, and the palladium(0) catalyst is regenerated.

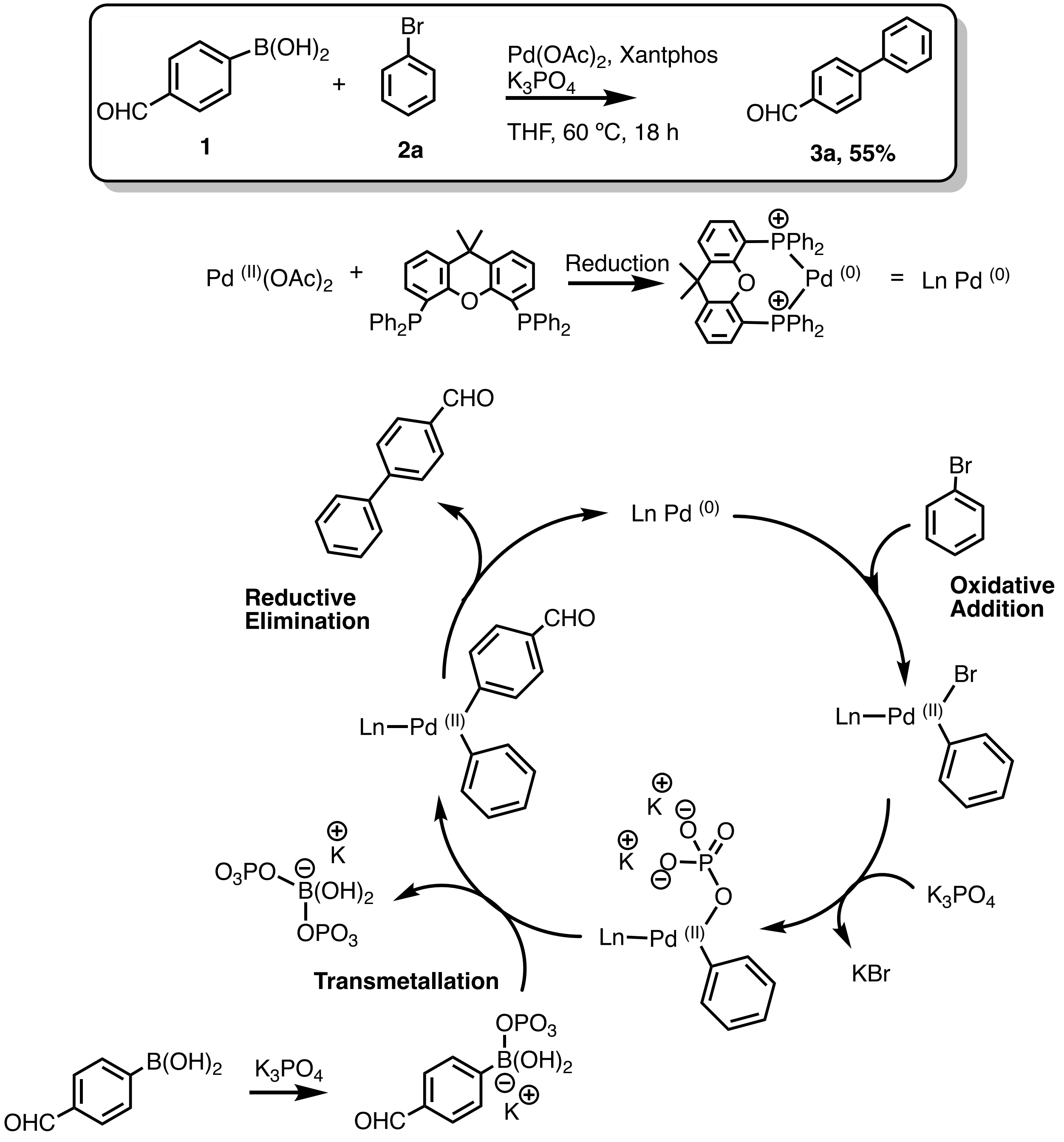

Figure 3.1. Palladium catalyzed Suzuki coupling reaction mechanism to generate [1,1'-biphenyl]-4-carbaldehyde (**3a**).

In the next step, the intermediate (1,1'-biphenyl)-4-carbaldehyde (**3a**) derivatives underwent a bromination via a Corey-Fuchs reaction to form 4-(2,2-dibromovinyl)-1,1'-biphenyl (**4a**) derivative (Figure 3.2).

This reaction was carried out in dichloromethane (DCM) for 2 h with stirring at 0 °C. The resulting solution was evaporated in vacuo, re-dissolved in dichloromethane (DCM), and collected organic fractions were dehydrated using anhydrous magnesium sulfate ($MgSO_4$), filtered and evaporated in vacuo to afford a crude solid intermediate. Purification was performed via silica gel column chromatography with a suitable solvent system. Intermediate product yields ranged from 22 – 92%.

Figure 3.2 displays the bromination via Corey-Fuchs reaction mechanism to generate 4-(2,2-dibromovinyl)-1,1'-biphenyl (**4a**) intermediates.[169] Formation of this dibromoalkene is achieved from its biphenyl-4-carbaldehyde precursor via triphenylphosphine. The formation of the ylide from CBr_4 requires two equivalents of triphenylphosphine. One equivalent of triphenylphosphine forms the ylide, which attacks the aldehyde on the biphenyl-4-carbaldehyde intermediate (**3a**), and the other triphenylphosphine acts as a reducing agent and bromine scavenger. This results in the generation of the 4-(2,2-dibromovinyl)-1,1'-biphenyl (**4a**) intermediate.

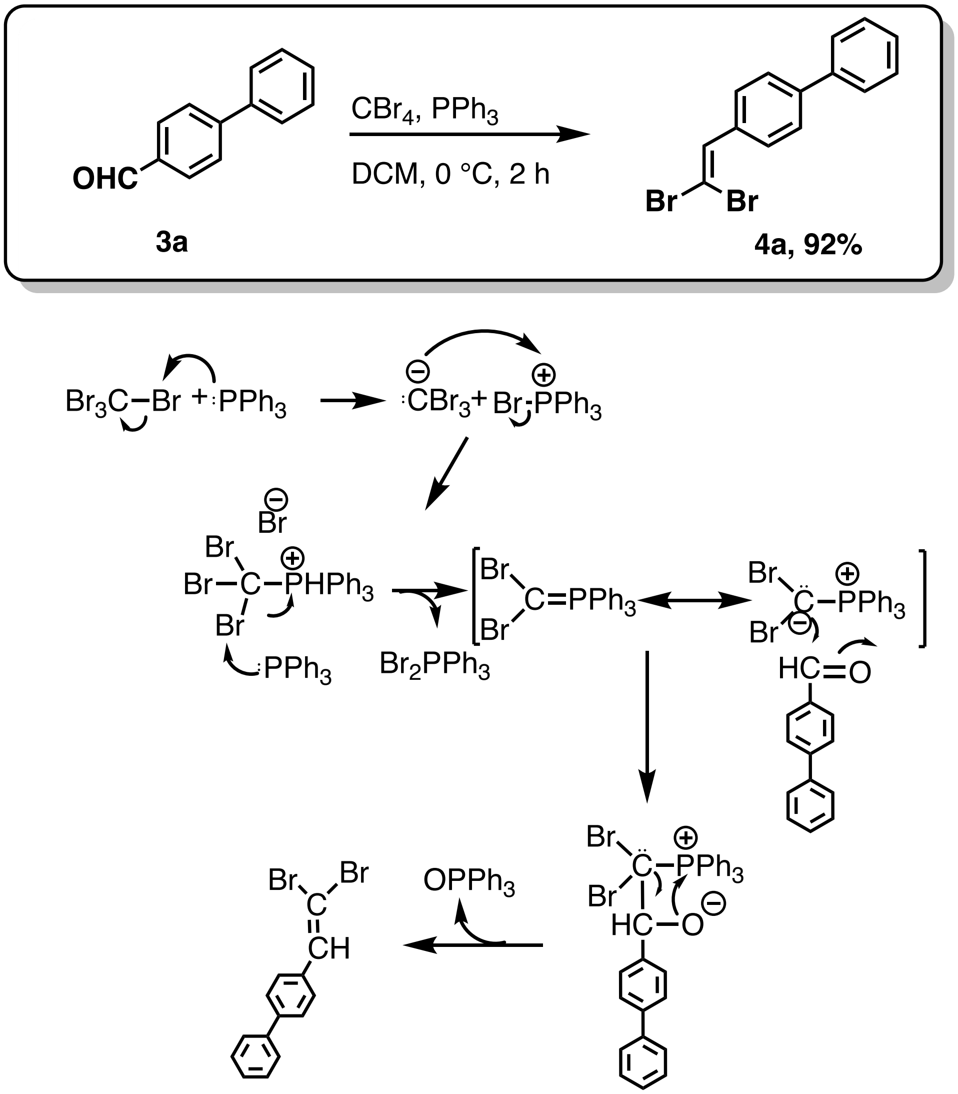

Figure 3.2. Bromination via Corey-Fuchs reaction mechanism to generate 4-(2,2-dibromovinyl)-1,1'-biphenyl (**4a**).

Finally, 4-ethynyl-1,1'-biphenyl (**5a**) was obtained via Cs_2CO_3-mediated synthesis (Figure 3.3).[170] This reaction was run in dimethylsulfoxide (DMSO), and refluxed for 14 h with stirring, at 115 °C. The resulting solution was evaporated in vacuo, re-dissolved in ethyl acetate (EtOAc), and collected organic fractions were dehydrated using anhydrous magnesium sulfate ($MgSO_4$), filtered and evaporated in vacuo to afford a crude solid intermediate. Purification was performed via silica gel column chromatography with a suitable solvent system. Final product yields ranged from 28 – 96%. Figure 3.3 displays Cs_2CO_3-mediated synthesis reaction mechanism to generate 4-ethynyl-1,1'-biphenyl (**5a**).

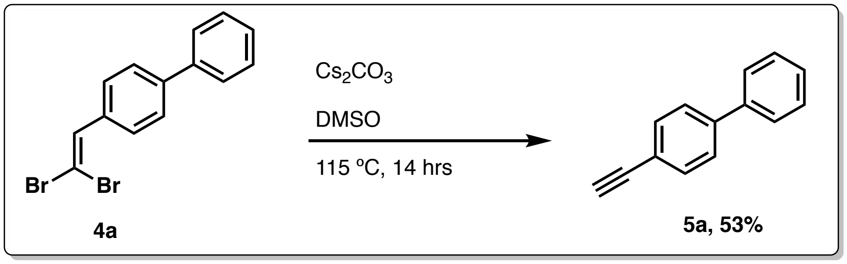

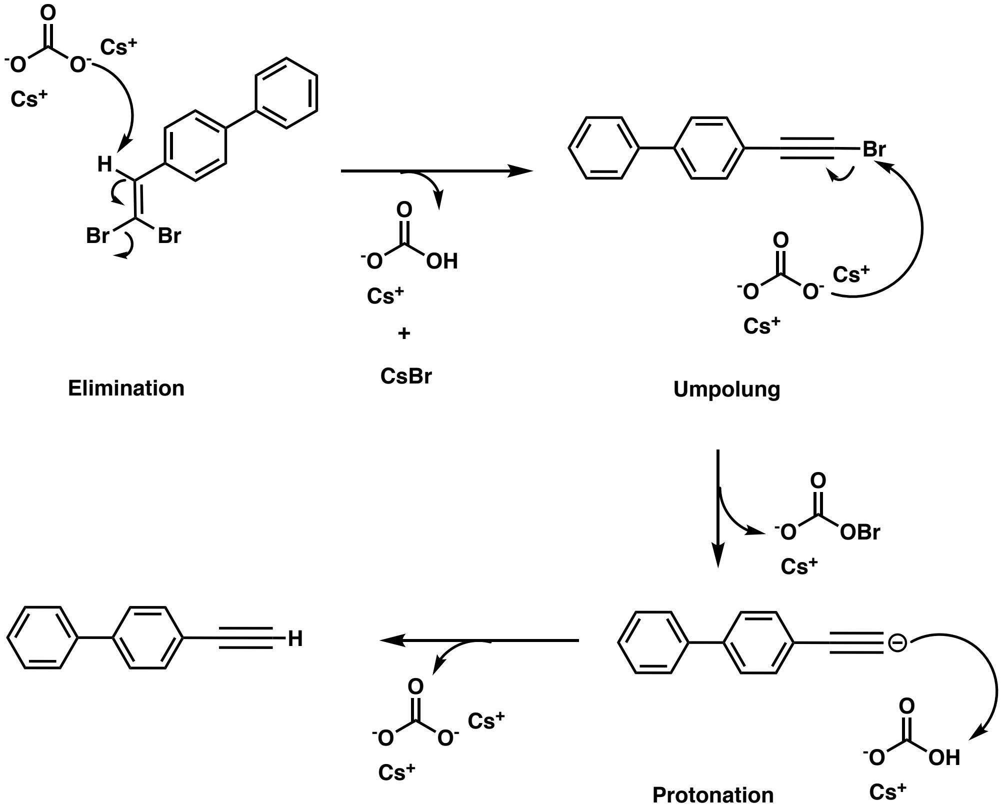

Figure 3.3. Cs_2CO_3-mediated synthesis reaction mechanism to generate 4-ethynyl-1,1'-biphenyl (**5a**).

The synthesis of terminal aryl-acetylene product from the dibromo-alkene intermediate, involves the use of inorganic base Cs_2CO_3 via an umpolung, or polarity inversion, reaction.[170] Cs_2CO_3 was utilized as it has better solubility in DMSO than other inorganic bases, like K_2CO_3 or Na_2CO_3. The proposed reaction involves a two-step process, wherein, under basic conditions, the elimination of hydrogen bromide from the alkene results in the formation of the alkyne, followed by umpolung/protonation in a single step to form (**5a**).[170]

3.1.2. 3-Ethynyl-1,1'-biphenyl derivatives synthesis (9a-g)

The general synthetic summary to prepare the 3-ethynyl-1,1'-biphenyl derivatives library is shown below, in Scheme 3.2.

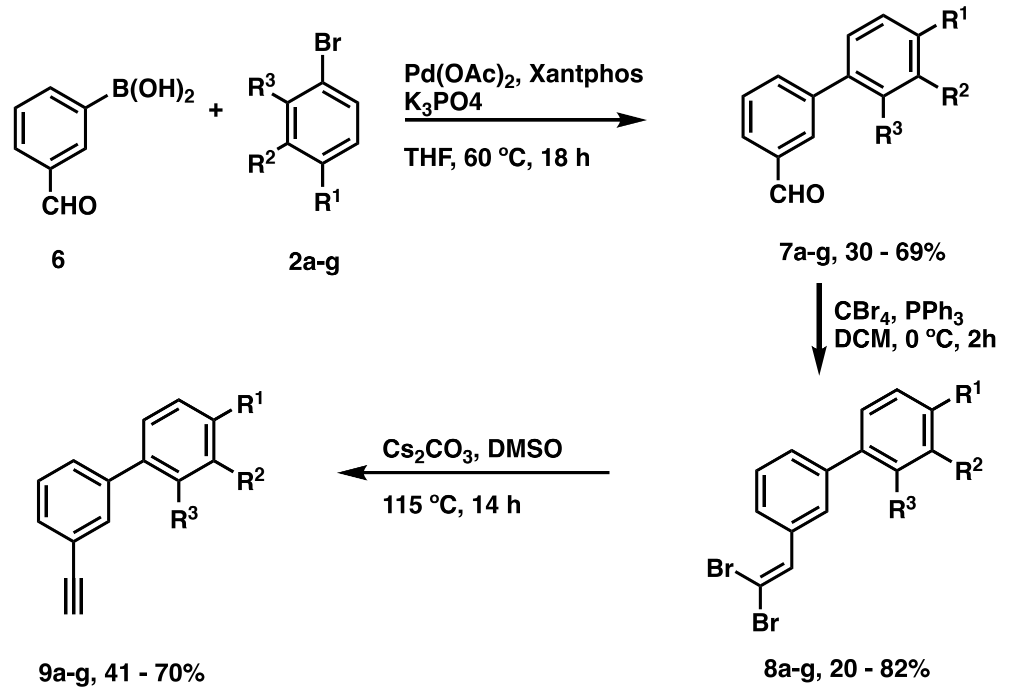

	R^1	R^2	R^3
a	H	H	H
b	OMe	H	H
c	H	H	OMe
d	OMe	OMe	H
e	OH	H	H
f	F	H	H
g	SMe	H	H

Scheme 3.2. General synthetic route for the preparation of 3-ethynyl-1,1'-biphenyl derivatives.

The synthesis of 3-ethynyl-1,1'-biphenyl derivatives (**9a-g**) was obtained in the exact same manner as the 4-ethynyl-1,1'-biphenyl derivatives (**5a-h.** Scheme 3.1), with the only difference in the use of the 3-formylphenylboronic acid (**6**), rather than 4-formylphenylboronic acid (**1**). Following the same method as the synthesis of the 4-ethynyl-1,1'-biphenyl derivatives, substituted phenylboronic acids (**6**) with bromobenzene or substituted bromobenzene derivatives (**2a-g**) undergo Suzuki-Miyaura cross-coupling reaction to form a new C-C bond between the two phenyl rings, and to afford carbaldehyde intermediates (**7a-g**).[168] In the next step, the carbaldehyde intermediates (**8a-g**) were brominated with CBr_4 in the presence of triphenylphosphine to obtain geminal dihaloalkenes (**8a-g**).[169] In the last step Cs_2CO_3 was used to generate the final 4-ethynyl-1,1'-biphenyl derivatives (**9**) possessing a terminal acetylene substituent (**9a-g**).[170]

3.1.3. Ethynylphenyl pyridine derivative synthesis (5i, 5j, 14)

Synthesis of ethynylphenyl pyridine derivatives follows the same scheme as the 4- and 3-ethynyl-1,1'-biphenyl reaction schemes (Schemes 3.1 and 3.2). The general synthetic summary to prepare 4-(4-ethynylphenyl)pyridine and 3-(4-ethynylphenyl)pyridine is shown below, in Scheme 3.3. These derivatives (**4i-j**) were obtained in the exact same manner as the 4-ethynyl-1,1'-biphenyl derivatives (**5a-f**), with the only difference being the use of bromopyridine as the coupling agent (**2i-j**).

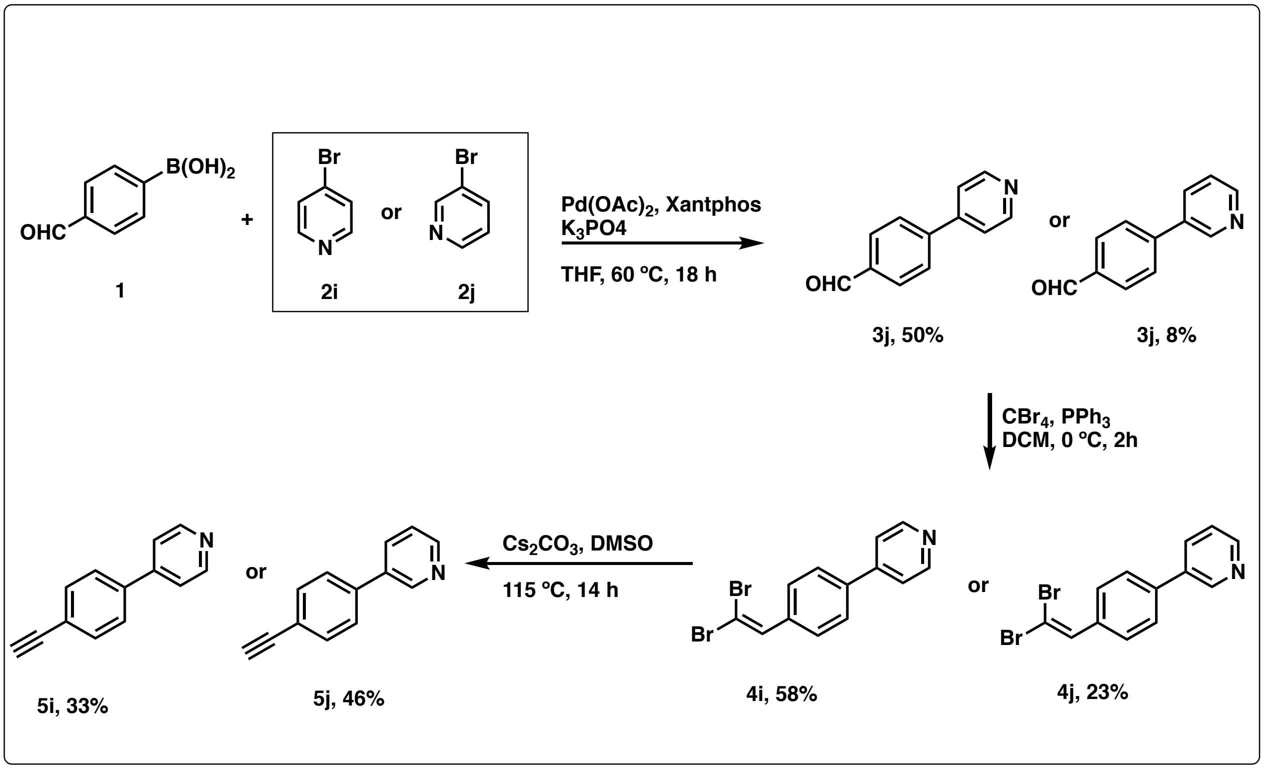

Scheme 3.3. General synthetic route for the preparation of 4-(4-ethynylphenyl)pyridine (**5i**) and 3-(4-ethynylphenyl)pyridine (**5j**).

In contrast, the corresponding regioisomer of **5j** (2-ethynyl-5-phenylpyridine, compound **14**) was synthesized after obtaining the starting 3-ethynylpyridine in a two-step reaction, starting with a Sonogashira cross-coupling to obtain (trimethylsilyl)ethynylpyridine, its deprotection under basic conditions and final coupling with phenylboronic acid (Scheme 3.4).[168,171,172] Similar to the Suzuki-Miyaura coupling reaction, the Sonogashira reaction is able to couple terminal alkynes with aryl halide under mild conditions and with high selectivity.[171] This cross-coupling requires a palladium catalyst, a copper(I) co-catalyst, and an amine base in order to drive this reaction to completion. In this case, trimethylsilylacetylene (TMSA) acts as the terminal alkyne protecting group and using these conditions, a new C-C bond is formed with the aryl halide, or 5-bromo-2-iodopyridine (**10**). This Sonogashira reaction yielded 5-bromo-2-((trimethylsilyl)ethynyl)pyridine

(**11**) as the product. In the next step, treatment of the (trimethylsilyl) acetylene (**11**) with sodium hydroxide afforded the desilylated product **12**, which was then combined with phenylboronic acid (**13**) in a Suzuki-Miyaura cross-coupling reaction in order to afford the final product, 2-ethynyl-5-phenylpyridine (**14**).[168, 172] The general synthetic summary to prepare 2-ethynyl-5-phenylpyridine (**14**) is shown below, in Scheme 3.4.

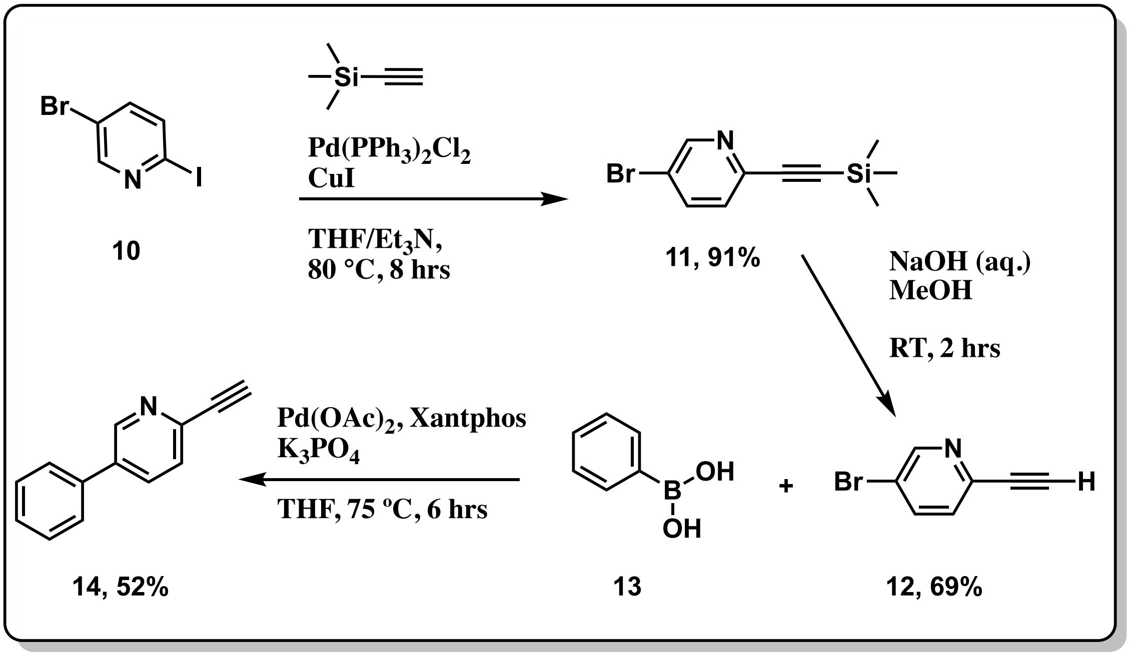

Scheme 3.4. General synthetic route for the preparation of 2-ethynyl-5-phenylpyridine (**14**).

To start with, the intermediate 5-bromo-2-((trimethylsilyl)ethynyl)pyridine (**11**) was obtained via Sonogashira cross-coupling reaction.[171] This reaction was carried out in tetrahydrofuran (THF)/triethylamine (Et_3N), under argon , and refluxed for 8 h with stirring, at 80 °C. The resulting solution was evaporated in vacuo, re-dissolved in ethyl acetate (EtOAc), and collected organic fractions were dehydrated using anhydrous magnesium sulfate ($MgSO_4$), filtered and evaporated in vacuo to afford a crude solid intermediate. Purification was performed via silica gel column chromatography with a suitable solvent system. Intermediate product yields was 91%.

Figure 3.4 shows the palladium catalyzed coupling reaction mechanism to generate 5-bromo-2-((trimethylsilyl)ethynyl)pyridine (**11**). This cross-coupling between the 5-bromo-2-iodopyridine (**10**) and TMSA requires a palladium catalyst, a copper(I) cocatalyst, and an amine base in order to drive this reaction to completion. The palladium catalyst here is palladium(II) triphenylphosphine dichloride, which undergoes a ligand exchange with Et_3N, followed by β-hydride elimination and reductive elimination to produce the palladium(0) complex.[171] Oxidative addition of the 5-bromo-2-iodopyridine (**10**) to the palladium(0) complex generates a palladium(II) intermediate. Copper(I) iodide in the presence of Et_3N reacts with TMSA to generate the alkynyl copper, which then undergoes transmetallation with the palladium(II) intermediate complex. Reductive elimination with coupling of the two organic ligands gives the product and regenerates the palladium(0) catalyst. Trans/cis isomerization occurs next, which is then followed by reductive elimination to afford the final product, 5-bromo-2-((trimethylsilyl)ethynyl)pyridine (**11**).[171]

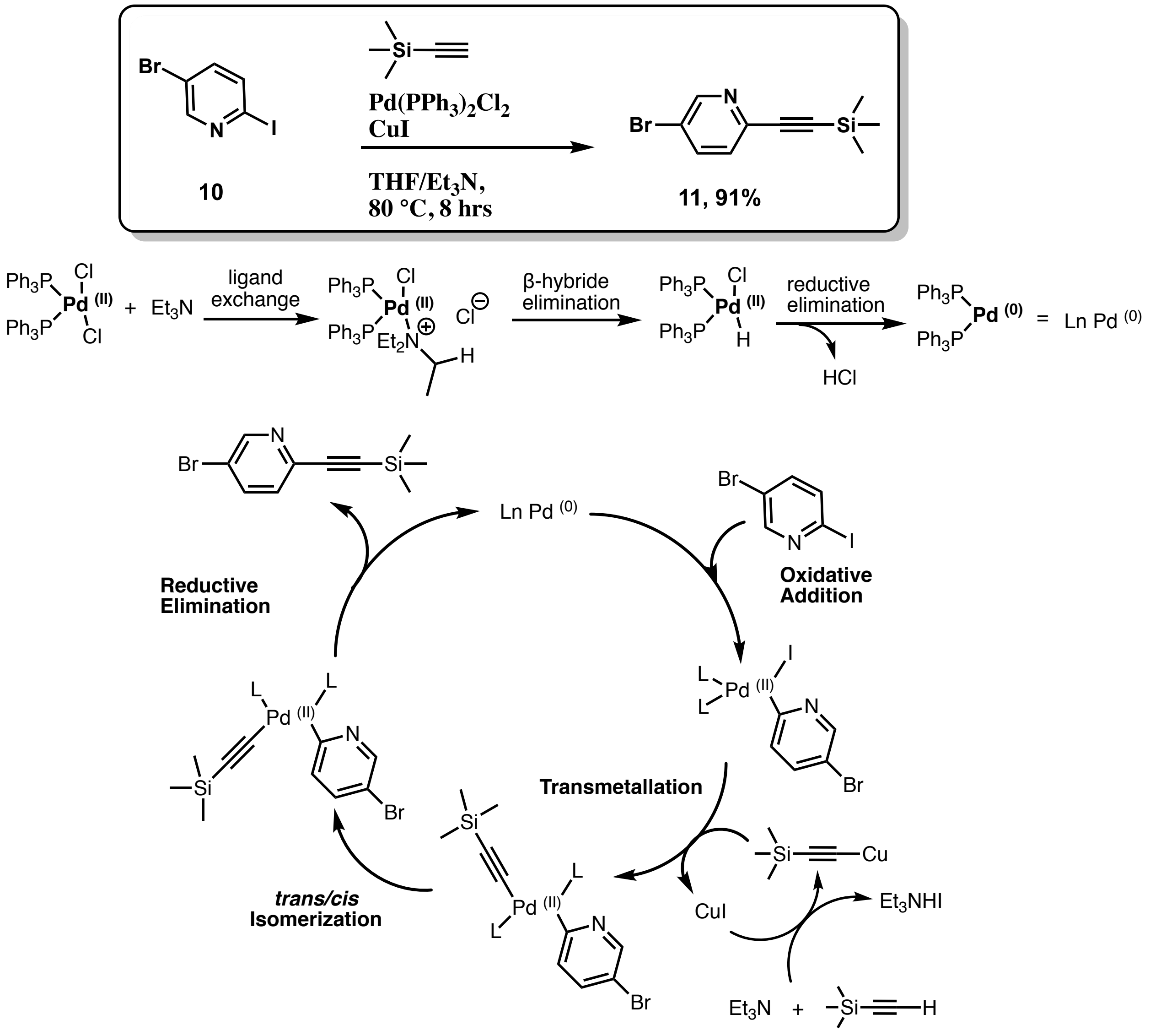

Figure 3.4. Palladium catalyzed Sonoghashira coupling reaction mechanism to generate 5-bromo-2-((trimethylsilyl)ethynyl)pyridine (**11**).

This 5-bromo-2-((trimethylsilyl)ethynyl)pyridine (**11**) intermediate was treated with sodium hydroxide (NaOH) to afford the desilylated product **12**.[172] The triple bond of **11** can be selectively reduced when conditions are controlled to minimize reductive debromination; in this case, reducing the time and amount of NaOH added to the reaction mixture. The desilylated intermediate **12** was then combined with phenylboronic acid (**13**) in a Suzuki-Miyaura cross-coupling reaction in order to afford the final product, 2-ethynyl-5-phenylpyridine (**14**). The reaction mechanism of this Suzuki-Miyaura cross-coupling is the same as the mechanism outlined for products **3a-j, 7a-g**.[168]

3.2. Biological Assays

Biological screening for the ethynylbiphenyl derivatives **5a-h**, **9a-g** and **14** was carried out by measuring their anti-aggregation properties against both Aβ$_{1-40}$ and Aβ$_{1-42}$. This was achieved by conducting fluorescence aggregation kinetics studies and transmission electron microscopy (TEM). The results obtained provided SAR data on the potential of ethynylbiphenyl derivatives as anti-AD agents. The details of biological assays are given in the sections below.

3.2.1. Amyloid-β (Aβ) aggregation assay

The anti-Aβ aggregation activity of the ethynylbiphenyl derivatives **5a-j**, **9a-g**, **14** and other biphenyl derivatives were evaluated using the ThT-based fluorescence kinetic assay. More specifically, the mechanism of action of compounds toward Aβ aggregation by direct binding can be determined experimentally via fluorescence spectroscopy. This ThT-based fluorescence assay relies on a key probe, thioflavin T (ThT), which is used in order to monitor and measure Aβ fibril formation.[173] ThT a benzothiazole dye that exhibits enhanced fluorescence upon binding to amyloid fibrils. ThT binds in between the β-sheets formed during Aβ fibrillization, causing a shift in the conformation of ThT.[173, 174] This conformational change also influences the fluorescent properties of ThT, resulting in a shift in the excitation spectrum. In protic solvents, free ThT absorbs at 385 nm, with an emission maximum value of 445 nm. Upon binding to Aβ, however, this fluorescent excitation shifts to 440 nm, and emission maximum shifts to a value of 490 nm.[174] As such, this method was used to quantify the Aβ aggregation process over a period of time, wherein, the ability of ethynylbiphenyl derivatives to promote or inhibit Aβ aggregation was determined by aggregation kinetic study. The change in the fluorescence of the excitation and emission wavelengths of ThT was measured, where an increase in fluorescence indicates the binding of ThT to Aβ oligomers or fibrils.

Amyloid aggregation occurs, typically, in three phases. The first being the lag phase, wherein monomeric species of Aβ undergo misfolding to form dimer species. Figure 3.5 displays a general model for ThT-based $A\beta_{1\text{-}40}$ and $A\beta_{1\text{-}42}$ aggregation, with $A\beta_{1\text{-}40}$ and $A\beta_{1\text{-}42}$ curves identified. While $A\beta_{1\text{-}40}$ has a sigmoidal shaped curve, the $A\beta_{1\text{-}42}$ curve is observed to take on a more logarithmic curve shape. This is due to the length of lag time for each species. The lag phase is much shorter for $A\beta_{1\text{-}42}$, in comparison to $A\beta_{1\text{-}40}$, as $A\beta_{1\text{-}42}$ is more insoluble and prone to aggregation at a faster rate than $A\beta_{1\text{-}40}$. This lag phase is followed by a rapid growth phase, wherein dimer species aggregate to form oligomers and larger protofibrils. As this process is more thermodynamically favourable in comparison to the lag phase, it proceeds quickly. This elongation phase is rapidly followed by a saturation phase, wherein the predominant Aβ species is the mature fibril species. The curve is observed to plateau at this increased fluorescence value, highlighting the stability of these mature Aβ fibril species. The known Aβ aggregation inhibitor methylene blue was used as reference compound, when conducting this assay to determine the anti-Aβ aggregation activity of the ethynylbiphenyl derivatives.

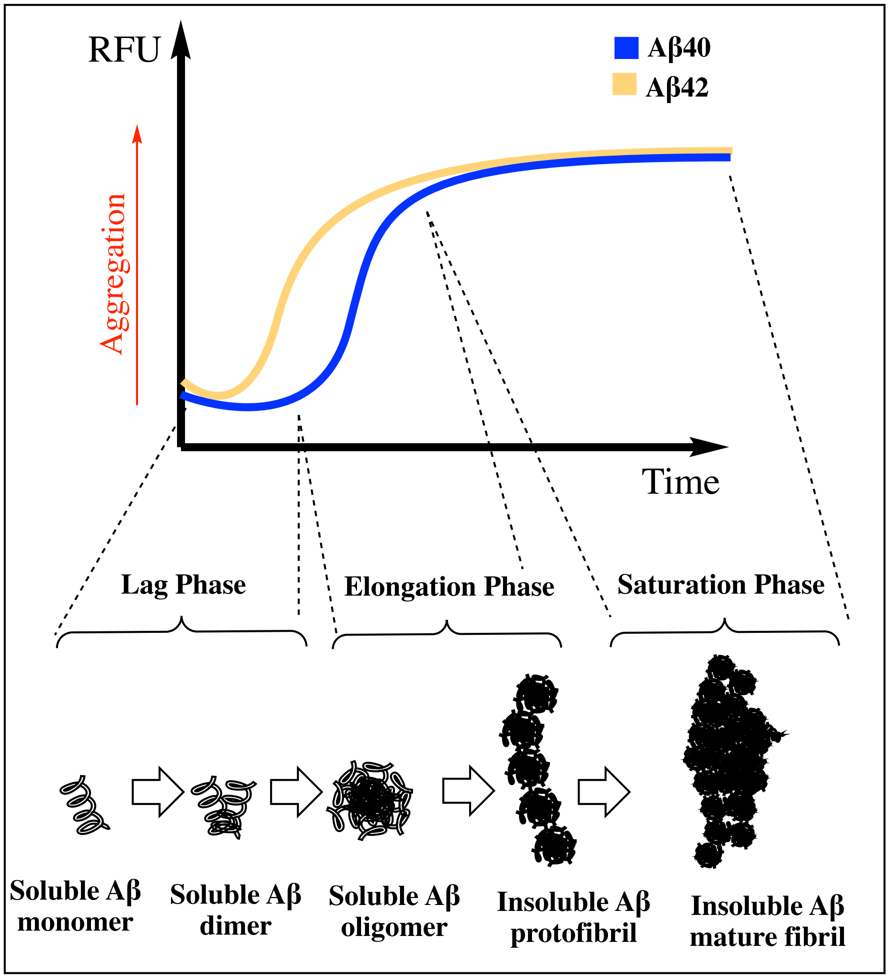

Figure 3.5. ThT-based Aβ$_{1\text{-}40/42}$ aggregation kinetic curve model.

3.2.2. TEM assay and imaging

While biochemical studies were carried out to assess the anti-aggregation properties of ethynylbiphenyl derivatives toward Aβ$_{1\text{-}40/42}$ peptide by fluorescence aggregation kinetics, transmission electron microscopy (TEM) was used to monitor the aggregation morphologies of these samples.[173] This electron microscope imaging technique is often used to visualize the ultrastructure, or fine features, of a cell and morphology; with a theoretical resolution of 0.002 nm.[175] As electrons pass through a sample, the filament or cathode from the TEM emits electrons, passing through a small hole to create an electron beam. As a result, electrons are able to pass directly through the sample or the electrons are scattered by electron dense, or stained, structures, which appear darker.[173, 175] The resulting image is recorded with high-resolution digital camera. Samples are stained with an electron-dense material, like phosphotungstic acid (PTA), which will provide better contrast to visualize our proteins of interest.[173, 175]

The Aβ aggregate morphology was evaluated by carrying out transmission electron microscopy (TEM) in the presence and absence of ethynylbiphenyl derivatives. These studies provide further confirmation on the anti-Aβ activity of promising ethynylbiphenyl derivatives.

Chapter 4: Results and Discussion

As discussed previously, the primary aim of this project was to design, synthesize and evaluate novel ethynyl-1,1'-biphenyl ring scaffolds that can prevent A$\beta_{1-40/42}$ aggregation, through the utilization of medicinal chemistry principles. In this regard, the SAR data for a library of 17 small molecules based on ethynyl-1,1'-biphenyl system was obtained. The biological profiles for the derivatives within this library will be discussed in this section, with a focus on their anti-A$\beta_{1-40/42}$ aggregation properties and TEM experiments to support these observations. Molecular modeling studies were conducted on the best candidates identified within this ethynyl-1,1'-biphenyl library, in order to gain an understanding of the binding interactions between the compounds and A$\beta_{1-40/42}$ models.

4.1. Structure activity relationship (SAR) studies

The SAR studies allow for the identification of the functional groups or moieties responsible for a specific biological effect. In our case, the obtained SAR studies provides a better understanding on the effect of ethynyl-1,1'-biphenyl derivatives with different electronic and steric features on Aβ aggregation inhibition properties.

4.1.1. Anti-Aβ_{1-40} aggregation activity

Through the utilization of ThT-based fluorescence kinetic assay, the anti-Aβ_{1-40} aggregation activity of the ethynyl-1,1'-biphenyl derivatives was evaluated at 1, 5, and 25 μM concentrations. The results are presented below in Table 4.1, as average % inhibition ± SD, n = 3 for two independent experiments, and were compared with the known inhibitor methylene blue (MB). In addition to our synthesized ethynyl-1,1'-biphenyl derivatives **5a-j**, **9a-g** and **14**, known Aβ_{1-40} inhibitors honokiol and magnolol, as well as unsubstituted biphenyl, various halo and cyano substituted biphenyl compounds were also tested to obtain a more detailed SAR study (Table 4.1).

As mentioned in previous sections, honokiol and magnolol are naturally occurring biphenyls with observed anti-Aβ aggregation properties.[137-144] Comparing our ethynyl-1,1'-biphenyl library with these additional compounds will allow for a better understanding on the chemical features that account for their anti-Aβ aggregating activity and provide valuable information on the use of ethynyl-substituents as bioisosteres of halogens or cyano-substituents.

Table 4.1: Inhibition data for ethynyl-1,1'-biphenyl derivatives **5a-j**, **9a-g**, **14** and other biphenyl derivatives toward Aβ_{1-40}.

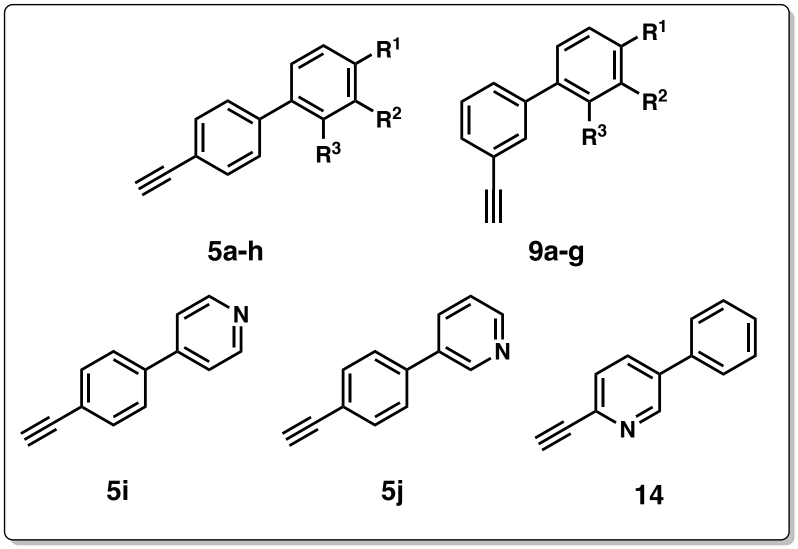

	R^1	R^2	R^3
a	H	H	H
b	OMe	H	H
c	H	H	OMe
d	OMe	OMe	H
e	OH	H	H
f	F	H	H
g	SMe	H	H
h	SO_2Me	H	H

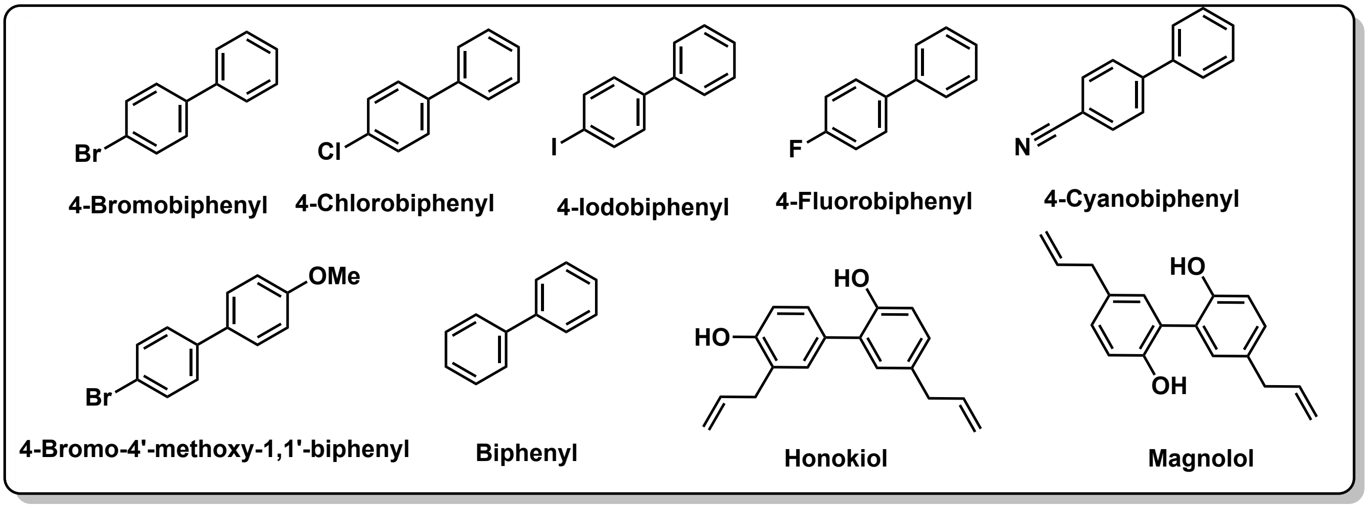

Compound	**R^1**	**R^2**	**R^3**	**% Inhibition (1 µM)**	**% Inhibition (5 µM)**	**% Inhibition (25 µM)**
5a	H	H	H	39.18 ± 1.21	43.82 ± 20	62.42 ± 7.12
5b	OMe	H	H	18.32 ± 7.20	36.53 ± 10.15	43.74 ± 6.02
5c	H	H	OMe	25.72 ± 1.30	35.19 ± 1.57	38.02 ± 5.87
5d	OMe	OMe	H	11.61 ± 0.17	34.24 ± 3.74	45.62 ± 3.49
5e	OH	H	H	18.49 ± 3.08	29.31 ± 3.29	66.91 ± 1.73
5f	F	H	H	18.29 ± 4.51	37.67 ± 4.82	46.35 ± 2.54
5g	SMe	H	H	2.54 ± 0.17	14.83 ± 1.80	26.58 ± 1.67
5h	SO_2Me	H	H	11.14 ± 0.38	15.91± 0.32	35.29 ± 1.38
5i	-	-	-	11.06 ± 0.59	58.47 ± 0.29	79.08 ± 2.24
5j	-	-	-	21.98 ± 0.42	34.13 ± 0.85	64.50 ± 0.36
9a	H	H	H	41.71 ± 0.69	46.73 ± 0.53	55.82 ± 2.75
9b	OMe	H	H	11.05 ± 2.83	27.91 ± 4.34	32.62 ± 2.95
9c	H	H	OMe	19.41 ± 2.07	36.38 ± 0.25	45.90 ± 1.81
9d	OMe	OMe	H	38.58 ± 0.27	54.72 ± 0.45	44.29 ± 1.18
9f	F	H	H	*	16.60 ± 0.53	29.87 ± 0.97
9g	SMe	H	H	40.69 ± 5.98	45.93 ± 8.35	50.34 ± 7.70
14	-	-	-	13.98 ± 0.50	34.15 ± 0.66	40.51 ± 0.14
4-Chlorobiphenyl				49.65 ± 0.49	60.63 ± 8.62	61.64 ± 8.26
4-Bromobiphenyl				54.01 ± 2.25	64.37 ± 4.75	64.67 ± 1.89
4-Fluorobiphenyl				36.36 ± 3.11	48.85 ± 5.63	52.20 ± 2.77

4-Iodobiphenyl	37.21 ± 4.36	41.90 ± 4.94	60.56 ± 2.04
4-Bromo-4’-methoxybiphenyl	52.70 ± 0.29	59.17 ± 0.74	61.07 ± 2.02
4-Cyanobiphenyl	44.08 ± 5.49	50.89 ± 4.89	51.93 ± 0.57
Biphenyl	42.06 ± 0.56	52.02 ± 0.80	53.08 ± 2.54
Honokiol	44.83 ± 1.40	58.16 ± 3.63	77.75 ± 2.82
Magnolol	31.25 ± 7.41	45.72 ± 3.34	67.77 ± 4.84
MB	92.53 ± 3.25	96.97 ± 1.84	99.36 ± 0.46

Results expressed as average ± SD of two separate experiments (n = 3), obtained from ThT-monitored 24 h aggregation kinetics of $A\beta_{1-40}$ *(5 μM) in the presence of 1, 5 and 25 μM of compound at pH 7.4, 37 °C in phosphate buffer.*Promotes aggregation.*

Aggregation kinetics data for all tested compounds show that compounds exhibited a concentration dependent decline in ThT fluorescence and were able to prevent $A\beta_{1-40}$ fibrillogenesis, with maximum inhibition observed at 25 μM (~26–79% inhibition). Table 4.1 provides a summary for all the compounds tested at concentrations 1, 5, and 25 μM, with methylene blue used as a reference compound. All ethynyl-1,1’-biphenyl derivatives were observed to have inhibitory activity toward $A\beta_{1-40}$, with the only exception being 3-ethynyl-1,1’-biphenyl derivative **6f**, which was observed to promote $A\beta_{1-40}$ fibrillogenesis at 1 μM concentration. In addition, honokiol, magnolol, unsubstituted biphenyl, cyanobiphenyl and halogenated biphenyl compounds, were also observed to show anti-$A\beta_{1-40}$ aggregation properties. Figure 4.1 shows the % inhibition of ThT fluorescence intensity in the presence of $A\beta_{1-40}$ (5 μM) for various tested compounds at 25 μM, and their corresponding % inhibition of $A\beta_{1-40}$ fibrillogenesis.

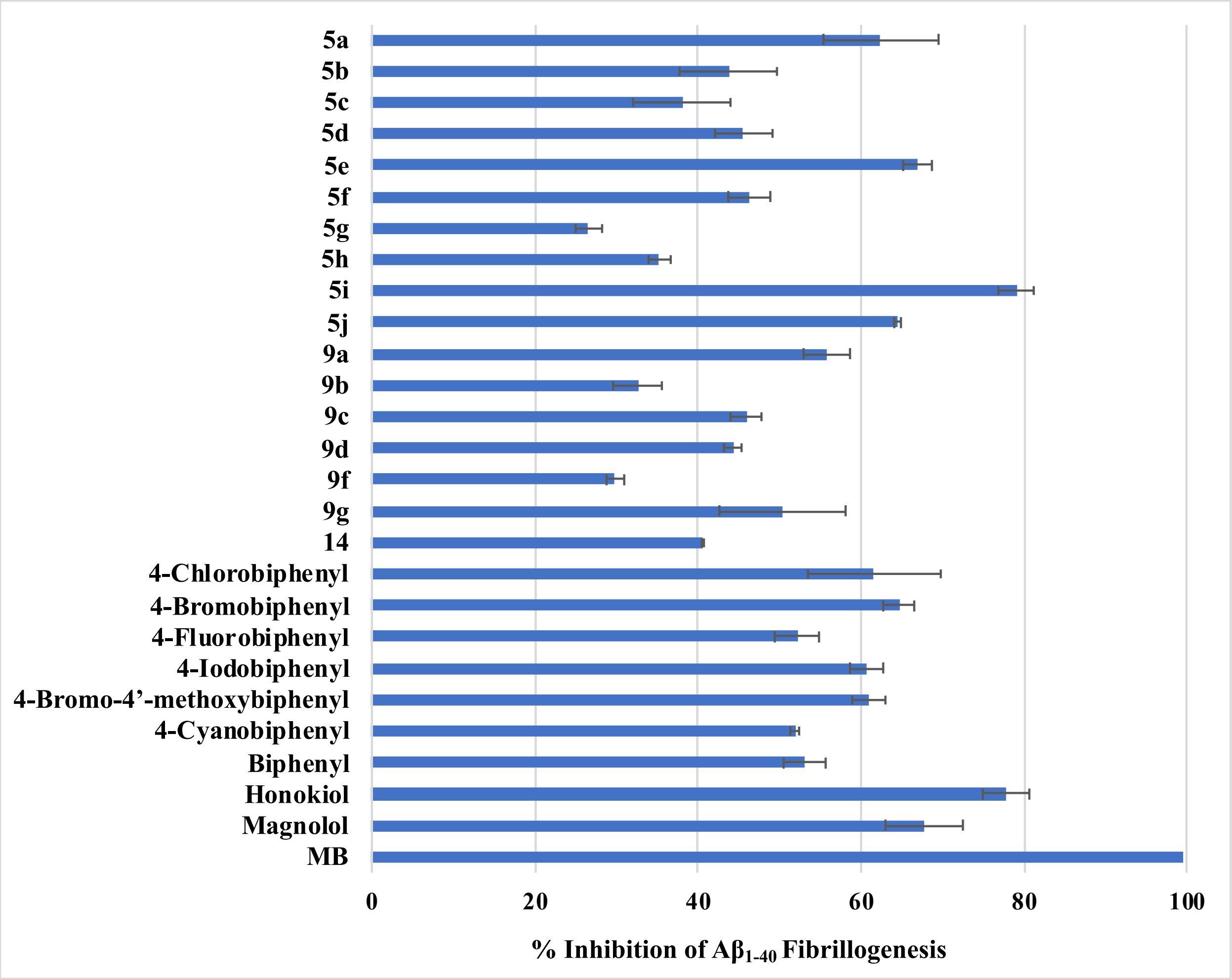

Figure 4.1. The percent inhibition of ThT fluorescence intensity in the presence of Aβ_{1-40} (5 μM) incubated with ethynyl-1,1’-biphenyl derivatives (**5a-j, 9a-g, 14**) and halogenated biphenyl, cyanobiphenyl derivatives, biphenyl, honokiol, magnolol and MB at 25 μM in phosphate buffer pH 7.4, 37 °C after 24 h.

The 24 h ThT-based aggregation kinetics data of Aβ_{1-40} (5 μM) in the presence of **5a** (4-ethynyl-1,1'-biphenyl) and reference agent MB is shown as representative examples in Figure 4.2. The aggregation kinetic curve for Aβ_{1-40} alone shows the characteristic trend with an initial lag phase lasting approximately for 8 h, followed by a rapid elongation phase and finally, exhibiting a saturation phase after approximately 16 h, indicating the formation of mature Aβ_{1-40} fibrils (Figure

4.2). In the presence of compound **5a**, a concentration dependent decline in ThT fluorescence was observed and was able to prevent A$\beta_{1\text{-}40}$ fibrillogenesis (~39–62% inhibition, Table 4.2 and Panel A, Figure 4.2). Maximum inhibition was seen at 25 μM (62% inhibition, Panel A, Figure 4.2).

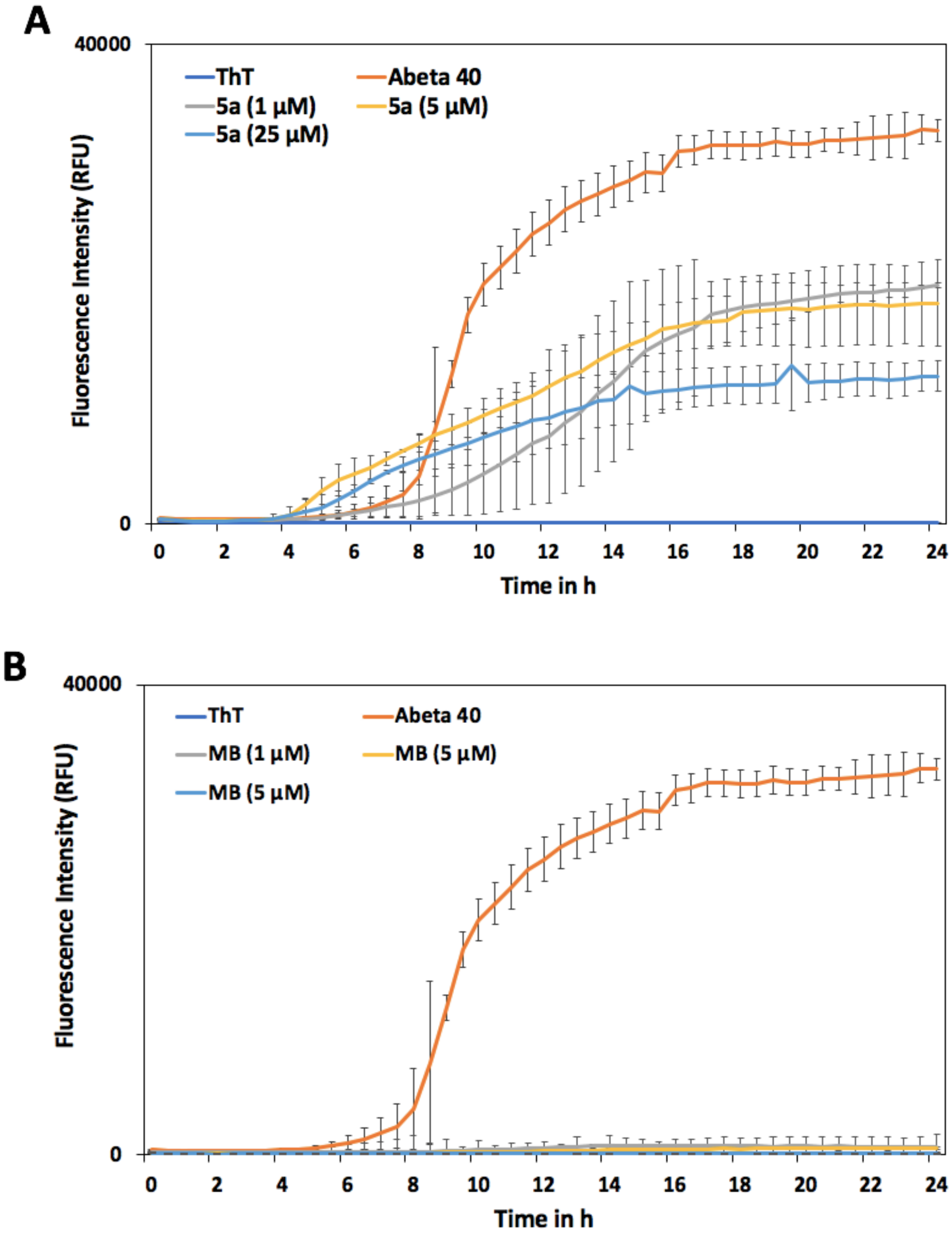

Figure 4.2. Panels A and B show ThT-monitored 24 h aggregation kinetics of A$\beta_{1\text{-}40}$ (5 µM) in the presence of 1, 5 and 25 µM of ethynyl-1,1'-biphenyl derivatives **5a** and MB respectively, at pH 7.4, 37 °C, phosphate buffer.

Compared to ethynylbiphenyl derivative **5a**, the 4-pyridyly containing compound **5i** (4-(4-ethynylphenyl)pyridine) exhibited better inhibition of A$\beta_{1\text{-}40}$ aggregation (Table 4.2) and was the most potent inhibitor, with 79.08% inhibition of A$\beta_{1\text{-}40}$ observed at 25 µM, however, it was not as effective as MB (~99% inhibition at 25 µM) in preventing A$\beta_{1\text{-}40}$ aggregation. Chemically, derivative **5i** contains a pyridine ring (Table 4.1). While similar to the benzene, the nitrogen atom within the pyridine ring contains a lone pair of electrons that can undergo additional hydrogen-bonding (H-bonding) interactions within the A$\beta_{1\text{-}40}$ dimer species, thus stabilizing these aggregates and reducing their fibrillogenesis. A detailed analysis of the binding interactions of **5i** and other derivatives with A$\beta_{1\text{-}40}$ aggregates is discussed in section 4.2. Evaluating the anti-A$\beta_{1\text{-}40}$ aggregation properties of the other pyridine containing derivative, 3-(4-ethynylphenyl)pyridine (**5j**), at the same concentration range (1–25 µM), shows that compound **5j** was also a slightly better inhibitor than **5a** at 25 µM (64% inhibition). However it was not as effective as compound **5i**. In contrast, the corresponding regioisomer compound **14** (2-ethynyl-5-phenylpyridine) was observed to be an even weaker inhibitor of A$\beta_{1\text{-}40}$ fibrillogenesis compared to both **5j** and **5i**, with an observed inhibition activity of ~13–40% (Table 4.2).

Ethynylbiphenyl derivatives with electron-donating groups (EDGs) **5b, 5c,** and **5d**; containing 2-methoxy, 4-methoxy and 3,4-dimethoxy substituents, were observed to exhibit inhibition profiles similar to compound **14** at 25 µM (~38–45% inhibition). Among the three derivatives, the *ortho*-substituted methoxy derivative (**5c**) exhibited the weakest inhibition toward A$\beta_{1\text{-}40}$ fibrillogenesis with a maximum inhibition of 38% at 25 µM, followed by the *para*-

substituted methoxy derivative (**5b**), which exhibited superior inhibition of A$\beta_{1\text{-}40}$ fibrillogenesis at 25 μM (43% inhibition), and lastly, the 3,4-dimethoxy substituent containing derivative **5d** was observed to have slightly better inhibition at 25 μM (45% inhibition). Interestingly, EDG-based derivative **5e**, containing a *para*-substituted hydroxy, exhibited an excellent inhibition profile (~18–66% inhibition), and was observed to be a better inhibitor of A$\beta_{1\text{-}40}$ fibrillogenesis at 25 μM (66% inhibition). It was not as potent as the reference agent MB (99.3% inhibition at 25 μM, Table 4.2).

EWG-based derivative **5f**, containing a *para*-substituted fluoro moiety, was observed to have an inhibition profile similar to EDG-based derivatives **5b, 5c,** and **5d**; with a maximum inhibition of 46% at 25 μM. In contrast, derivative **5g**, containing a *para*-substituted thiomethyl moiety, was observed to show weaker inhibition toward A$\beta_{1\text{-}40}$ fibrillogenesis, with a maximum inhibition of 26% at 25 μM. However, oxidation of the sulfur atom gave sulfonylmethyl containing derivative **5h** which exhibited better inhibition of A$\beta_{1\text{-}40}$ at 25 μM (35% inhibition) compared to compound **5g** (Table 4.2).

As part of the SAR study, when the ethynyl-substituent was moved from C4 to C3-position in derivatives **9a**-**g**, it led to a decline in A$\beta_{1\text{-}40}$ aggregation inhibition compared to the corresponding 4-ethynyl-1,1'-biphenyl derivatives (**5a-j**, Table 4.2**)**. Derivatives **9a-g** exhibited ~29 – 55% inhibition in A$\beta_{1\text{-}40}$ fibrillogenesis at the 24 h time point. Unsubstituted 3-ethynyl-1,1'-biphenyl derivative (**9a**) exhibited superior inhibition among 3-ethynyl-1,1'-biphenyl derivative, with a maximum inhibition of 55% at 25 μM. It was less effective compared to the 4-ethynyl-1,1'-biphenyl derivative (**5a**) at 25 μM (62% inhibition, Table 4.2). EDG-based derivatives **9b, 9c,** and **9d**, containing methoxy and dimethoxy substituents, were observed to exhibit an inhibition profile similar to the methoxy substituted 4-ethynyl-1,1'-biphenyl derivative (**5b, 5c** and **5d**) at 25 μM

(~32–44% inhibition). The same pattern was also observed, wherein the 3,4-dimethoxy substituent (**9d**) was observed to have the best inhibition at 25 μM (44% inhibition), among the methoxy-substituted 3-ethynyl-1,1'-biphenyl derivatives (**9b-d**).

In contrast to the 4-ethynyl-1,1'-biphenyl derivative **5f**, which exhibited a maximum inhibition of 46% at 25 μM; the corresponding regioisomer 3-ethynyl-1,1'-biphenyl derivative **9f**, exhibited weaker inhibition of $A\beta_{1-40}$ at 25 μM (29% inhibition, Table 4.2). The 4-thiomethyl containing derivative **5g** was a weaker inhibitor compared to the corresponding regioisomer **9g** which exhibited better inhibition at 25 μM (~50% inhibition). In general, compounds with superior $A\beta_{1-40}$ aggregation inhibition were identified in the 4-ethynylbiphenyl series.

As discussed previously, naturally occurring compounds, honokiol and magnolol, are known $A\beta_{1-40}$ inhibitors. It came as no surprise to see that both honokiol and magnolol exhibited excellent inhibition of $A\beta_{1-40}$ aggregation (Table 4.2) and it was observed that honokiol was a better inhibitor of $A\beta_{1-40}$ fibrillogenesis at 25 μM (78% inhibition). Its isomer, magnolol was also observed to be strong inhibitor $A\beta_{1-40}$ fibrillogenesis at 25 μM (68% inhibition). In comparison to the unsubstituted 4-ethynyl-1,1'-biphenyl derivative (**5a**, 62% inhibition) and the unsubstituted 3-ethynyl-1,1'-biphenyl derivative (**9a**, 55% inhibition), both honokiol and magnolol were observed to be better inhibitors of $A\beta_{1-40}$ fibrillogenesis at 25 μM. Interestingly, the unsubstituted biphenyl also exhibited inherent anti-$A\beta_{1-40}$ aggregation activity with inhibition range of 42–58% (Table 4.2). It was observed that the addition of the ethynyl moiety led to an increase in the anti-$A\beta_{1-40}$ aggregation activity at 25 μM (compound **5a**, 62% inhibition, Table 4.2).

Halogenated biphenyl compounds, 4-bromobiphenyl, 4-bromo-4'-methoxybiphenyl, 4-chlorobiphenyl, 4-iodobiphenyl, and 4-fluorobiphenyl (Table 4.2), were also tested against $A\beta_{1-40}$ at the same concentration range (1–25 μM). All compounds exhibited inhibition toward $A\beta_{1-40}$

fibrillogenesis, with a range of 52–64% inhibition at 25 μM, which was very similar to the unsubstituted 4-ethynyl-1,1'-biphenyl derivative (**5a**, 62% inhibition, Table 4.2). Among the halogenated biphenyls, the 4-bromobiphenyl compound was the best inhibitor with a 64% inhibition at 25 μM. Interestingly, its methoxy substituted derivative, 4-bromo-4'-methoxybiphenyl, exhibited a lower inhibition profile (52–61% inhibition). The 4-cyanobiphenyl was a less potent inhibitor of $A\beta_{1-40}$ fibrillogenesis compared to halogenated compounds with 44 – 51% inhibition range. While the cyano moiety is similar to the ethynyl moiety, in that, it consists of a carbon and nitrogen group joined via a triple bond; it differs as it is an EWG substituent that can undergo polar or H-bonding interactions. When comparing 4-cyanobiphenyl with the unsubstituted 4-ethynyl-1,1'-biphenyl derivative at 25 μM (**5a**, 62% inhibition), 4-cyanobiphenyl exhibited ~52% inhibition of $A\beta_{1-40}$ fibrillogenesis; thus, indicating that the ethynyl containing compound **5a** exhibited better inhibition.

Generally, it was evident that better anti-$A\beta_{1-40}$ aggregation activity was observed for 4-ethynyl-1,1'-biphenyl derivatives whereas the presence of a 4-pyridine bioisostere in compound **5i** (4-(4-ethynylphenyl)pyridine) provided maximum $A\beta_{1-40}$ aggregation inhibition. The results also show that ethynylbiphenyl system serves as a suitable template to design small molecules as inhibitors of $A\beta_{1-40}$ aggregation and that an ethynyl-substituent is a suitable bioisostere for halogen and cyano-containing biphenyls. It should be noted that polychlorinated and polybrominated biphenyls (PCBs and PBBs) are known to be toxic to humans and are classified as environmental toxins which suggests their unsuitability in drug design and development[176-178] This study shows that modifying the biphenyls with an ethynyl-substituent is a novel strategy to develop potential drug candidates.

4.1.2. Anti-Aβ_{1-42} aggregation activity

The ThT-based Aβ_{1-42} aggregation kinetics was carried out in the presence of the ethynyl-1,1'-biphenyl derivatives (**5a-j, 9a-g, 14**), halogenated biphenyls, cyano-biphenyl and reference compound over a period of 24 h, and results are provided in Table 4.2.

Table 4.2: Inhibition data for ethynyl-1,1'-biphenyl derivatives **5a-j, 9a-g, 14** and other biphenyl derivatives toward Aβ_{1-42}. .

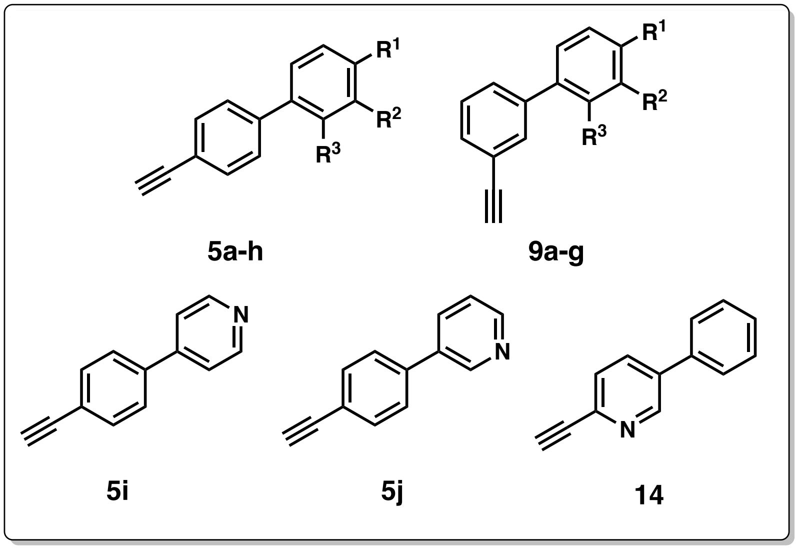

	R¹	**R²**	**R³**
a	H	H	H
b	OMe	H	H
c	H	H	OMe
d	OMe	OMe	H
e	OH	H	H
f	F	H	H
g	SMe	H	H
h	SO_2Me	H	H

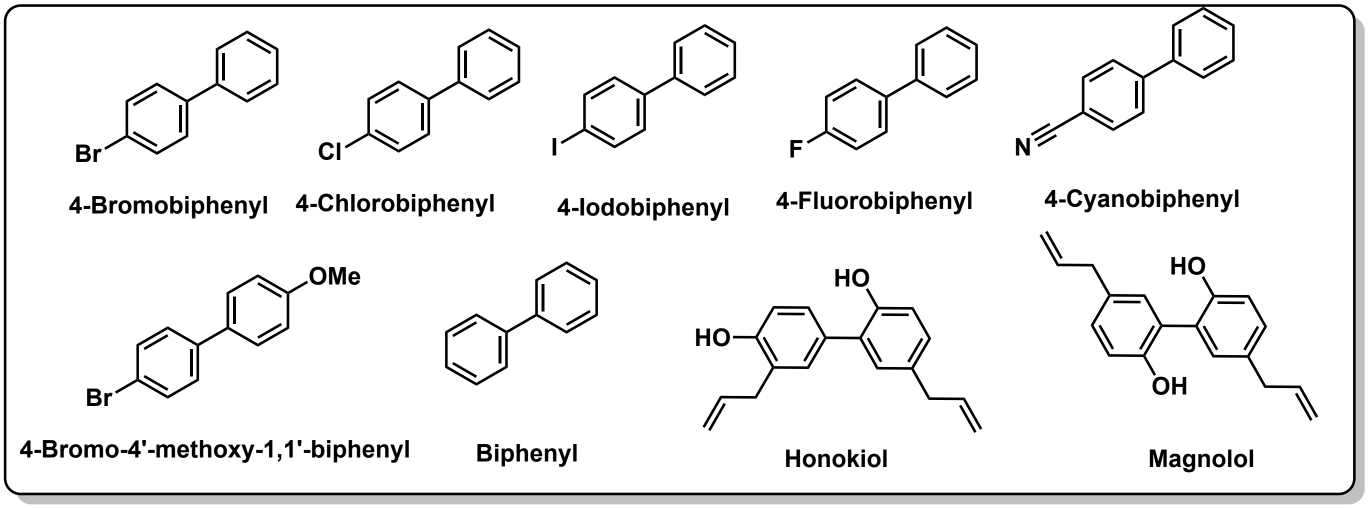

Compound	**R¹**	**R²**	**R³**	**% Inhibition (1 µM)**	**% Inhibition (5 µM)**	**% Inhibition (25 µM)**
5a	H	H	H	71.91 ± 7.39	79.58 ± 0.64	83.56 ± 0.41
5b	OMe	H	H	48.05 ± 2.39	74.78 ± 4.30	86.38 ± 3.66
5c	H	H	OMe	71.48 ± 2.48	78.27 ± 13.57	84.28 ± 1.81
5d	OMe	OMe	H	26.18 ± 0.21	40.08 ± 1.51	56.90 ± 9.07
5e	OH	H	H	55 ± 1.60	70.31 ± 1.37	79.55 ± 0.45
5f	F	H	H	65.71 ± 13.84	68.10 ± 9.54	79.08 ± 1.80
5g	SMe	H	H	63.71 ± 1.26	68.77 ± 0.16	78.28 ± 0.42
5h	SO_2Me	H	H	69.19 ± 0.84	76.51 ± 1.54	80.96 ± 0.25
5i	H	H	H	81.72 ± 0.58	83.43 ± 6.83	85.80 ± 0.75
5j	H	H	H	62.28 ± 0.14	63.34 ± 1.71	79.64 ± 0.19
9a	H	H	H	77.62 ± 5.55	83.82 ± 2.54	86.25 ± 1.63
9b	OMe	H	H	59.02 ± 0.91	73.46 ± 1.32	84.76 ± 2.91
9c	H	H	OMe	72.44 ± 6.32	82.52 ± 5.53	83.82 ± 3.01
9d	OMe	OMe	H	68.34 ± 2.31	72.26 ± 5.97	77.63 ± 3.25
9f	F	H	H	80.50 ± 0.11	81.79 ± 2.88	85.36 ± 1.97
9g	SMe	H	H	47.43 ± 4.17	67.03 ± 3.65	86.97 ± 2.04
14	H	H	H	63.71 ± 2.44	68.77 ± 3.05	78.28 ± 1.09
4-Chlorobiphenyl				55.94 ± 3.07	84.26 ± 7.09	84.86 ± 0.39
4-Bromobiphenyl				79.88 ± 1.83	82.67 ± 6.66	88.61 ± 1.21
4-Fluorobiphenyl				84.67 ± 2.23	86.93 ± 3.28	88.68 ± 4.92

4-Iodobiphenyl	79.39 ± 4.59	83.06 ± 5.67	84.67 ± 3.47
4-Bromo-4’-methoxybiphenyl	74.43 ± 1.48	81.79 ± 4.19	59.66 ± 0.11
4-Cyanobiphenyl	82.46 ± 1.83	84.27 ± 3.39	85.78 ± 3.39
Biphenyl	35.89 ± 1.30	54.39 ± 0.16	61.24 ± 0.48
Honokiol	77.39 ± 1.48	83.96 ± 4.19	89.34 ± 0.11
Magnolol	82.22 ± 5.01	85.35 ± 3.02	85.83 ± 0.09
MB	97.83 ± 1.06	98.34 ± 0.52	98.22 ± 0.26

Results expressed as average ± SD of two separate experiments (n = 3), obtained from ThT-monitored 24 h aggregation kinetics of $A\beta_{1-42}$ *(5 μM) in the presence of 1, 5 and 25 μM of compound at pH 7.4, 37 °C in phosphate buffer.*

Aggregation kinetics data for all tested compounds show that compounds exhibited a concentration dependent decline in ThT fluorescence and were able to prevent $A\beta_{1-42}$ fibrillogenesis, with maximum inhibition observed at 25 μM (~56–89% inhibition). Figure 4.3 displays the percent inhibition of ThT fluorescence intensity in the presence of $A\beta_{1-42}$ (5 μM) and the various tested compounds at 25 μM.

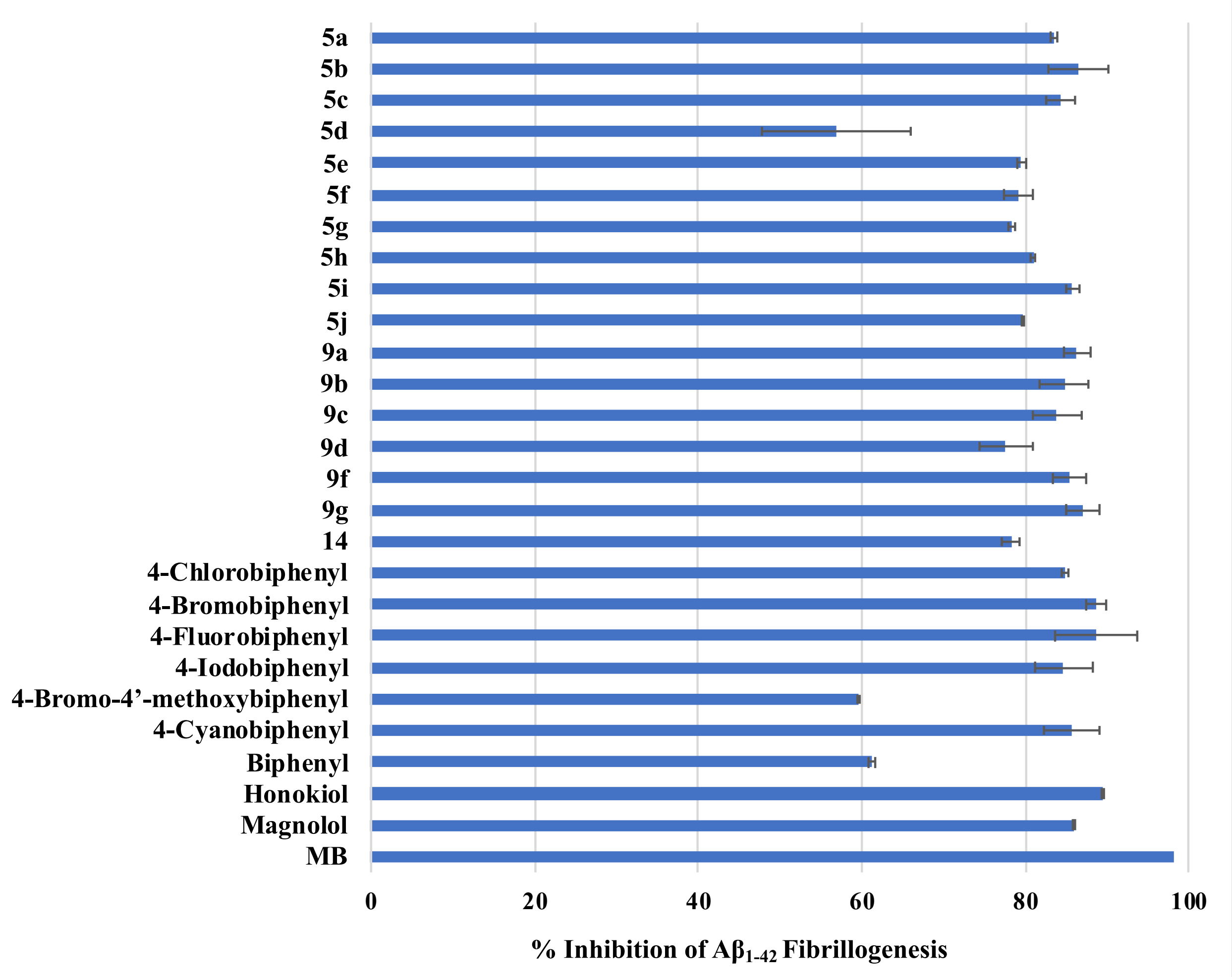

Figure 4.3. The percent inhibition of ThT fluorescence intensity in the presence of Aβ_{1-42} (5 µM) incubated with ethynyl-1,1'-biphenyl derivatives (**5a-j, 9a-g, 14**) and halogenated biphenyl, cyanobiphenyl derivatives, biphenyl, honokiol, magnolol and MB at 25 µM in phosphate buffer pH 7.4, 37 °C after 24 h.

Aggregation kinetic data for compound **5a** (4-ethynyl-1,1'-biphenyl) and reference agent MB is shown in Figure 4.4 as representative examples. The control aggregation kinetics curve for Aβ_{1-42} (5 µM) shows that it tends to aggregate at a faster pace compared to Aβ_{1-40} (Figure 4.4). The lag phase was very short (~2 h), followed by a rapid elongation phase lasting for ~10 h before reaching the saturation phase.

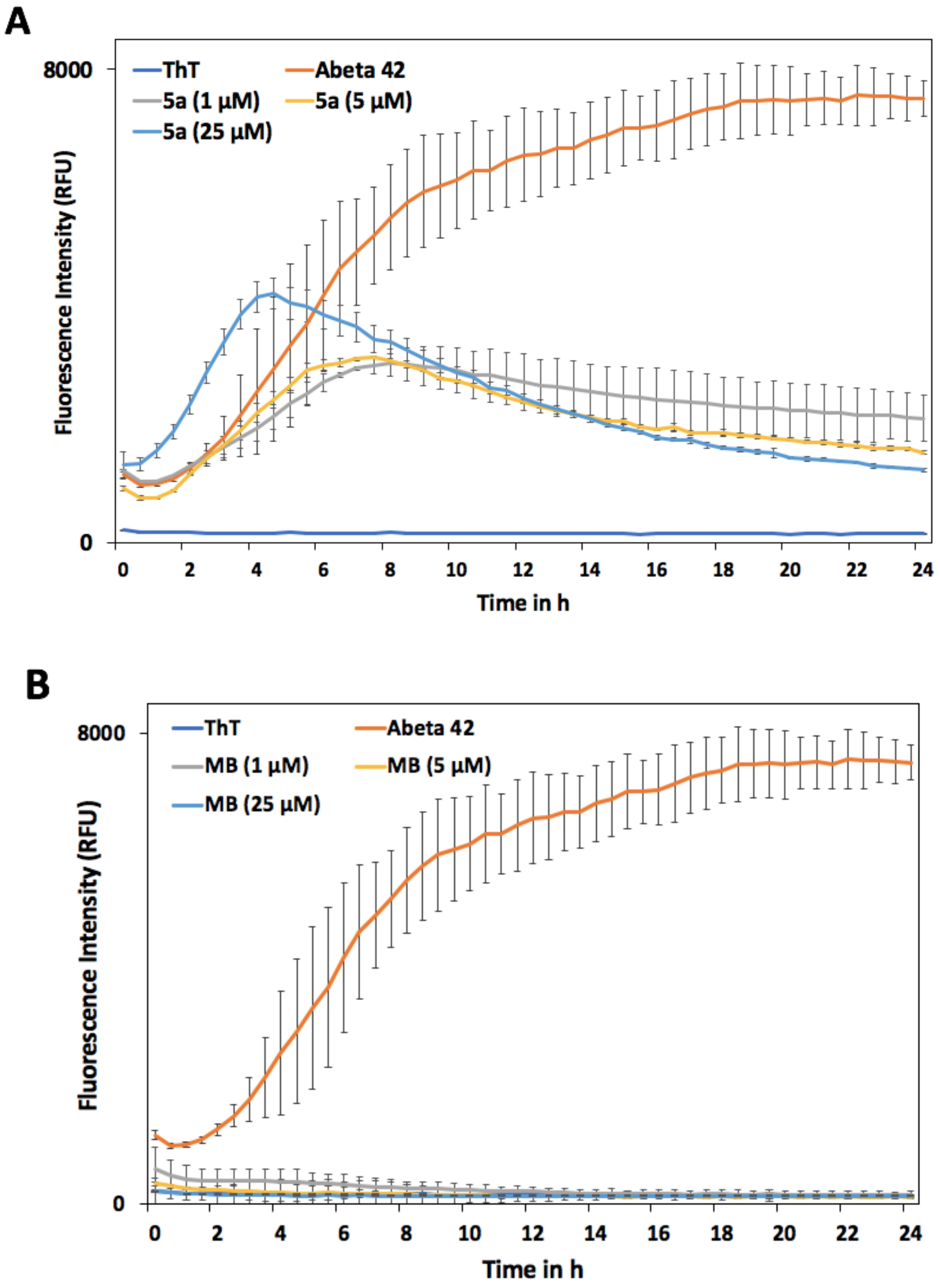

Figure 4.4. Panels A and B show ThT-monitored 24 h aggregation kinetics of Aβ_{1-42} (5 μM) in the presence of 1, 5 and 25 μM of 4-ethynyl-1,1'-biphenyl derivatives **5a** and MB, at pH 7.4, 37 °C in phosphate buffer.

Upon initial observation, all tested compounds exhibited greater inhibition toward Aβ_{1-42} over Aβ_{1-40} inhibition. In the presence of 25 μM of 4-ethynyl-1,1'-biphenyl derivatives (**5a-j**), there was a decline in ThT fluorescence intensity, with a range of 56–86% inhibition in A$\beta_{1\text{-}42}$ fibrillogenesis at the 24 h time point; in comparison to an A$\beta_{1\text{-}40}$ inhibition range of ~26–79% inhibition. Aggregation kinetics data for the unsubstituted 4-ethynyl-1,1'-biphenyl derivative (**5a**) shows that it exhibited a concentration dependent decline in ThT fluorescence and was able to prevent A$\beta_{1\text{-}42}$ fibrillogenesis (~71–83% inhibition, Panel A, Figure 4.4). In this case, derivative **5a** was observed to be a stronger inhibitor of A$\beta_{1\text{-}42}$, in comparison to A$\beta_{1\text{-}40}$ (62% inhibition at 25 μM, Table 4.1).

Consistent with the results observed with A$\beta_{1\text{-}40}$, **5i** (4-(4-ethynylphenyl)pyridine) was also observed to be a better inhibitor of A$\beta_{1\text{-}42}$ aggregation, with 85% inhibition observed at 25 μM. However, it was not as effective as MB (~98% inhibition at 25 μM, Table 4.2). Other pyridine containing derivatives **5j** and **14** exhibited excellent inhibition of A$\beta_{1\text{-}42}$ aggregation (79% and 61% inhibition at 25 μM respectively, Table 4.2) although were less effective as compared to **5a** (83% inhibition at 25 μM).

While 2-methoxy, 4-methoxy and 3,4-dimethoxy containing derivatives (**5b, 5c,** and **5d**) were observed to exhibit weaker A$\beta_{1\text{-}40}$ inhibition profile at 25 μM (~38–45% inhibition, Table 4.1), these derivatives exhibited excellent A$\beta_{1\text{-}42}$ inhibition profile at 25 μM (~56–86% inhibition, Table 4.2). In this case, however, the *para*-substituted methoxy derivative (**5b**) exhibited the highest activity toward A$\beta_{1\text{-}42}$ fibrillogenesis with a maximum inhibition of 86% at 25 μM, followed by the *ortho*-substituted methoxy derivative (**5c**, 84% inhibition, Table 4.2). In contrast, the 3,4-dimethoxy derivative (**5d**) was observed to exhibit the lower inhibitory activity toward A$\beta_{1\text{-}42}$ fibrillogenesis at 25 μM (56% inhibition). Similarly, compound **5e** with an EDG, containing a *para*-substituted hydroxy, derivative exhibited excellent inhibition (~54–79% inhibition at 25 μM) and was a slightly weaker inhibitor in comparison to unsubstituted 4-ethynyl-1,1'-biphenyl derivative **5a** (83% inhibition at 25 μM, Table 4.2). Comparable results were observed for EWG-based derivative **5f**, containing a *para*-substituted fluoro moiety, with a maximum inhibition of 79% at 25 μM. Compound **5g**, containing a *para*-substituted thiomethyl group which showed weaker inhibition of $A\beta_{1-40}$ fibrillogenesis (26% at 25 μM) exhibited superior inhibition of $A\beta_{1-42}$ fibrillogenesis, with a maximum inhibition of 78% observed at 25 μM (Table 4.2). Similar to results observed for $A\beta_{1-40}$ inhibition rates, the oxidation of the sulfur atom enhanced the $A\beta_{1-42}$ inhibition activity as seen with compound **5h** (80% inhibition at 25 μM).

The 3-ethynyl-1,1'-biphenyl derivatives (**9a-g**) exhibited excellent inhibition of $A\beta_{1-42}$ with a range of 77 – 86% inhibition at the 24 h time point. Similar to the results observed for aggregation kinetics data of $A\beta_{1-40}$, unsubstituted 3-ethynyl-1,1'-biphenyl derivative (**9a**) was observed to be one of the most potent of the 3-ethynyl-1,1'-biphenyl derivatives, with a maximum inhibition of 86% at 25 μM. Derivative **9g**, containing a *para*-substituted thiomethy group, was also exhibited similar activity with 47-86% inhibition range (Table 4.2). The 3-ethynylbiphenyl derivatives with EDGs **9b, 9c,** and **9d**; containing 2-methoxy, 4-methoxy and 3,4-dimethoxy substituents, were observed to exhibit an $A\beta_{1-42}$ inhibition profile similar to the methoxy substituted 4-ethynyl-1,1'-biphenyl derivatives (**5b, 5c** and **5d**) at 25 μM (~77–84% inhibition). Presence of an EWG in compound **9f** (3-ethynyl-4'-fluoro-1,1'-biphenyl) exhibited excellent inhibition of $A\beta_{1-42}$ at 25 μM (85% inhibition, Table 4.2).

Even the biphenyl compound exhibited inherent inhibition of $A\beta_{1-42}$ fibrillogenesis (36 - 61% inhibition, Table 4.2). However, it was much weaker compared to ethynylbiphenyl derivatives. This also confirms that the addition of ethynyl moiety appears to increase both anti-$A\beta_{1-40}$ and $A\beta_{1-40}$ fibrillogenesis activity.

The natural biphenyl derivatives honokiol and magnolol were observed to be excellent inhibitors of Aβ_{1-42} fibrillogenesis at 25 μM (89% inhibition and 85% inhibition, respectively, Table 4.2) with slightly better inhibition compared to **5a** at 25 μM.

Halogenated biphenyl compounds (4-bromobiphenyl, 4-bromo-4'-methoxybiphenyl, 4-chlorobiphenyl, 4-iodobiphenyl, and 4-fluorobiphenyl) were also tested against Aβ_{1-42} at the same concentration range (1–25 μM), and all compounds exhibited inhibition toward Aβ_{1-42} fibrillogenesis, with a range of 59–88% inhibition at 25 μM, which was very similar to the unsubstituted derivatives **5a** and **9a** (83% and 86% inhibition). Again, it was observed that the most potent inhibitor among these compounds was the 4-bromobiphenyl which exhibited 88% inhibition at 25 μM (Table 4.2).The addition of a bromine-substituent at 4-position led to a decrease in the inhibition activity (59% inhibition at 25 μM, Table 4.2) in the 4-bromo-4'-methoxybiphenyl compound.. The presence of a 4-cyano-group in the 4-cyanobiphenyl compound exhibited excellent inhibition range as well (82 – 85% inhibition, Table 4.2).

Generally, it is apparent that the synthesized ethynyl-1,1'-biphenyl derivative library, as well as the various biphenyl compounds exhibit a higher selectivity toward Aβ_{1-42} inhibition over Aβ_{1-40} inhibition. The 4-ethynylbiphenyl derivatives **5b, 5i**, and 3-ethynylbiphenyl derivatives **9a** and **9g** were identified as compounds with excellent inhibition of Aβ_{1-42} aggregation (~86 % inhibition at 25 μM). The results also show that halogenated biphenyls and the natural biphenyl (honokiol and magnolol) exhibited excellent inhibition properties (84 – 88 % inhibition at 25 μM) whereas the ethynylbiphenyl derivatives **5a-j**, **9a-g** and **14** exhibited 56 - 87% inhibition at 25 μM demonstrating the utility of biphenyl rings and the ethynyl-substituent in the design and development of novel Aβ aggregation inhibitors. This study also highlights the suitability of ethynyl-substituent as a bioisostere for halogens and cyano-substituent in designing biphenyl-based Aβ aggregation inhibitors.

4.1.3. Transmission electron microscopy (TEM) studies

TEM studies were used to investigate and assess the morphology of $A\beta_{1-40}$ and $A\beta_{1-42}$ aggregates after incubating them with ethynyl-1,1'-biphenyl derivatives to study their effect on Aβ. Images obtained from this qualitative technique is used to validate and confirm the results observed in the ThT-based fluorescence assay. The ethynylbiphenyl derivatives **5a-c**, **5e**, **5i**, **5j**, **9a**, **9f**, **9g** and **honokiol** were used as representative examples. After 24 h incubation, $A\beta_{1-40}$ control (5 μM) formed distinct fibrils in the absence of any test compounds (Figure 4.5A). Co-incubation of $A\beta_{1-40}$ with **5a** (25 μM) led to a reduction in $A\beta_{1-40}$ fibril load, which further confirms its anti-$A\beta_{1-40}$ aggregation property (Figure 4.5C). The pyridine containing compounds (**5i** and **5j**), the phenolic derivative **5i** and the 3-ethynyl derivative **9a** also were able to reduce $A\beta_{1-40}$ load at 25 μM (Figure 4.5B, 4.5F, 4.5E and 4.5D, respectively). The reference compound honokiol exhibited significant inhibition of $A\beta_{1-40}$ fibrillogenesis at 25 μM (Figure 4.5G), leading to a reduction in $A\beta_{1-40}$ fibril formation, providing further evidence on the anti-aggregation properties of these ethynylbiphenyl derivatives.

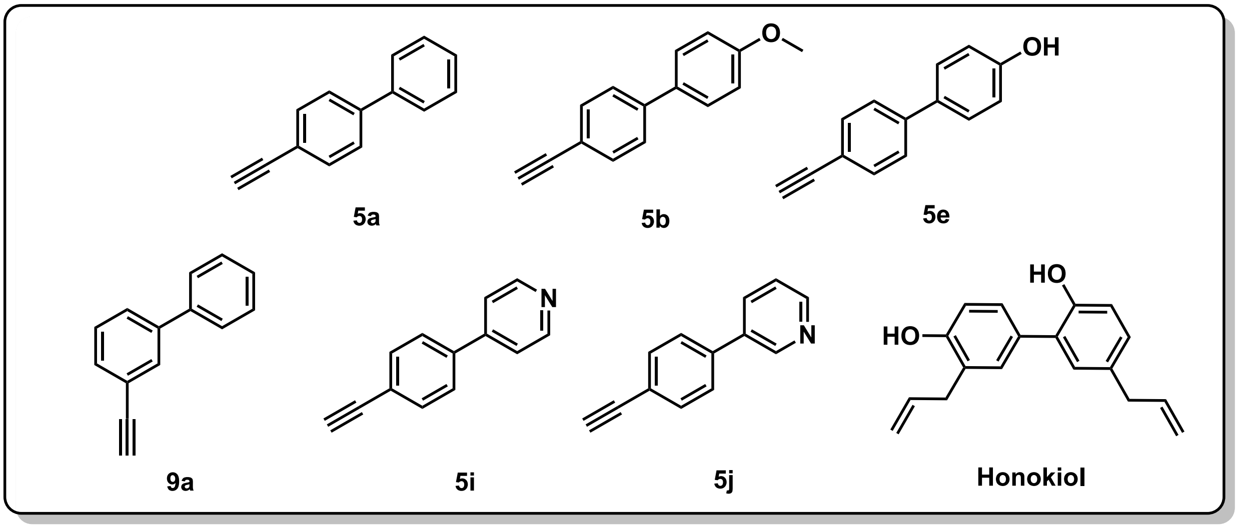

5a

5b

5e

9a

5i

5j

Honokiol

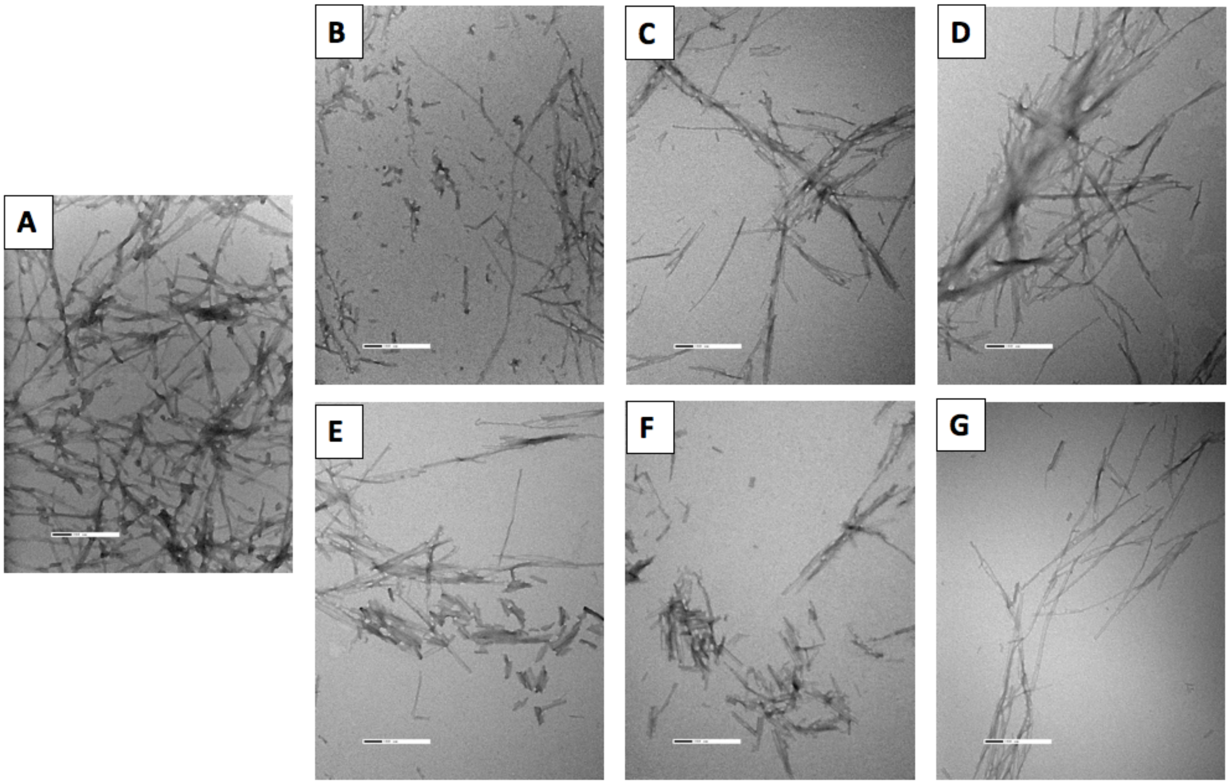

Figure 4.5. TEM images of A$\beta_{1\text{-}40}$ alone (5 µM) after 24 h incubation at 37 °C (Panel A), A$\beta_{1\text{-}40}$ + **5i** (25 µM, Panel B), A$\beta_{1\text{-}40}$ + **5a** (25 µM, Panel C), A$\beta_{1\text{-}40}$ + **9a** (25 µM, Panel D), A$\beta_{1\text{-}40}$ + **5e** (25 µM, Panel E), A$\beta_{1\text{-}40}$ + **5j** (25 µM, Panel F), and A$\beta_{1\text{-}40}$ + **honokiol** (25 µM, Panel G). Scale - 100 nm.

TEM studies of $A\beta_{1-42}$ alone (5 µM) showed the formation of fibrils after 24 h incubation at 37 °C (Figure 4.6A). Co-incubation with **5b** (25 µM) for 24 h, led to a drastic reduction in $A\beta_{1-42}$ fibril formation (Figure 4.6C). Similarly, co-incubation with **5i** (25 µM, Panel B), **5c** (25 µM, Panel D), **9a** (25 µM, Panel E), **9f** (25 µM, Panel F) and **9g** (25 µM, Panel G) for 24 h, led to a noticeable reduction in $A\beta_{1-42}$ fibril formation, thus confirming the anti-$A\beta_{1-42}$ aggregation properties of ethynylbiphenyl derivatives.

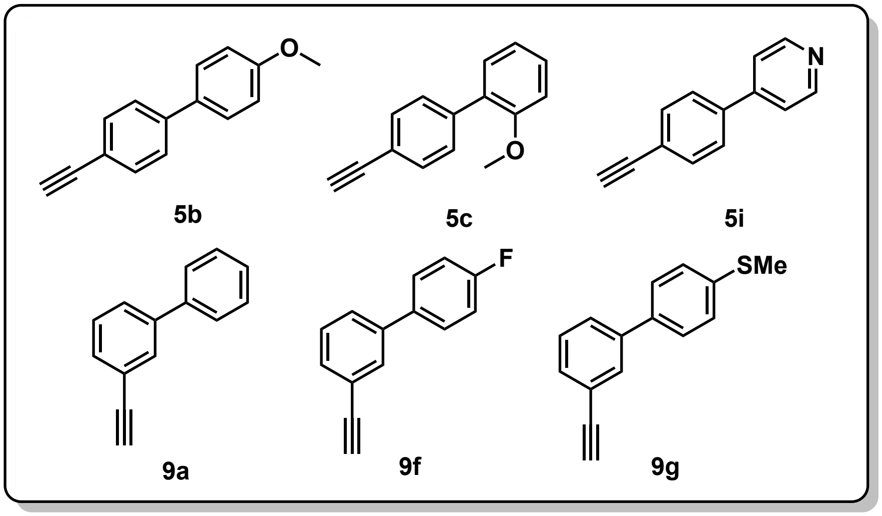

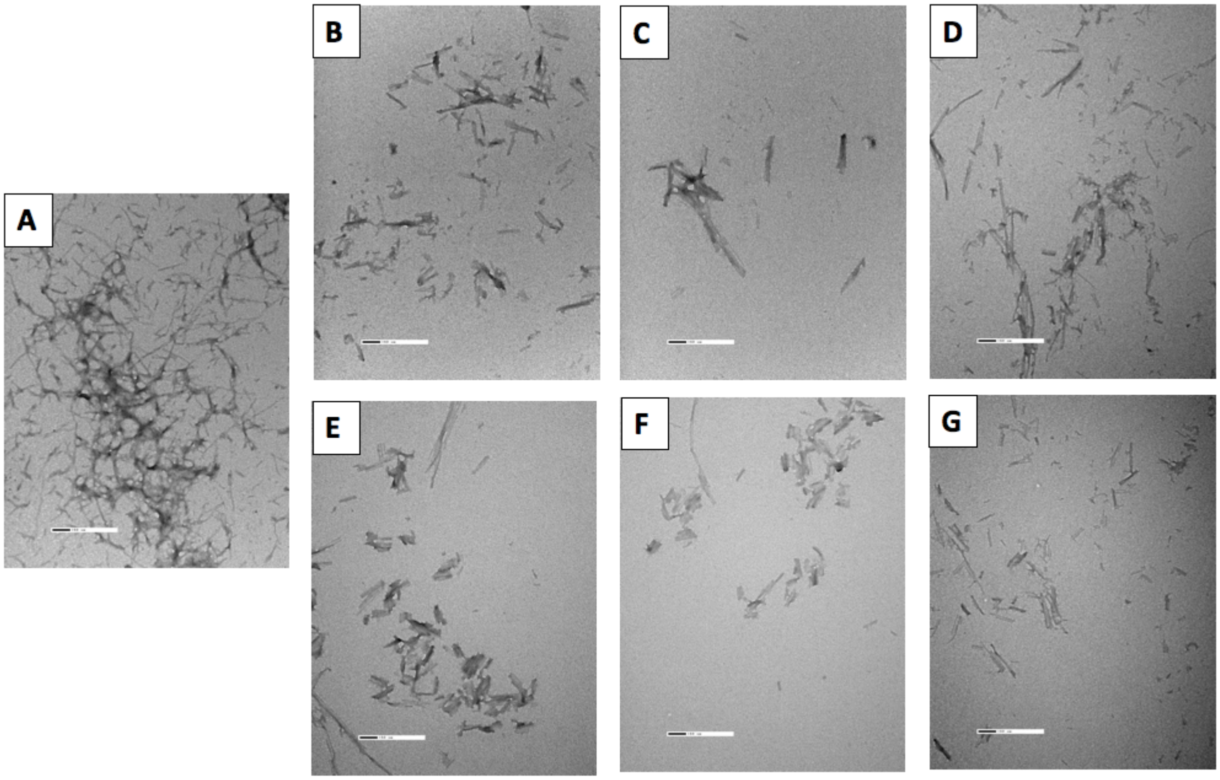

Figure 4.6. TEM images of Aβ_{1-42} alone (5 μM) after 24 h incubation at 37 °C (Panel A), Aβ_{1-42} + **5i** (25 μM, Panel B), Aβ_{1-42} + **5b** (25 μM, Panel C), Aβ_{1-42} + **5c** (25 μM, Panel D), Aβ_{1-42} + **9a** (25 μM, Panel E), Aβ_{1-42} + **9f** (25 μM, Panel F), and Aβ_{1-42} + **9g** (25 μM, Panel G). Scale - 100 nm.

4.2. Molecular modeling studies

Molecular modeling, or docking, studies using computational software is often utilized to design novel molecules and to understand the interactions of test compounds with their molecular target to correlate their chemical structures with the observed biological activity and for further SAR optimization and validation. In this regard, the molecular docking studies of ethynylbiphenyl derivatives with superior inhibition profiles of Aβ_{1-40} and Aβ_{1-42} was investigated using the NMR structures of dimer and oligomer models of Aβ_{1-40} and Aβ_{1-42} respectively to gain insight into their ability to prevent or reduced Aβ aggregation.

4.2.1. Molecular docking of ethynylbiphenyl derivatives with Aβ_{1-40}

Molecular docking studies of lead derivatives **5e** (4'-ethynyl-4-biphenyl-4-ol) and **5i (**4-(4-ethynylphenyl)pyridine), which exhibited excellent inhibition of Aβ_{1-40} aggregation (66 and 79% inhibition at 25 μM, respectively), was investigated by building dimer and oligomer models of Aβ_{1-40}. The docking algorithm CDOCKER in the software program *Discovery Studio Structure-Based-Design* (BIOVIA, Inc) was used. As mentioned in previous sections, Aβ_{1-40} exists as different species, including the monomeric, dimeric, trimeric, tetrameric, oligomeric and fibril forms. In solution, the Aβ_{1-40} protein exists in equilibrium with these species and, as such, molecular docking studies were conducted with these lead derivatives (**5e**, **5i**) using dimer and tetramer models of Aβ_{1-40}. The solid-state NMR structure of Aβ_{1-40} was used to model the dimer and tetramer-β-sheet assembly, and both these models adopt a U-shaped conformation.[179]

The molecular docking of derivative **5e**, which was observed to be an excellent inhibitor of Aβ_{1-40} fibrillogenesis (66% inhibition at 25 μM), within the Aβ_{1-40} dimer model shows that it was oriented in a perpendicular fashion to the Aβ_{1-40} dimer axis and underwent H-bonding and hydrophobic interactions with amino acids in the N- and C-terminal region (Figure 4.7A). Most notably, the 4-hydroxy substituent of **5e** acts as a hydrogen donor and was contact with the backbone C=O of Lys16, (distance = 5.32 Å). This Lys16 is near the N-terminus, within the site of aggregation, or the KLVFFA region which is known to be the seeding point for Aβ aggregation. Effective binding within this region stabilizes the dimer assembly, thus preventing further aggregation. In addition, the ethynyl moiety was in contact with the C=O of Leu34 near the C-terminal region via H-bonding interaction (distance = 2.37 Å). In addition, **5e** underwent a number of nonpolar contacts with amino acids near the C-terminal and N-terminal regions. Prominent interactions include alkyl interactions with alkyl chain of Val36 (distance < 5 Å) and alkyl-π interactions with aromatic ring of derivative **5e** and alkyl chain of Leu17 (distance = 5.0 Å). This analysis suggests that a combination of H-bonding and hydrophobic interactions stabilize the dimer structure and contribute to its superior anti-aggregation activity.

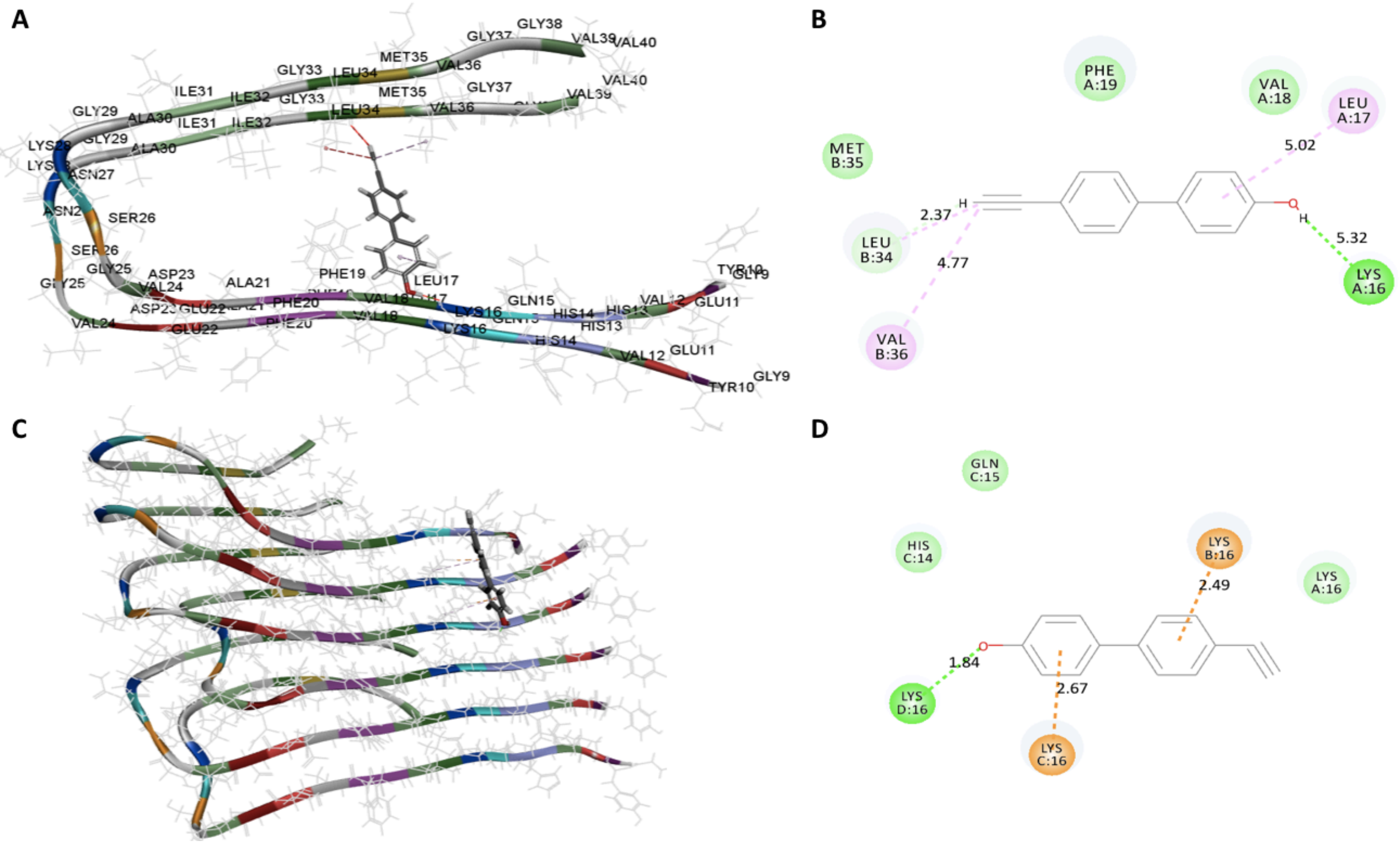

Figure 4.7. The binding mode of derivative **5e** (stick cartoon, Panel A and C) in the dimer and oligomer models of A$\beta_{1\text{-}40}$ (PDB id: 2LMN). Hydrogen atoms in the A$\beta_{1\text{-}40}$ model are removed for clarity. Panel B and D show the 2D interaction map of derivative **5e**, with key amino acids in the A$\beta_{1\text{-}40}$ dimer and oligomer models.

The molecular docking of **5e** with the A$\beta_{1\text{-}40}$ tetramer assembly show that it was oriented in a region consisting of amino acids His14, Gln15 andLys16 (Figure 4.7C). The aromatic rings of **5e** were in contact with side chains of Lys16, undergoing H-bonding, mostly due to electrostatic interactions (distance = 2.49 Å and 2.67 Å), whereas the 4-hydroxy substituent was in contact with another Lys16, via conventional H-bonding (distance = 1.84 Å). The aromatic rings of **5e** were also in contact with side chains of Lys16, via alkyl-π interactions (distance < 5 Å). These investigations suggest that derivative **5e** can stabilize the oligomer assembly and prevent further aggregation into higher order structures.

The derivative **5i** was observed to be the best inhibitor of Aβ_{1-40} fibrillogenesis (79% inhibition at 25 μM). Similar to derivative **5e**, the molecular docking of derivative **5i** within the Aβ_{1-40} dimer model shows that it was oriented closer to the N- and near the C-terminal region (Figure 4.8A). In contrast to the binding interactions observed for compound **5e**, compound **5i** was observed to undergo a greater number of H-bonding and hydrophobic interactions with the Aβ_{1-40} dimer. The 4-ethynyl substituent underwent nonpolar contacts with side chains of Leu34, Val36, (distance < 5 Å), located near the C-terminal region; as well as hydrophobic interactions with the pyridine ring and the side chains of Leu17 and Val18 within the KLVFFA region (distance = 5 Å). In addition to these nonpolar interactions, conventional H-bonding interactions was observed between the pyridine nitrogen atom and the side chain of Val18, within the KLVFFA region (distance = 2.50 Å). The 4-ethynyl substituent was also observed to interact with the backbone C=O of Leu34, Lys16 and Val18; via H-bonding interactions (distance = 2.44 Å, 2.65 Å, and 2.46 Å, respectively).

In the Aβ_{1-40} tetramer assembly, the best binding mode of derivative **5i**, was comparable to the orientation of **5e** and was positioned in a region consisting of amino acids His14, Gln15 and Lys16 (Figure 4.8C). Similar to the binding interactions observed for derivative **5e**, the phenyl and pyridine rings of **5i** were in contact with side chains of Lys16, undergoing π-donor H-bonding interactions (distance = 2.77 Å and 2.14 Å), whereas the nitrogen atom of the pyridine ring was in contact with another Lys16, via conventional H-bonding (distance = 1.99 Å). In addition, the aromatic rings of **5i** were also in contact with side chains of Lys16, via alkyl-π interactions (distance < 5 Å). The number of H-bonding and hydrophobic interactions of **5i**, within both dimer and oligomer A$\beta_{1\text{-}40}$ assemblies, stabilize the A$\beta_{1\text{-}40}$ structure and contribute to its superior anti-aggregation activity, compared to **5e**. These investigations suggest that derivative **5i** can stabilize the A$\beta_{1\text{-}40}$ dimer and oligomer assemblies and prevent their further aggregation into higher order structures.

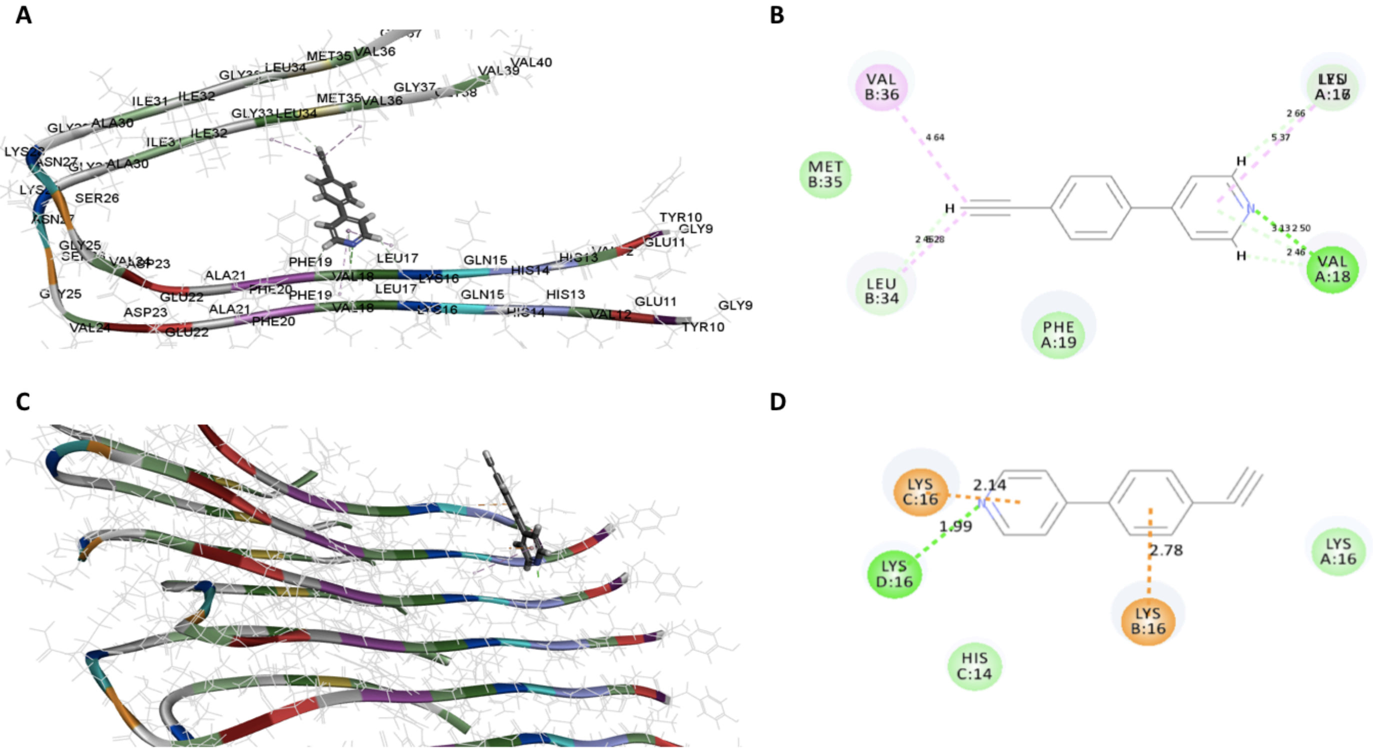

Figure 4.8. The binding mode of derivative **5i** (stick cartoon, Panel A and C) in the dimer and oligomer models of A$\beta_{1\text{-}40}$ (PDB id: 2LMN). Hydrogen atoms in the A$\beta_{1\text{-}40}$ model are removed for clarity. Panel B and D show the 2D interaction map of derivative **5i**, with key amino acids in the A$\beta_{1\text{-}40}$ dimer and oligomer models.

4.2.2. Comparison of molecular docking studies of ethynylbiphenyls with corresponding halogen and cyano bioisosteres in $A\beta_{1-40}$ models

The binding mode of $A\beta_{1-40}$ aggregation inhibitors **5a**, 4-bromobiphenyl and 4-cyanobiphenyl was also investigated in the $A\beta_{1-40}$ dimer model, in order to investigate the different binding interactions exhibited by these compounds with varying bioisosteric features (Figure 4.9). As mentioned in previous sections, the incorporation of a terminal unsubstituted ethynyl group on aromatic carbons acts as an electrophilic surrogate for halomethyls.[159] In addition, the comparison of the nitrile group, which has similar polarity properties to the halogen and ethynyl moiety, but differs in the presence of an electronegative nitrogen results in an increase in the polarity of the nitrile containing compound, with a decreased cLogP value, as displayed in Figure 4.9. In this case, the use of an ethynyl moiety as a halogen bioisostere exhibited similar anti-$A\beta_{1-40}$ aggregation activity; wherein compound **5a**, 4-ethynyl-1,1'-biphenyl, was observed to have a maximum inhibition of 62% inhibition at 25 μM; and 4-bromobiphenyl was observed to have a comparable a maximum inhibition of 64% inhibition at 25 μM. The 4-cyanobiphenyl compound, however, was observed to be less potent toward $A\beta_{1-40}$ fibrillogenesis, with a maximum inhibition of 51% at 25 μM.

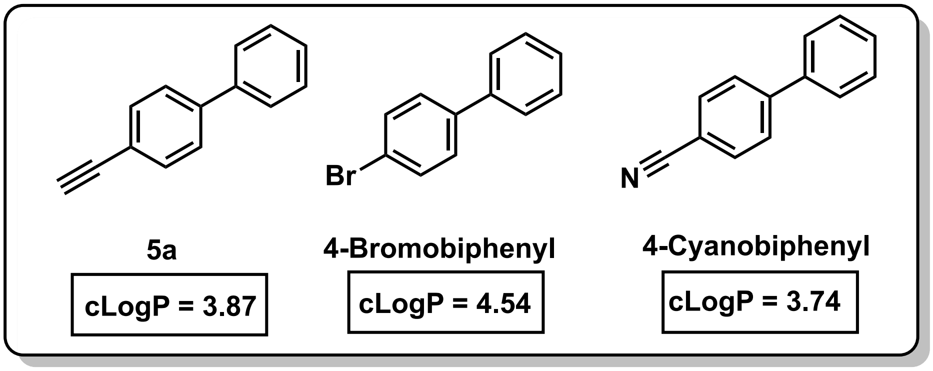

Figure 4.9. Chemical structures and cLogP values for compound **5a**, 4-bromobiphenyl and 4-cyanobiphenyl compounds.

The molecular docking of derivative **5a** within the Aβ_{1-40} dimer model shows that it was interacting with the N-terminal region of the Aβ_{1-40} dimer assembly; with H-bonding and hydrophobic interactions occurring within the KLVFFA region (Figure 4.10A). Interestingly, the aromatic ring of **5a** underwent hydrophobic interactions with the aromatic side chains of Phe19 (distance = 4.20 Å) and the alkyl side chain of Val18 (distance = 5.13 Å).

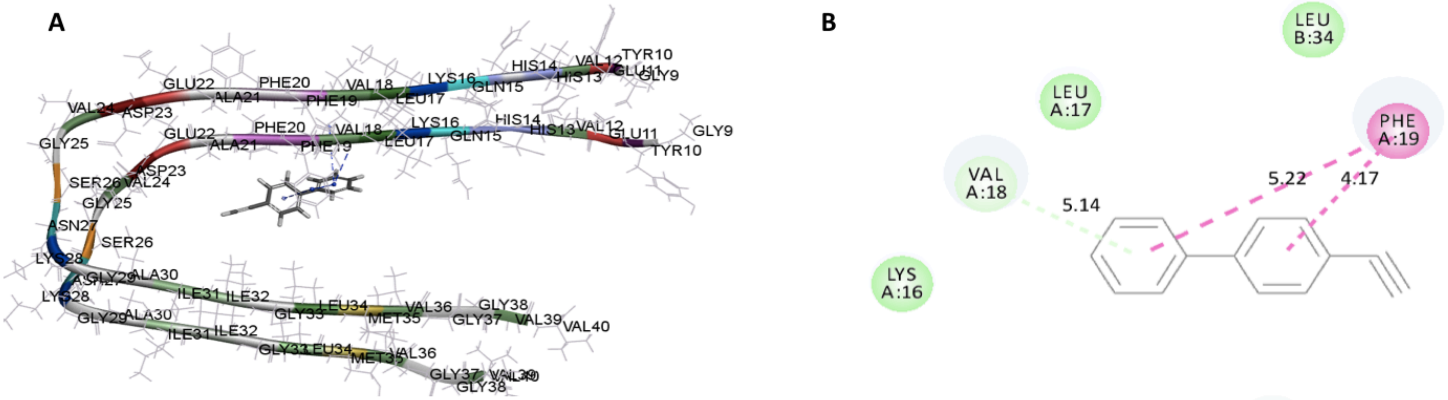

Figure 4.10. The binding mode of derivative **5a** (stick cartoon, Panel A) in the dimer model of Aβ_{1-40} (PDB id: 2LMN). Hydrogen atoms in the Aβ_{1-40} model are removed for clarity. Panel B shows the 2D interaction map of derivative **5a**, with key amino acids in the Aβ_{1-40} dimer model.

Similar to derivative **5a**, the molecular docking of 4-cyanobiphenyl within the Aβ_{1-40} dimer model shows that it was oriented near the KLVFFA region (Figure 4.11A). In contrast to the binding interactions observed for derivative **5a**, 4-cyanobiphenyl was not observed to undergo any H-bonding interactions with the Aβ_{1-40} dimer. Instead, the aromatic rings were observed to interact with the aromatic side chains of Phe19 (distance = 4.28 Å and 5.53 Å) and the alkyl side chain of Val18 (distance = 5.07 Å) via hydrophobic π- π and π-alkyl interactions. The lack of H-bonding interactions seen with the 4-cyanobiphenyl and the Aβ_{1-40} dimer model may not be adequate to stabilize the dimer as effectively as derivative **5a**, thus reflecting its weaker Aβ_{1-40} inhibitory activity. In a similar fashion, 4-bromobiphenyl was also positioned near the KLVFFA region of the A$\beta_{1\text{-}40}$ dimer model (Figure 4.11C). Analogous to the binding mode of 4-cyanobiphenyl, 4-bromobiphenyl did not undergo H-bonding interactions and the aromatic rings on the compound were observed to interact with the aromatic side chains of Phe19 and Phe20 (distance = 4.44 Å and 5.33 Å) via hydrophobic π-π interactions. The hydrophobic π-π interactions between one aromatic ring within 4-bromobiphenyl and two different aromatic sidechains (Phe19 and Phe20) may create a more stable complex between the compound and the A$\beta_{1\text{-}40}$ dimer model, in comparison to 4-cyanobiphenyl. This stabilizing of the A$\beta_{1\text{-}40}$ dimer model is reflected in the increased anti-A$\beta_{1\text{-}40}$ aggregation activity of 4-bromobiphenyl.

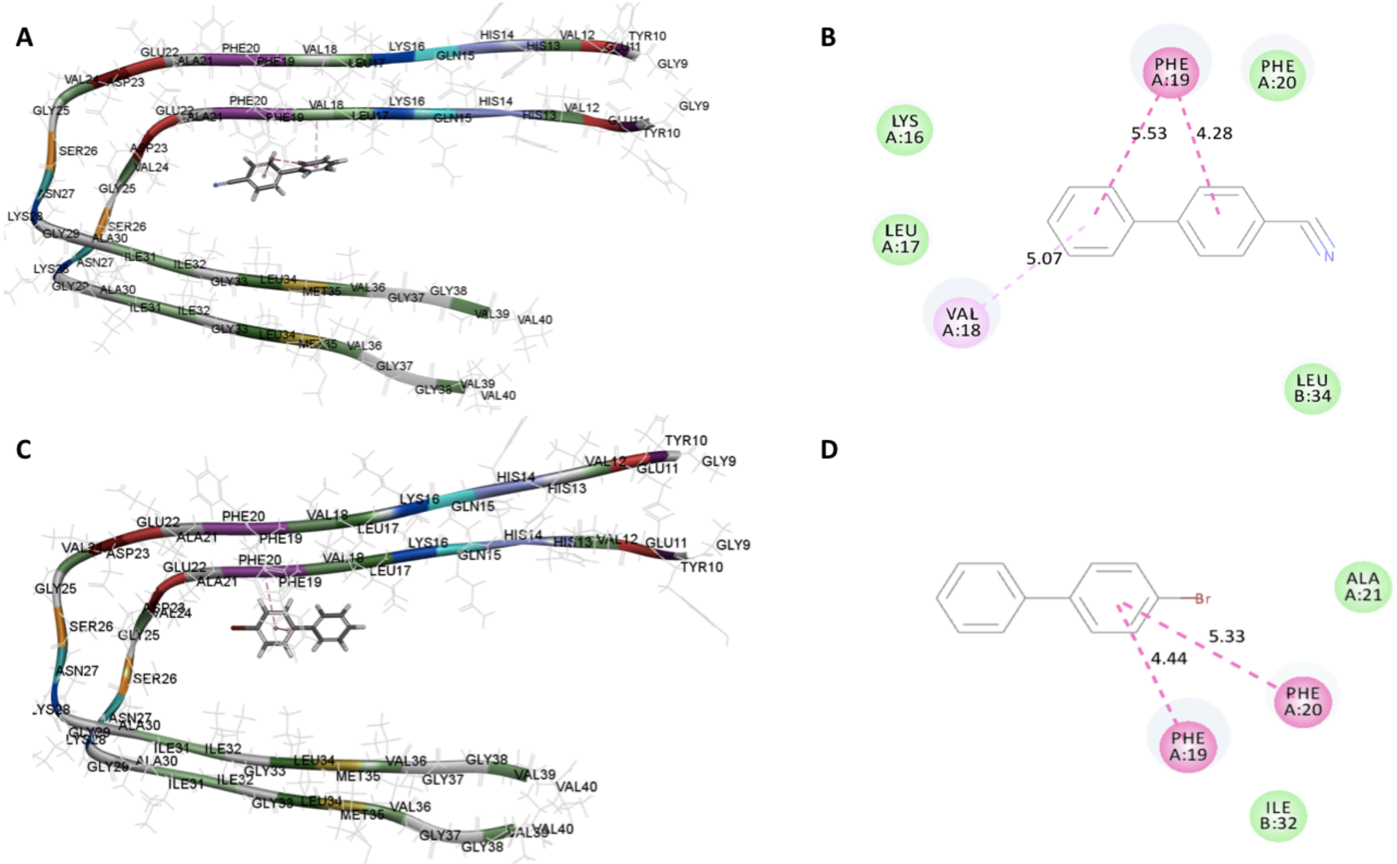

Figure 4.11. The binding mode of 4-cyanobiphenyl (stick cartoon, Panel A) and 4-bromobiphenyl (stick cartoon, Panel C) in the dimer model of A$\beta_{1\text{-}40}$ (PDB id: 2LMNs). Hydrogen atoms in the

A$\beta_{1\text{-}40}$ model are removed for clarity. Panel B and D show the 2D interaction map of 4-cyanobiphenyl and 4-bromobiphenyl compounds with key amino acids in the A$\beta_{1\text{-}40}$ dimer model.

The CDOCKER algorithm used produces the top binding modes of these compounds bound using CHARMm force field. These binding modes were ranked based on the CDOCKER energies and CDOCKER interaction energies in kcal/mol, indicating the relative stability of these binding modes.[181,183] In this case, the CDOCKER energies for the ethynylbiphenyls with corresponding halogen and cyano bioisosteres in A$\beta_{1\text{-}40}$ models are given below:

	CDOCKER Energy (kcal/mol)
4-Ethynyl-1,1'-biphenyl (5a)	–2.08
4-Cyanobiphenyl	–1.05
4-Bromobiphenyl	–3.01

In this case, 4-bromobiphenyl was observed to have the highest negative CDOCKER energy (–3.01 kcal/mol), in comparison to the cyano and ethynyl substituted derivatives, indicating a more stable complex. This high negative CDOCKER energy further validates the stabile binding mode of 4-bromobiphenyl within the A$\beta_{1\text{-}40}$ dimer model, which is also reflected in the increased anti-A$\beta_{1\text{-}40}$ aggregation activity of 4-bromobiphenyl. This is followed by derivative **5a** (–2.08 kcal/mol), and 4-cyanobiphenyl (–1.05 kcal/mol), which was observed to form the least stable binding mode, thus, reflecting its weaker A$\beta_{1\text{-}40}$ inhibitory activity.

4.2.3. Molecular docking of ethynylbiphenyl derivatives with A$\beta_{1\text{-}42}$

Molecular docking studies of lead derivatives **9g** (3'-ethynylbiphenyl-4-yl)(methyl)sulfane) and **5i** (4-(4-ethynylphenyl)pyridine), which exhibited excellent inhibition of A$\beta_{1\text{-}42}$ aggregation (86% inhibition at 25 μM), was investigated by building dimer and oligomer models of A$\beta_{1\text{-}42}$. The docking algorithm CDOCKER in the software program *Discovery Studio*

Structure-Based Design (BIOVIA, Inc) was used. Molecular docking studies were conducted with these lead derivatives (**9g**, **5i**) using dimer and tetramer models of Aβ_{1-42}. The NMR structure of Aβ_{1-42} was used to model the dimer and tetramer-β-sheet assembly, and both these models adopt an S-shaped conformation, unlike the U-shape observed for Aβ_{1-40} models.[180,181]

The molecular docking of derivative **9g**, which was observed to be an excellent inhibitor of Aβ_{1-42} fibrillogenesis (86% inhibition at 25 μM), within the Aβ_{1-42} dimer model shows that it was interacting with N-terminal amino acids Val12, Val18, Ala21, Gln15 and Lys16 (distance < 5.0 Å) as shown in Figure 4.12A, via hydrophobic interactions. Interestingly, the 3-ethynylsubstituent underwent H-bonding interactions with the C=O backbone of Glu11 (distance = 3.0 Å), while the aromatic ring underwent hydrophobic interactions with Ala21 whereas the 4-thiomethyl-benzene ring was in contact with Lys16 via cation-π interactions, wherein Lys16 acts as the cation (distance < 5.0 Å).These interactions show that **9g** is able to effectively stabilize Aβ_{1-42} dimer model, and as a resulting in excellent Aβ_{1-42} inhibitory activity.

The molecular docking of **9g** with the Aβ_{1-42} tetramer assembly shows that it was oriented within the N-terminal region of the assembly (Figure 4.12C). Similar to the binding interactions observed in the Aβ_{1-42} dimer assembly, the binding mode, of **9g** was interacting with the side chains of Val18 and Ala21 via various hydrophobic π-alkyl and alkyl interactions (distance < 5.0 Å). In the Aβ_{1-42} tetramer model, however, the 3-ethynyl hydrogen interacts with C=O backbone of Glu22 via H-bonding interaction (distance = 2.94 Å). These studies suggest the ability of derivative **9g** to bind to the Aβ_{1-42} oligomer assemblies and prevent their further aggregation.

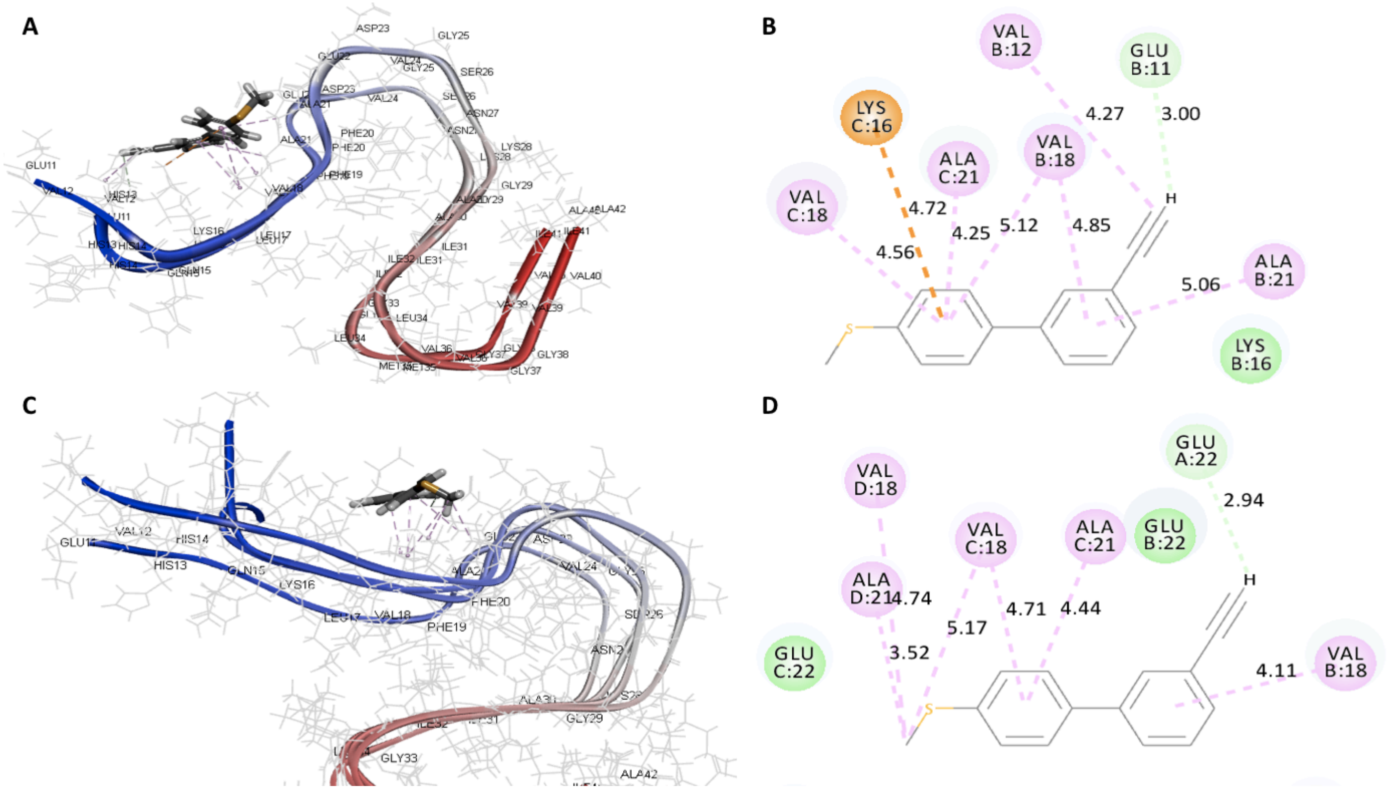

Figure 4.12. The binding mode of derivative **9g** (stick cartoon, Panel A and C) in the dimer and oligomer models of A$\beta_{1\text{-}42}$ (PDB id: 5KK3). Hydrogen atoms in the A$\beta_{1\text{-}42}$ model are removed for clarity. Panel B and D show the 2D interaction map of derivative **9g**, with key amino acids in the A$\beta_{1\text{-}42}$ dimer and oligomer models.

In comparison, the molecular docking of derivative **5i**, within the Aβ_{1-42} dimer model shows that it was also interacting with N-terminal amino acids Val18 and Ala21, via hydrophobic π-alkyl interactions (distance < 5.0 Å) as shown in Figure 4.13A which was similar to the interactions observed for **9g** in the Aβ_{1-42} dimer model. In contrast to the binding mode of derivative **9g**, the 4-ethynyl substituent of **5i** did not participate in any interactions. Instead, the pyridine nitrogen atom underwent H-bonding interactions with the side chain of Lys16 (distance = 2.0 Å). This H-bonding interaction between nitrogen atom and amino acid Lys16, located within the KLVFFA region, as well as the various hydrophobic interactions, suggest that derivative **5i** effectively stabilizes the Aβ_{1-42} dimer model, thus contributing to its anti-Aβ_{1-42} fibrillogenesis activity.

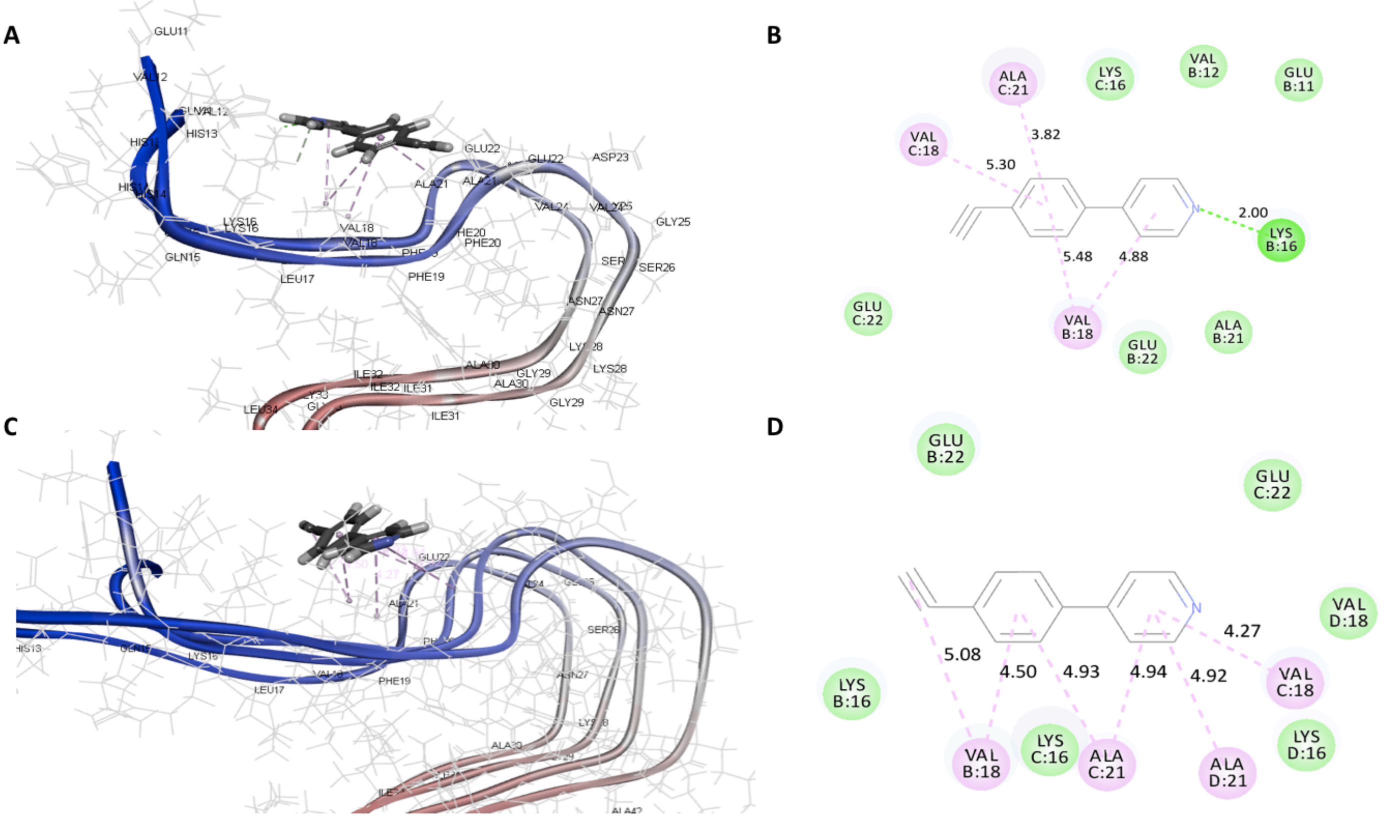

Figure 4.13. The binding mode of derivative **5i** (stick cartoon, Panel A and C) in the dimer and oligomer models of Aβ_{1-42} (PDB id: 5KK3). Hydrogen atoms in the Aβ_{1-42} model are removed for

clarity. Panel B and D show the 2D interaction map of derivative **5i**, with key amino acids in the Aβ_{1-42} dimer and oligomer models.

In contrast, the molecular docking of **5i** in the Aβ_{1-42} tetramer assembly shows that it undergoes hydrophobic interactions within the N-terminal region of the assembly (Figure 4.13C). Similar to the binding interactions observed in the Aβ_{1-42} dimer assembly, derivative **5i** interacts with the side chains of Val18 and Ala21 via various hydrophobic π-alkyl and alkyl interactions (distance < 5.0 Å). These studies suggest the ability of **5i** to interact with N-terminal region and prevent Aβ_{1-42} fibrillogenesis.

4.2.4. Comparison of molecular docking studies of ethynylbiphenyls with corresponding halogen and cyano bioisosteres in Aβ_{1-42} models

The binding modes of the 4-ethynylbiphenyl compound **5a** was compared with corresponding 4-bromobiphenyl and 4-cyanobiphenyls that carry either bromo or cyano bioiososteres in the Aβ_{1-42} dimer model (Figure 4.9). ThT-based aggregation kinetic assays conducted with Aβ_{1-42} and these compounds exhibited anti-Aβ_{1-42} aggregation activity; wherein compound **5a**, 4-ethynyl-1,1'-biphenyl, was observed to have a maximum inhibition of 83% inhibition at 25 μM; and 4-bromobiphenyl was observed to be more potent toward Aβ_{1-42} with a maximum inhibition of 88% inhibition at 25 μM whereas the 4-cyanobiphenyl compound was observed to be have comparable potency towards Aβ_{1-42} fibrillogenesis, with a maximum inhibition of 85% at 25 μM.

The molecular docking of derivative **5a** within the Aβ_{1-42} dimer model shows that it was undergoing a number of interactions within with the N-terminal region of the Aβ_{1-42} dimer assembly with both H-bonding and hydrophobic interactions occurring within the N-terminus (Figure 4.14A). Similar to the binding mode observed in Aβ_{1-40} dimer model, the aromatic ring of

5a undergoes a cation-π interaction with the Lys16 side chain (distance = 2.87 Å), while also undergoing hydrophobic interactions with the alkyl side chains of Val18 and Ala21 (distance = 4.66 – 5.13 Å).

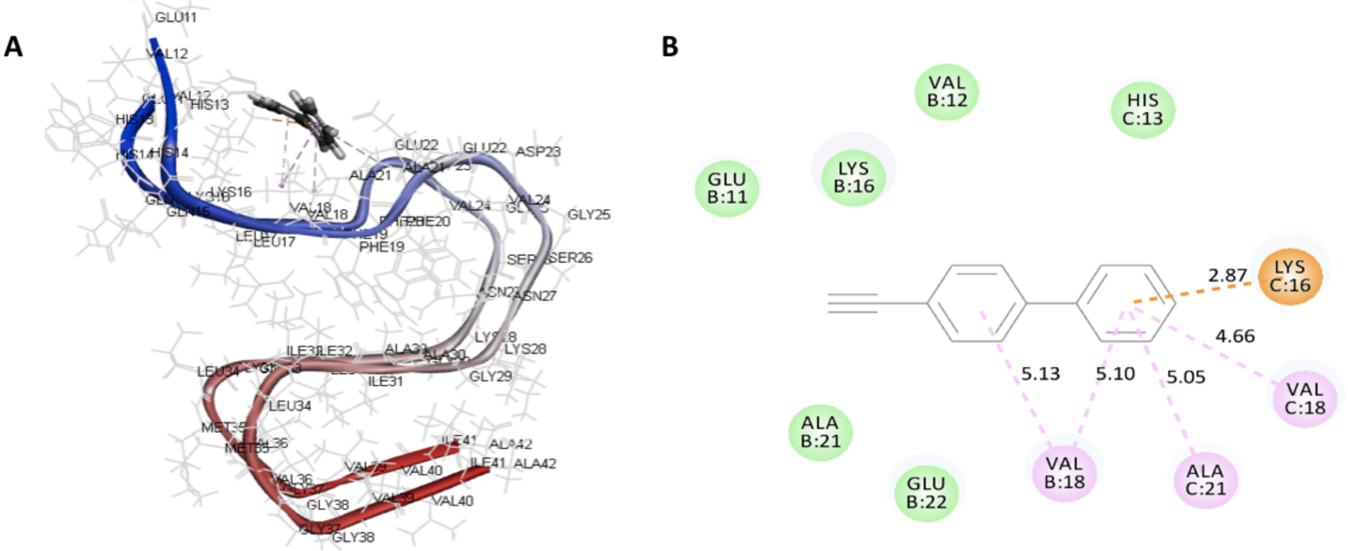

Figure 4.14. The binding mode of derivative **5a** (stick cartoon, Panel A) in the dimer model of A$\beta_{1\text{-}42}$ (PDB id: 5KK3). Hydrogen atoms in the A$\beta_{1\text{-}42}$ model are removed for clarity. Panel B shows the 2D interaction map of derivative **5a**, with key amino acids in the A$\beta_{1\text{-}42}$ dimer model.

In comparison, the molecular docking of derivative 4-cyanobiphenyl within the A$\beta_{1\text{-}42}$ dimer model shows that it was positioned similarly, within the N-terminus (Figure 4.14A). However, in contrast to the observed binding mode of derivative **5a**, 4-cyanobiphenyl exhibited H-bonding, as well as electrostatic interactions within the KLVFFA region of the A$\beta_{1\text{-}42}$ dimer. Similar to the binding mode of **5a** observed in A$\beta_{1\text{-}42}$ dimer model, the unsubstituted aromatic ring of 4-cyanobiphenyl undergoes a cation-π interaction with the Lys16 side chain (distance = 2.23 Å) and interestingly even the 4-cyano-substituted aromatic ring underwent similar cation-π interactions with another Lys16 side chain (distance = 4.39 Å). In addition, the aromatic ring of 4-cyanobiphenyl was observed to interact with the alkyl side chain of Val18, via hydrophobic interactions (distance = 4.93 Å). This suggests that the increased inhibition of Aβ_{1-42} aggregation demonstrated by the 4-cyanobiphenyl compound could be due to the presence of an additional cation-π interaction compared to **5a** which can provide additional stabilization of the dimer assembly.

Comparably, 4-bromobiphenyl was also positioned near the KLVFFA region of the Aβ_{1-42} dimer model (Figure 4.14C). Analogous to the binding mode of 4-cyanobiphenyl, both the aromatic rings of 4-bromobiphenyl compound were also observed to undergo couple of cation-π-interactions with Lys16 side chains (distance = 2.19 – 4.30 Å, Figure 4.14C), In contrast to 4-cyanobiphenyl, 4-bromobiphenyl was observed to undergo additional hydrophobic interactions with the side chains of Val12, Lys 16 and Val18 (distance = 5.03 - 5.49 Å), and the 4-bromo-substituent was exhibited hydrophobic alkyl interactions with the side chains of Ala21(distance = 4.06 Å). These additional interactions help to further stabilize the Aβ_{1-42} dimer model, thus reflecting the increased anti-Aβ_{1-42} aggregation activity observed for 4-bromobiphenyl.

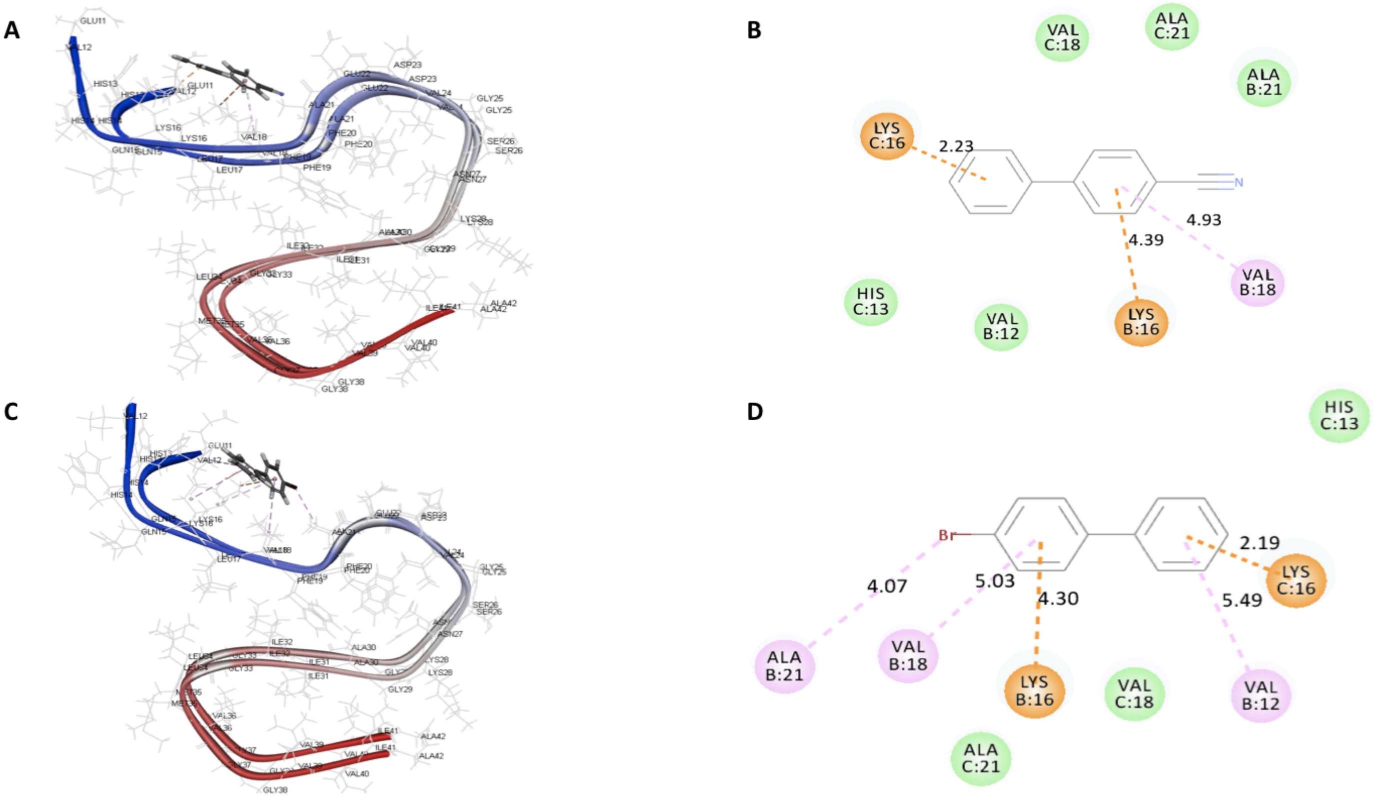

Figure 4.15. The binding mode of 4-cyanobiphenyl (stick cartoon, Panel A) and 4-bromobiphenyl (stick cartoon, Panel C) in the dimer model of Aβ$_{1-42}$ (PDB id: 5KK3). Hydrogen atoms in the Aβ$_{1-42}$ model are removed for clarity. Panel B and D show the 2D interaction map of 4-cyanobiphenyl and 4-bromobiphenyl compounds with key amino acids in the Aβ$_{1-42}$ dimer model.

Similar to the Aβ_{1-40} docking studies, the CDOCKER algorithm produced the top binding modes of these compounds and ranked them based on the CDOCKER energies in kcal/mol, indicating the relative stability of these binding modes.[181,183] Here, the CDOCKER energies for the ethynylbiphenyls with corresponding halogen and cyano bioisosteres in Aβ_{1-42} models are given below:

	CDOCKER Energy (kcal/mol)
4-Ethynyl-1,1'-biphenyl (5a)	–8.26
4-Cyanobiphenyl	–3.92
4-Bromobiphenyl	–6.44

In contrast to what was observed when comparing negative CDOCKER energies for Aβ_{1-40} binding modes, the values observed with Aβ_{1-42} docking were much larger, further reflecting the increased anti-Aβ_{1-42} aggregation activity of these derivatives. In this case, however, derivative **5a** (–8.26 kcal/mol) was observed to have the highest negative CDOCKER energy, in comparison to the cyano and bromo substituted derivatives, indicating a more stable complex. This is followed by 4-bromobiphenyl (–6.44 kcal/mol) and 4-cyanobiphenyl (–3.92 kcal/mol), which was observed to form the least stable binding mode. However, because all these compounds display a relatively high negative CDOCKER energy value, the result is the formation of a very stable binding mode, which validates the observed potent anti-Aβ_{1-42} aggregation activity of these derivatives.

These molecular docking studies provide insight on the binding interactions of ethynylbiphenyl derivatives in the Aβ_{1-40} and Aβ_{1-42} dimer and oligomer models. Furthermore, these studies also suggest that ethynyl-substituent can be considered as a bioisotere of either halogens or the cyano group in developing novel biphenyl derivatives that possess anti-Aβ aggregation properties.

Chapter 5: Conclusion and Future Outlook

The goal of this research project was to design and evaluate a novel biphenyl ring template with an ethynyl-substituent capable of targeting the self-assembly of A$\beta_{1-40/42}$ peptides. Through a combination of computational chemistry, compound library synthesis and biochemical studies, SAR data was acquired for a novel class of 17 ethynyl-1,1'-biphenyl derivatives **5a**-**j**, **9a**-**g** and **14**.

The ethynylbiphenyl derivatives were designed and synthesized via palladium catalyzed C-C bond formation using Suzuki cross-coupling to obtain the biphenyl template and the incorporation of the ethynyl substituent via geminal dibromoalkene synthesis by bromination and their conversion to terminal acetylenes to afford ethynyl-1,1'-biphenyl derivatives. The synthetic routes implemented were successful and provided final yields ranging from 28–95%. The chemical library of ethynyl-1,1'-biphenyl derivatives were screened biologically to determine their potential Aβ anti-aggregation activity and to obtain SAR data for this library. In order to determine the biological profile for these derivatives, ThT-based fluorescence aggregation kinetics assay was utilized to test derivatives with Aβ_{1-40} and Aβ_{1-42} peptides and the SAR data was obtained. TEM studies were carried out to determine the changes in Aβ aggregation morphology in the presence of ethynylbiphenyl derivatives. Molecular docking studies were performed to investigate the interactions of lead ethynylbiphenyl derivatives in the dimer and oligomer models of Aβ_{1-40} and Aβ_{1-42}, in order to enhance our understanding on binding mechanisms and to further validate the SAR data.

A collective summary of the various parameters for the ethynyl-1,1'-biphenyl library **5a**-**j**, **9a**-**g** and **14** is displayed below:

Molecular Weights (MW):	178.23 – 256.32 g/mol
Partition Coefficients (cLogP):	2.53 – 4.31
Molecular Volume:	143.03 – 200.65 Å^3
$A\beta_{1-40}$ Aggregation Inhibition:	26 – 79%
$A\beta_{1-42}$ Aggregation Inhibition:	56 – 86%

Our results indicate that the ethynyl-1,1'-biphenyl derivatives **5a**-**j**, **9a-g** and **14** exhibit anti-Aβ aggregation properties. Known Aβ inhibitors, honokiol and magnolol, as well as halogenated biphenyl compounds, 4-bromobiphenyl, 4-bromo-4'-methoxybiphenyl, 4-chlorobiphenyl, 4-iodobiphenyl, and 4-fluorobiphenyl, were also evaluated to assess and compare their anti- Aβ activity with the synthesized ethynylbiphenyl derivatives. It was observed that the synthesized ethynyl-1,1'-biphenyl derivatives **5a**-**j**, **9a**-**g** and **14**, as well as the various halogenated and cyano biphenyl compounds exhibit superior inhibition of $A\beta_{1-42}$ aggregation over $A\beta_{1-40}$ inhibition. These investigations clearly demonstrate the ability of the ethynyl-1,1'-biphenyl derivatives to prevent Aβ-fibrillogenesis by direct interactions (~26–86% inhibition).

Among the derivatives tested, derivatives **5e** (4'-ethynyl-4-biphenylol) and **5i** **(**4-(4-ethynylphenyl)pyridine), were identified as excellent inhibitors of $A\beta_{1-40}$ aggregation (66 and 79% inhibition at 25 μM, respectively) whereas compound **9g** (3'-ethynylbiphenyl-4-yl)(methyl)sulfane) and **5i** **(**4-(4-ethynylphenyl)pyridine) were identified as lead derivatives of $A\beta_{1-42}$ aggregation, with exhibited excellent inhibition (~86% inhibition at 25 μM).

Furthermore, in comparison to the unsubstituted 4-ethynyl-1,1'-biphenyl derivative (**5a**, 62% inhibition of $A\beta_{1-40}$, 83% inhibition of $A\beta_{1-42}$) and the unsubstituted 3-ethynyl-1,1'-biphenyl derivative (**9a**, 55% inhibition of $A\beta_{1-40}$, 86% inhibition of $A\beta_{1-42}$), the naturally occurring biphenyls; honokiol and magnolol were observed to be better inhibitors of $A\beta_{1-40}$ and $A\beta_{1-42}$ fibrillogenesis at 25 μM (61 – 89% inhibition range).

The halogenated biphenyl compounds exhibited inhibition comparable to derivatives **5a** and **9a** toward both $A\beta_{1-40}$ and $A\beta_{1-42}$ fibrillogenesis (52–64% inhibition of $A\beta_{1-40}$, 55–89% inhibition of $A\beta_{1-42}$). The addition of the ethynyl moiety either at 4- or 3-position, appears to increase the anti-Aβ fibrillogenesis activity when compared to inhibition rates observed by the unsubstituted biphenyl compound (53% inhibition of $A\beta_{1-40}$, 61% inhibition of $A\beta_{1-42}$). Similarly, the 4-cyanobiphenyl activity toward $A\beta_{1-40}$ fibrillogenesis (51% inhibition of $A\beta_{1-40}$) was observed to be less effective than derivatives **5a** and **9a**. However, the inhibition profile of 4-cyanobiphenyl toward $A\beta_{1-42}$ fibrillogenesis was observed to be similar to derivatives **5a** and **9a** (85% inhibition of $A\beta_{1-40}$).

TEM studies were used to validate and confirm the results observed in the ThT-based fluorescence assay, as well as assess the morphology of $A\beta_{1-40}$ and $A\beta_{1-42}$ aggregates after incubating the target ethynyl-1,1'-biphenyl derivatives. There was significant reduction in the formation of Aβ aggregates and Aβ load observed upon co-incubation with the derivatives, providing further evidence on the anti-aggregation properties of these compounds.

Molecular docking studies of lead derivatives **5e** (4'-ethynyl-4-biphenyl-4-ol) and **5i** (4-(4-ethynylphenyl)pyridine), which exhibited excellent inhibition of $A\beta_{1-40}$ aggregation was investigated in the dimer and oligomer models of $A\beta_{1-40}$. This analysis suggests that both **5e** and **5i** were able to interact with both the N- and C-terminal amino acids by orienting in a perpendicular fashion along the dimer axis and underwent H-bonding and hydrophobic interactions to stabilize the dimer structure which contributed to anti-aggregation activity. In contrast, the binding modes of **5a** and bioisosteric compounds 4-bromobiphenyl and 4-cyanobiphenyl in the A$\beta_{1\text{-}40}$ dimer model shows that they were oriented closer to the N-terminal in parallel to the dimer axis with compound **5a** undergoing better interactions compared to 4-cyanobiphenyl compound whereas the 4-bromobiphenyl, was observed to undergo greater interactions in the KLVFFA region, reflecting its increased anti-A$\beta_{1\text{-}40}$ aggregation activity.

The molecular docking studies of lead derivatives **9g** (3'-ethynylbiphenyl-4-yl)(methyl)sulfane) and **5i (**4-(4-ethynylphenyl)pyridine) in the A$\beta_{1\text{-}42}$ dimer and oligomer models show their ability to stabilize A$\beta_{1\text{-}42}$ dimer and oligomer models by interacting in the KLVFFA region of the S-shaped conformation resulting in excellent A$\beta_{1\text{-}42}$ inhibitory activity. The binding mode of A$\beta_{1\text{-}42}$ aggregation inhibitors **5a** and the corresponding compounds with bioisosteric replacement, namely compounds 4-bromobiphenyl and 4-cyanobiphenyl was also investigated in the A$\beta_{1\text{-}42}$ dimer model. These compounds showed the importance of cation-π interactions in stabilizing the conformations and their ability to prevent A$\beta_{1\text{-}42}$ aggregation. These studies also show the suitability of ethynyl-substituent as a bioisostere for either halogen or cyano-substituted biphenyls.

Interestingly, when comparing the molecular volume occupied by each of these bioisosteric replacements, both the ethynyl and cyano substituents are observed to have similar values, whereas the bromo substituent has a much larger molecular volume value, as displayed below:

	Biphenyl	**Ethynyl Substituent**	**Cyano Substituent**	**Bromo Substituent**
Molecular Volume (Å^3)	129.65	14.75	14.06	37.39

The larger molecular volume observed for the bromo substituent may account for the potent Aβ_{1-40} inhibitory activity, wherein a stabilization of the complex is likely due to this larger molecular volume. In contrast, the smaller molecular volumes observed for the ethynyl and cyano substituents might result in less effective Aβ_{1-40} inhibitory activity. Similarly, an opposite trend was observed for the ethynyl and cyano substituents, with respect to Aβ_{1-42} inhibitory activity, where their smaller molecular volumes seems to enhance their binding in the KLVFFA groove and the larger bromo substituted biphenyl derivative was less effective in preventing Aβ_{1-42} aggregation, suggesting the difference in the binding regions of Aβ_{1-40} and Aβ_{1-42} dimer models.

The acquired SAR data supports the hypothesis that the ethynyl-1,1'-biphenyl ring template can be used as a suitable template to develop novel agents that can prevent Aβ aggregation and to design novel anti-AD agents. Moreover, these results confirm the use of an ethynyl moiety as a viable halogen bioisostere and a better alternative to the design of novel molecules since there are reports of toxicity associated with halogenated biphenyls which is a drawback in using halogen containing biphenyl rings in drug design.[182]

Future studies based on the findings of this work involves expanding the ethynyl-1,1'-biphenyl library through structure modifications of lead derivatives in order to improve their biological profile as Aβ inhibitors, as well as examining their toxicity profile and ability to reduce Aβ-mediated cell death in hippocampal HT22 cells. It is anticipated that the results obtained from these experiments will be able to identify lead compounds for evaluation in animal models of AD as well as further SAR optimization.

In summary, this investigation provides valuable first evidence on the development of ethynyl-1,1'-biphenyl derivatives as novel chemical tools to study Aβ aggregation and design agents to treat AD.

Chapter 6: Experimental

6.1. Chemistry

All reagents and chemicals used in the synthesis were purchased from either Sigma-Aldrich (St. Louis, MO, USA), TCI Chemicals (Portland, OR, USA), or Matrix Scientific (Columbia, SC, USA) and was used without further purification. Melting points were determined on a Fisher-Johns apparatus and are uncorrected. ^{1}H NMR spectra were recorded on a Bruker ® Avance 300 MHz series spectrometer using $CDCl_3$ as the solvent. Coupling constants (*J* values) were recorded in hertz (Hz) and the following abbreviations were used for multiplicity of NMR signals: s = singlet, d = doublet, t = triplet, m = multiplet, br = broad. Compound purification was accomplished using Merck 230-400 mesh silica gel 60. All derivatives showed single spot on thin-layer chromatography (TLC) performed on Merck 60 F_{254} silica gel plates (0.2 mm) using three different solvent systems (n-hexane/EtOAc, 1:1, n-hexane/EtOAc, 7:1, n-hexane/EtOAc, 5:1, n-hexane/EtOAc, 5:2, n-hexane/EtOAc, 6:1, n-hexane/EtOAc, 20:1) and spots were visualized with UV 254 nm. Compound purity (> 95%) was measured using an Agilent 6100 series single quad LCMS equipped with an Agilent 1.8 µm Zorbax Eclipse Plus C18 (2.1 x 50 mm) running 90:10 MeOH/IPA at a flow rate of 0.4 mL/min with detection at 254 nm by UV. The biphenyl, 4-chloro, bromo, fluoro, iodo and cyanobipheyl compounds were obtained from Sigma-Aldrich and TCI America and were > 95% pure. High resolution mass spectra (HRMS) were recorded on a Thermo Scientific Q ExactiveTM mass spectrometer with an ESI source, Department of Chemistry, University of Waterloo.

6.1.1. General method to prepare intermediates 3a-h, 7a-g[168]

Under argon atmosphere, $Pd(OAc)_2$ (0.023 g, 0.10 mmol) was combined with Xantphos (0.069 g, 0.10 mmol) in degassed THF (7.5 mL). After stirring for 5 min, this resulting solution was added into a separate round-bottom-flask (RBF) containing bromobenzene (**2a**-**h**, Scheme 3.1) (1.0 g, 4.12 mmol), phenylboronic acid (**1** or **6**, Scheme 3.1 or 3.2) (0.54 g, 4.41 mmol), and K_3PO_4 (2.62 g, 12.35 mmol). The reaction was then stirred with heating at 60 °C for 18 h. The reaction mixture was extracted two times with DCM (100 mL), and distilled water (100 mL). The combined organic extracts were dried over $MgSO_4$ and filtered. The solvent was evaporated under reduced pressure to afford the crude product, which was then purified by column chromatography (silica gel, *n*-hexane/EtOAc (5:1 or 7:1)) to give the desired product, **3a-h** or **7a-h** as white solids Yield: 26 – 91 %.

Physical and spectroscopy data for the synthesized compounds are provided below.

(1,1'-Biphenyl)-4-carbaldehyde (**3a**): The product was obtained as a beige solid after coupling with 4-formylphenylboronic acid with bromobenzene (1.33 mL, 12.47 mmol). Yield: 55%; Mp: 55 – 58 °C. ^{1}H NMR (300 MHz, $CDCl_3$): δ: 10.05 (1H, s, CHO), 7.24-8.02 (m, 9H) ppm. $C_{13}H_{10}O$.

4'-Methoxy-(1,1'-biphenyl)-4-carbaldehyde (**3b**): The product was obtained as a white solid after coupling 4-formylphenylboronic acid with 4-bromoanisole (1.56 mL, 12.47 mmol) and was purified using *n*-hexane/EtOAc (7:1). Yield: 27 %; Mp: 86 – 98 °C. ^{1}H NMR (300 MHz, $CDCl_3$): δ 10.02 (s,1H), 7.85 – 7.52 (m, 6H), 7.24 – 6.92(m, 2H), 3.84 (s, 3H). $C_{14}H_{12}O_2$.

2'-Methoxy-(1,1'-biphenyl)-4-carbaldehyde (**3c**): The product was obtained as a yellow solid after coupling 4-formylphenylboronic acid with 2-bromoanisole (1.79 mL, 12.47 mmol). Yield: 23 %; Mp: 48 – 51 °C. ^{1}H NMR (300 MHz, $CDCl_3$): δ 10.04 (s,1H), 7.99 – 7.74 (m, 4H), 7.27 – 6.94 (m, 4H), 3.82 (s, 3H). $C_{14}H_{12}O_2$.

3',4'-Dimethoxy-(1,1'-biphenyl)-4-carbaldehyde (**3d**): The product was obtained as a white solid after coupling 4-formylphenylboronic acid with 4-bromoveratrole (1.56 mL, 12.47 mmol), *n*-hexane/EtOAc (5:1). Yield: 38 %; Mp: 103.0 – 106.0 °C. ^{1}H NMR (300 MHz, $CDCl_3$): δ 10.02 (s,1H), 7.99 – 7.61 (m, 4H), 7.26 – 6.88 (m, 3H), 3.82 (s, 3H), 3.81 (s, 3H). $C_{15}H_{14}O_3$.

4'-Hydroxy-(1,1'-biphenyl)-4-carbaldehyde (**3e**): The product was obtained as a white solid after coupling 4-formylphenylboronic acid with 4-bromophenol (2.16 g, 12.47 mmol) and was purified using *n*-hexane/EtOAc (7:1). Yield: 37 %; Mp: 171 – 177 °C. ^{1}H NMR (300 MHz, $CDCl_3$): δ 10.51 (s, 1H), δ 8.19 – 8.12 (m, 4H), 7.80 – 7.78 (m, 2H), 7.72 – 7.66 (m, 2H). $C_{13}H_{10}O$.

4'-Fluoro-(1,1'-biphenyl)-4-carbaldehyde (**3f**): The product was obtained as a yellow solid after coupling 4-formylphenylboronic acid with 1-bromo-4-fluorobenzene (1.37 mL, 12.47 mmol) and was purified using , *n*-hexane/EtOAc (7:1). Yield: 36 %; Mp: 75 – 78 °C. ^{1}H NMR (300 MHz, $CDCl_3$): δ 10.05 (s,1H), 8.02 – 7.49 (m, 6H), 7.29 – 7.01 (m, 2H). $C_{13}H_9FO$.

4'-(Methylthio)-(1,1'-biphenyl)-4-carbaldehyde (**3g**): The product was obtained as a white solid after coupling 4-formylphenylboronic acid with 4-bromothioanisole (4.51 g, 22.19 mmol) and was purified using , *n*-hexane/EtOAc (7:1). Yield: 46 %; Mp: 85 – 89 °C. ^{1}H NMR (300 MHz, $CDCl_3$): δ 10.03 (s, 1H), 7.94 – 7.70 (m, 4H), 7.57 – 7.31 (m, 4H), 2.51 (s, 3H). $C_{14}H_{12}OS$.

4'-(Methylsulfonyl)-(1,1'-biphenyl)-4-carbaldehyde (**3h**): The product was obtained as a white solid after coupling 4-formylphenylboronic acid with 4-bromophenyl methyl sulfone (2.82 g, 12.01 mmol) and was purified using *n*-hexane/EtOAc (1:1). Yield: 42 %; Mp: 182 – 185 °C. ^{1}H NMR (300 MHz, $CDCl_3$): δ 10.08 (s, 1H), 8.02 (dd, *J* = 10, 8.0 Hz, 4H), 7.78 (dd, *J* = 9.3, 8.0 Hz, 4H), 3.10 (s, 3H). $C_{14}H_{12}O_3S$.

4-(Pyridin-4-yl)benzaldehyde (**3i**): The product was obtained as a white solid after coupling 4-formylphenylboronic acid with 4-bromopyridine hydrochloride (2.42 g, 6.23 mmol) and was purified using *n*-hexane/EtOAc (5:1). Yield: 51 %; Mp: 79 – 83 °C. ^{1}H NMR (300 MHz, $CDCl_3$): δ 10.08 (s, 1H), 8.76 – 8.66 (m, 2H), 8.08 – 7.48 (m, 6H). $C_{12}H_9NO$.

4-(Pyridin-3-yl)benzaldehyde (**3j**): The product was obtained as a white solid after coupling 4-formylphenylboronic acid with 3-bromopyridine (3.24 mL, 12.47 mmol) and was purified using *n*-hexane/EtOAc (5:1). Yield: 8 %; Mp: 58 – 61 °C. ^{1}H NMR (300 MHz, $CDCl_3$): δ 10.09 (s, 1H), 8.08 – 7.71 (m, 8H). $C_{12}H_9NO$.

(1,1'-Biphenyl)-3-carbaldehyde (**7a**): The product was obtained as a white solid after coupling 3-formylphenylboronic acid with bromobenzene (1.33 mL, 12.47 mmol) and was purified using *n*-hexane/EtOAc (5:1). Yield: 30 %; Mp: 59 – 60 °C. ^{1}H NMR (300 MHz, $CDCl_3$): δ: 10.07 (s, 1H), 8.08 (s, 1H), 7.86 – 7.83 (d, *J* =7.15 ,1H), 7.65 – 7.57 (d, *J* =7.15 ,4H), 7.49 – 7.38 (m, 3H) ppm. $C_{13}H_{10}O$.

4'-Methoxy-(1,1'-biphenyl)-3-carbaldehyde (**7b**): The product was obtained as a yellow oil after coupling 3-formylphenylboronic acid with 4-bromoanisole (1.56 mL, 12.47 mmol) and was purified using *n*-hexane/EtOAc (7:1). Yield: 61 %. ^{1}H NMR (300 MHz, $CDCl_3$): δ 10.05 (s, 1H), 8.03 – 7.47 (m, 6H), 7.04 – 6.90 (m, 2H), 3.83 (s, 1H). $C_{14}H_{12}O_2$.

2'-Methoxy-(1,1'-biphenyl)-3-carbaldehyde (**7c**): The product was obtained as a yellow oil after coupling 3-formylphenylboronic acid with 2-bromoanisole (1.79 mL, 12.47 mmol) and was purified using *n*-hexane/EtOAc (7:1). Yield: 41 %. ^{1}H NMR (300 MHz, $CDCl_3$): δ 10.05 (s, 1H), 8.02 – 7.64 (m, 4H), 7.37 – 6.93 (m, 4H), 3.81 (s, 1H). $C_{14}H_{12}O_2$.

3',4'-Dimethoxy-(1,1'-biphenyl)-3-carbaldehyde (**7d**): The product was obtained as a yellow oil after coupling 3-formylphenylboronic acid with 4-bromoveratrole (1.56 mL, 12.47 mmol), *n*-hexane/EtOAc (5:1). Yield: 53 %. ^{1}H NMR (300 MHz, $CDCl_3$): δ 10.05 (s, 1H), 8.04 – 8.03 (m, 1H), 7.81 – 7.77 (m, 2H), 7.56 (t, *J* = 7.6 Hz, 1H), 7.17 – 7.10 (m, 2H), 6.94 (d, *J* = 8.3 Hz, 1H), 3.93 (s, 3H), 3.91 (s, 3H). $C_{15}H_{14}O_3$.

4'-Fluoro-(1,1'-biphenyl)-3-carbaldehyde (**7f**): The product was obtained as a yellow oil after coupling 3-formylphenylboronic acid with 1-bromo-4-fluorobenzene (1.37 mL, 12.47 mmol) and was purified using , *n*-hexane/EtOAc (5:2). Yield: 69 %. ^{1}H NMR (300 MHz, $CDCl_3$): δ 10.10 (s, 1H), 8.13 – 7.14 (m, 8H).$C_{13}H_9FO$.

4'-(Methylthio)-(1,1'-biphenyl)-3-carbaldehyde (**7g**): The product was obtained as a yellow oil after coupling 3-formylphenylboronic acid with 4-bromothioanisole (4.51 g, 22.19 mmol) and was purified using , *n*-hexane/EtOAc (7:1). Yield: 54 %. ^{1}H NMR (300 MHz, $CDCl_3$): δ 10.06 (s, 1H), 8.06 (t, *J* = 1.8 Hz, 1H), 7.82 (ddd, *J* = 6.7, 2.0, 1.3 Hz, 2H), 7.63 – 7.49 (m, 3H), 7.38 – 7.28 (m, 2H), 2.51 (s,3H). $C_{14}H_{12}OS$.

6.1.2. General method to prepare intermediates 4a-h, 8a-g[169]

To a stirred solution of (1,1'-biphenyl)-4- or 3-carbaldehyde **3a-h** or **7a-h** (182 mg, 1.0 mmol) and CBr_4 (663 mg, 2.0 mmol) in anhydrous dichloromethane (10 mL) was added triphenylphosphine (1.05 g, 4.0 mmol) in portions over a period of 20 mins at 0 °C temperature under inert atmosphere. The reaction mixture turned brown and that was allowed to stir at 0 °C temperature for 2 h. After completion of reaction (monitored by TLC), reaction mixture was quenched with water (15 mL). The reaction mixture was extracted with dichloromethane (2 x 20 mL); organic layers were washed with brine (10 mL). The organic layers were dried over anhydrous $MgSO_4$; solvent was evaporated under reduced pressure to afford a crude residue, and crude residue was purified by column chromatography (silica gel, *n*-hexane/EtOAc, 5:1 or 7:1) to give the desired product, **4a-h, 8a-g** as a white solid. Yield: 20 – 92 %.

Physical and spectroscopy data for the synthesized compounds are provided below.

4-(2,2-Dibromovinyl)-1,1'-biphenyl (**4a**): The product was obtained as a white solid. Yield: 92 %; Mp: 106 – 108 °C. ^{1}H NMR (300 MHz, CDCl$_3$): δ: 7.60 – 7.32 (m, 9H), 7.24 (s, 1H) ppm. $C_{14}H_{10}Br_2$.

4-(2,2-Dibromovinyl)-4'-methoxy-1,1'-biphenyl (**4b**): The product was obtained as a white solid. Yield: 100 %; Mp: 98 – 102 °C. ^{1}H NMR (300 MHz, CDCl$_3$): δ 7.66 – 7.45 (m, 7H), 6.97 (d, J = 6.8 Hz, 2H), 3.84 (s, 3H). $C_{15}H_{12}Br_2O$.

4'-(2,2-Dibromovinyl)-2-methoxy-1,1'-biphenyl (**4c**): The product was obtained as a beige solid. Yield: 36 %; Mp: 68 – 71 °C. ^{1}H NMR (300 MHz, CDCl$_3$): δ 7.60 – 7.49 (m, 4H), 7.39 – 7.28 (m, 2H), 7.08 – 6.93 (m, 2H), 6.69 (s, 1H), 3.81 (s, 3H). $C_{15}H_{12}Br_2O$.

4'-(2,2-Dibromovinyl)-3,4-dimethoxy-1,1'-biphenyl (**4d**): The product was obtained as a white solid. Yield: 70 %; Mp: 91 – 95 °C. ^{1}H NMR (300 MHz, CDCl$_3$): δ 7.61 – 7.50 (m, 5H), 7.13 – 7.09 (m, 2H), 6.93 (s, 1H), 3.93 (s, 3H), 3.91 (s, 3H). $C_{16}H_{14}Br_2O_2$.

4'-(2,2-Dibromovinyl)-(1,1'-biphenyl)-4-ol (**4e**): The product was obtained as a white solid. Yield: 52 %; Mp: 180 – 184 °C. ^{1}H NMR (300 MHz, CDCl$_3$): δ 7.68 – 7.61 (m, 4H), 7.51 – 7.49 (m, 2H), 7.46 – 7.42 (m, 4H). $C_{14}H_{10}Br_2O$.

4-(2,2-Dibromovinyl)-4'-fluoro-1,1'-biphenyl (**4f**): The product was obtained as a white solid. Yield: 89 %; Mp: 58 – 61 °C. ^{1}H NMR (300 MHz, CDCl$_3$): δ 7.64 – 7.49 (m, 7H), 7.15 – 7.09 (m, 2H). $C_{14}H_9Br_2F$.

(4'-(2,2-Dibromovinyl)-(1,1'-biphenyl)-4-yl)(methyl)sulfane (**4g**): The product was obtained as a white solid. Yield: 82 %; Mp: 141 – 147 °C. ^{1}H NMR (300 MHz, CDCl$_3$): δ 7.66 – 7.45 (m, 8H), 7.31 (s, 1H), 2.51 (s, 3H). $C_{15}H_{12}Br_2S$.

4-(2,2-Dibromovinyl)-4'-(methylsulfonyl)-1,1'-biphenyl (**4h**): The product was obtained as a white solid. Yield: 72 %; Mp: 179 – 182 °C. ^{1}H NMR (300 MHz, $CDCl_3$): δ 8.04 – 7.95 (m, 2H), 7.77 (d, *J* = 8.5 Hz, 2H), 7.61 – 7.64 (m, 4H), 7.52 (s, 1H), 3.08 (s, 3H). $C_{15}H_{12}Br_2O_2S$.

4-(4-(2,2-Dibromovinyl)phenyl)pyridine (**4i**): The product was obtained as a white solid. Yield: 58 %; Mp: 112 – 115 °C. ^{1}H NMR (300 MHz, $CDCl_3$): δ 8.67 (br s, 1H), 7.74 – 7.59 (m, 4H), 7.59 – 7.38 (m, 4H). $C_{13}H_9Br_2N$.

3-(4-(2,2-Dibromovinyl)phenyl)pyridine (**4j**): The product was obtained as a white solid. Yield: 23 %; Mp: 96.1 – 101.0 °C. ^{1}H NMR (60 MHz, $CDCl_3$): 7.60 – 7.50 (m, 9H). $C_{13}H_9Br_2N$.

3-(2,2-Dibromovinyl)-1,1'-biphenyl (**8a**): The product was obtained as a yellow oil. Yield: 20 %. ^{1}H NMR (300 MHz, $CDCl_3$): δ: 7.74 (s, 1H), 7.57 – 7.53 (m, 4H), 7.49 – 7.40 (m, 5H) ppm. $C_{14}H_{10}Br_2$.

3-(2,2-Dibromovinyl)-4'-methoxy-1,1'-biphenyl (**8b**): The product was obtained as a pale yellow oil. Yield: 31 %. ^{1}H NMR (300 MHz, $CDCl_3$): δ 7.74 (s, 1H), 7.70 (s, 1H), 7.53 – 7.51 (m, 4H), 7.34 (t, *J* = 7.6 Hz, 1H), 6.95 (dd, *J* = 8.7, 6.4 Hz, 2H), 3.83 (s, 3H). $C_{15}H_{12}Br_2O$.

3'-(2,2-Dibromovinyl)-2-methoxy-1,1'-biphenyl (**8c**): The product was obtained as an orange oil. Yield: 82 %. ^{1}H NMR (300 MHz, $CDCl_3$): δ 7.70 (t, *J* = 1.7 Hz, 1H), 7.55 – 7.44 (m, 3H), 7.39 (t, *J* = 7.6 Hz, 1H), 7.36 – 7.26 (m, 2H), 7.08 – 6.94 (m, 2H), 3.81 (s, 3H). $C_{15}H_{12}Br_2O$.

3'-(2,2-Dibromovinyl)-3,4-dimethoxy-1,1'-biphenyl (**8d**): The product was obtained as a yellow oil. Yield: 61 %. ^{1}H NMR (300 MHz, CDCl3): δ 7.69 (t, *J* = 1.8 Hz, 1H), 7.56 – 7.40 (m, 4H), 7.15 – 7.06 (m, 2H), 6.93 (d, *J* = 8.3 Hz, 1H), 3.93 (s, 3H), 3.91 (s, 3H). $C_{16}H_{14}Br_2O_2$.

3-(2,2-Dibromovinyl)-4'-fluoro-1,1'-biphenyl (**8f**): The product was obtained as a yellow oil. Yield: 62 %. ^{1}H NMR (300 MHz, $CDCl_3$): δ 7.69 (t, *J* = 1.8 Hz, 1H), 7.55 – 7.48 (m, 4H), 7.47 – 7.34 (m, 2H), 7.16 – 7.07 (m, 2H). $C_{14}H_9Br_2F$.

(3'-(2,2-Dibromovinyl)-(1,1'-biphenyl)-4-yl)(methyl)sulfane (**8g**): The product was obtained as a pale yellow oil. Yield: 33 %. ^{1}H NMR (300 MHz, $CDCl_3$): δ 7.71 (d, *J* = 1.8 Hz, 1H), 7.54 – 7.47 (m, 4H), 7.47 – 7.38 (m, 2H), 7.38 – 7.26 (m, 2H), 2.51 (s, 3H). $C_{15}H_{12}Br_2S$.

6.1.3. General method to prepare final ethynylbiphenyl derivatives 5a-h, 9a-g[170]

To a stirred solution of dibromoalkene **4a-h, 8a-g** (200 mg, 0.59 mmol) in DMSO (4 mL), Cs_2CO_3 was added (483 mg, 1.48 mmol). The reaction was then stirred and heated at 60 °C for 18 h. The reaction mixture was extracted two times with EtOAc (100 mL), and distilled water (100 mL). The combined organic extracts were dried over $MgSO_4$ and filtered. The solvent was evaporated under reduced pressure to afford the crude product, which was then purified by column chromatography (silica gel, *n*-hexane/EtOAc (5:1 or 7:1)) to give the desired product, **5a-h** or **9a-h** as a white solid or yellow oil. Yield: 28 – 98 %.

Physical and spectroscopy data for the synthesized compounds are provided below.

4-Ethynyl-1,1'-biphenyl (**5a**): The product was obtained as a pale yellow solid. Yield: 53%; Mp: 78 – 80 °C. ^{1}H NMR (300 MHz, $CDCl_3$): δ 7.58 (t, *J* = 1.7 Hz, 2H), 7.55 – 7.54 (m, 4H), 7.46 – 7.41 (m, 2H), 7.38 – 7.31 (m, 1H), 3.11 (s, 1H). $C_{14}H_{10}$. Purity: 95%

4-Ethynyl-4'-methoxy-1,1'-biphenyl (**5b**): The product was obtained as a white solid. Yield: 28 %; Mp: 159 – 161 °C. ^{1}H NMR (300 MHz, $CDCl_3$): δ 7.60 – 7.41 (m, 6H), 7.02 – 6.89 (m, 2H), 3.84 (s, 3H), 3.09 (s, 1H). HRMS (ESI) m/z calcd for $C_{15}H_{12}O$ $[M+H]^+$ 209.09609, found: 209.0958. Purity: 99%

4'-Ethynyl-2-methoxy-1,1'-biphenyl (**5c**): The product was obtained as a yellow oil. Yield: 67 %. ^{1}HNMR (300 MHz, $CDCl_3$): δ 7.49 (d, *J* = 3.3 Hz, 4H), 7.30 (dd, *J* = 13.1, 8.5 Hz, 2H), 7.05 – 6.94 (m, 2H), 3.81 (s, 3H), 3.10 (s, 1H). $C_{15}H_{12}O$. Purity: 99%

4'-Ethynyl-3,4-dimethoxy-1,1'-biphenyl (5d): The product was obtained as a beige solid. Yield: 96 %; Mp: 139 – 145 °C. ^{1}H NMR (300 MHz, $CDCl_3$): δ 7.54 – 7.48 (m, 4H), 7.13 – 7.07 (m, 2H), 6.93 (d, *J* = 8.3 Hz, 2H), 3.93 (s, 3H), 3.91 (s, 3H), 3.10 (s, 1H). $C_{16}H_{14}O_2$. Purity: 100%

4'-Ethynyl-(1,1'-biphenyl)-4-ol (5e): The product was obtained as a beige solid. Yield: 43 %; Mp: 143 – 146.0 °C. ^{1}H NMR (300 MHz, CDCl3): δ 7.48 – 7.40 (m, 6H), 6.91 – 6.88 (m, 2H), 3.09 (s, 1H). $C_{14}H_{10}O$. Purity: 99%

4-Ethynyl-4'-fluoro-1,1'-biphenyl (5f): The product was obtained as a yellow solid and was purified using *n*-hexane/EtOAc (5:1). Yield: 92 %; Mp: 85 – 89 °C. ^{1}H NMR (300 MHz, $CDCl_3$): δ 7.55 – 7.46 (m, 6H), 7.14 – 7.08 (m, 2H), 3.11 (s, 1H). $C_{14}H_9F$. Purity: 99%

(4'-Ethynyl-(1,1'-biphenyl)-4-yl)(methyl)sulfane (5g): The product was obtained as a pale yellow solid. Yield: 50 %; Mp: 206 – 209 °C. ^{1}H NMR (300 MHz, $CDCl_3$): δ 7.54 – 7.47 (m, 6H), 7.34 – 7.28 (m, 2H), 3.11 (s, 1H), 2.51 (s, 3H). $C_{15}H_{12}S$. Purity: 96%

4-Ethynyl-4'-(methylsulfonyl)-1,1'-biphenyl (5h): The product was obtained as a white solid. Yield: 30 %; Mp: 204 – 207 °C. ^{1}H NMR (300 MHz, $CDCl_3$): δ 8.01 – 7.99 (m, 2H), 7.76 – 7.73 (m, 2H), 7.58 – 7.56 (d, *J* = 4.2 Hz, 4H), 3.16 (s, 1H), 3.08 (s, 3H). HRMS (ESI) m/z calcd for $C_{15}H_{12}O_2S$ $[M+H]^+$ 257.0631, found: 257.0623. Purity: 100%

4-(4-Ethynylphenyl)pyridine (5i): The product was obtained as a white solid. Yield: 33 %; Mp: 182 – 185 °C. ^{1}H NMR (300 MHz, $CDCl_3$): δ 7.54 – 7.47 (m, 6H), 7.34 – 7.28 (m, 2H), 3.11 (s, 1H), 2.51 (s, 3H). $C_{13}H_9N$. Purity: 97%

3-(4-Ethynylphenyl)pyridine (5j): The product was obtained as a yellow solid. Yield: 46 %; Mp: 153 – 156 °C. ^{1}H NMR (300 MHz, $CDCl_3$): δ 7.58 (t, *J* = 1.8 Hz, 1H), 7.56 – 7.54 (m, 4H), 7.53 (dd, *J* = 8.8, 6.4 Hz, 1H), 7.51 – 7.50 (m, 2H), 3.12 (s, 1H). $C_{13}H_9N$. Purity: 100%

3-Ethynyl-1,1'-biphenyl (**9a**): The product was obtained as a pale yellow oil. Yield: 69. %. ^{1}H NMR (300 MHz, CDCl$_3$): δ 7.72 (s, 1H), 7.58 – 7.55 (d, *J* = 4.2 Hz, 3H), 7.47 – 7.35 (m, 5H), 3.09 (s, 1H). $C_{14}H_{10}$. Purity: 99%

3-Ethynyl-4'-methoxy-1,1'-biphenyl (**9b**): The product was obtained as an orange oil. Yield: 41 %. ^{1}H NMR (300 MHz, CDCl3): δ 7.72 – 7.63 (m, 1H), 7.60 – 7.39 (m, 4H), 7.34 (t, *J* = 7.6 Hz, 1H), 6.95 (dd, *J* = 8.7, 6.4 Hz, 2H), 3.83 (s, 3H), 3.07 (s, 1H). $C_{15}H_{12}O$. Purity: 96%

3'-Ethynyl-2-methoxy-1,1'-biphenyl (**9c**): The product was obtained as a yellow oil. Yield: 70 %. ^{1}H NMR (300 MHz, CDCl$_3$): δ 7.66 (d, *J* = 1.8 Hz, 1H), 7.52 (dt, *J* = 7.7, 1.6 Hz, 1H), 7.45 (dt, *J* = 7.7, 1.5 Hz, 1H), 7.42 – 7.25 (m, 3H), 7.08 – 6.94 (m, 2H), 3.81 (s, 3H), 3.07 (s, 1H). $C_{15}H_{12}O$. Purity: 100%

3'-Ethynyl-3,4-dimethoxy-1,1'-biphenyl (**9d**): The product was obtained as a white solid. Yield: 51 %; Mp: 118 – 122 °C. ^{1}H NMR (300 MHz, CDCl$_3$): δ 7.67 (d, *J* = 1.8 Hz, 1H), 7.52 (dt, *J* = 7.7, 1.9 Hz, 1H), 7.47 – 7.38 (m, 1H), 7.34 (d, *J* = 7.7 Hz, 1H), 7.16 – 7.03 (m, 2H), 6.93 (d, *J* = 8.3 Hz, 1H), 3.93 (s, 3H), 3.91 (s, 3H), 3.09 (s, 1H). $C_{16}H_{14}O_2$. Purity: 100%

3-Ethynyl-4'-fluoro-1,1'-biphenyl (**9f**): The product was obtained as a yellow oil. Yield: 57 %. ^{1}H NMR (300 MHz, CDCl$_3$): δ 7.69 (t, *J* = 1.8 Hz, 1H), 7.55 – 7.48 (m, 3H), 7.47 – 7.34 (m, 2H), 7.16 – 7.07 (m, 2H), 3.12 (s, 1H). $C_{14}H_9F$. Purity: 99%

(4'-Ethynyl-(1,1'-biphenyl)-4-yl)(methyl)sulfane (**9g**): The product was obtained as a pale yellow solid. Yield: 68 %; Mp: 47 – 51 °C. ^{1}H NMR (300 MHz, CDCl$_3$): δ 7.68 (d, *J* = 1.8 Hz, 1H), 7.55 – 7.49 (m, 2H), 7.48 – 7.42 (m, 2H), 7.37 (dd, *J* = 7.7, 0.7 Hz, 1H), 7.33 – 7.28 (m, 2H), 3.08 (s, 1H), 2.51 (s, 3H). $C_{15}H_{12}S$.

6.1.4. General method to prepare intermediate 11[171]

Under argon atmosphere, $Pd(PPh_3)_2$ (0.594 g, 0.85 mmol) was combined with CuI (0.081 g, 0.42 mmol), 5-bromo-2-iodopyridine (**10**, Scheme 3.4), and Et_3N (1.00 ml, 7.14 mmol) in THF solution (10 mL) in 100 mL RB flask. The reaction was then stirred and heated at 80°C for 9 h. The reaction mixture was extracted two times with EtOAc (100 mL), and distilled water (100 mL). The combined organic extracts were dried over $MgSO_4$ and filtered. The solvent was evaporated under reduced pressure to afford the crude product, which was then purified by column chromatography (silica gel, *n*-hexane/EtOAc (7:1)) to give the desired product, **11**, as an orange solid. Yield: 91 %.

Physical and spectroscopy data for **11** is given below.

5-Bromo-2-((trimethylsilyl)ethynyl)pyridine (**11**): The product was obtained as an orange solid after coupling with 5-bromo-2-iodopyridine (2.00 g, 7.05 mmol) and was purified using *n*-hexane/EtOAc (7:1). Yield: 91 %; Mp: 45 – 48 °C. ^1H NMR (300 MHz, $CDCl_3$): δ 8.61 (s, 1H), 7.77 (dd, *J* = 8.3 Hz, 1H), 7.30 (d, *J* = 7.7 Hz, 1H), 0.24 (s, 9H). $C_{10}H_{12}BrNSi$.

6.1.5. General method to prepare intermediate 12[172]

To a stirred solution of 5-bromo-2-((trimethylsilyl)ethynyl)pyridine (**11**) (1.50 g, 5.90 mmol) in MeOH (20 mL), aq. NaOH (6N, 7.40 mL, 5.90 mmol) solution was added. The reaction mixture was allowed to stir at room temperature for 2 h. After completion of the reaction (monitored by TLC), acetic acid was added (0.340 mL) to the reaction mixture and was quenched with water (15 mL). The reaction mixture was extracted with dichloromethane (2 x 20 mL); organic layers were washed with brine (10 mL). The organic layers were dried over anhydrous $MgSO_4$; solvent was evaporated under reduced pressure to afford a crude residue, and crude residue was purified by column chromatography (silica gel, *n*-hexane/EtOAc, 7:1) to give the desired product, **12** as a beige solid. Yield: 69 %.

5-Bromo-2-ethynylpyridine (**12**): The product was obtained as a beige solid and was purified using *n*-hexane/EtOAc (7:1). Yield: 69 %; Mp: 86 – 87 °C. ^{1}H NMR (300 MHz, $CDCl_3$): δ 8.61 (s, 1H), 7.79 (dd, *J* = 8.3 Hz, 1H), 7.32 (d, *J* = 8.3 Hz, 1H), 3.18 (s, 1H). C_7H_4BrN.

6.1.6. General method to prepare ethynylpyridyl derivative 14[168]

Under argon atmosphere, $Pd(OAc)_2$ (0.008 g, 0.03 mmol) was combined with Xantphos (0.020 g, 0.03 mmol) in degassed THF (7.5 mL). After stirring for 5 min, this resulting solution was added into a separate round-bottom-flask (RBF) containing 5-bromo-2-ethynylpyridine (**12**) (250 mg, 1.37 mmol), phenylboronic acid (**13**, Scheme 3.4) (179 mg, 1.47 mmol), and K_3PO_4 (875 mg, 4.12 mmol). The reaction was then stirred and heated at 60°C for 18 h. The reaction mixture was extracted two times with DCM (100 mL), and distilled water (100 mL). The combined organic extracts were dried over $MgSO_4$ and filtered. The solvent was evaporated under reduced pressure to afford the crude product, which was then purified by column chromatography (silica gel, *n*-hexane/EtOAc (1:1)) to give the desired product, **14** as a brown solid. Yield: 52 %.

2-Ethynyl-5-phenylpyridine (**14**): The product was obtained as a brown solid and was purified using , *n*-hexane/EtOAc (1:1). Yield: 52 %; Mp: 86 – 90 °C. ^{1}H NMR (300 MHz, $CDCl_3$): δ 8.82 (dd, *J* = 2.4, 0.9 Hz, 1H), 7.83 (dd, *J* = 8.1, 2.4 Hz, 1H), 7.59 – 7.40 (m, 6H), 3.18 (s, 1H). HRMS (ESI) m/z calcd for $C_{13}H_9N$ $[M+H]^+$ 180.0808, found: 180.0811. Purity: 100%.

6.2. Biological Assay Methodology

6.2.1. Aβ Aggregation Assay

The anti-Aβ aggregation activity of the ethynyl-1,1'-biphenyl derivatives and other compounds was evaluated using the ThT-based fluorescence assay.[173,174] The assay was carried out using Costar 384-well flat, clear bottom black plates. The $A\beta_{1-40}$ and $A\beta_{1-42}$ hexafluoro-2-propanol (HFIP) (obtained from rPeptide, USA) stock solutions were prepared to obtain a final concentration of 1 mg/mL; via dissolving 0.5 mg of $A\beta_{1-40}$ in 1% NH_4OH solution and 10% NH_4OH solution for $A\beta_{1-42}$. This was followed by dilution in 215 mM phosphate buffer (pH 7.4) to obtain a final concentration of 500 μM. Stock solutions of compounds and derivatives was prepared in DMSO and diluted in 215 mM phosphate buffer (pH 7.4) to prepare various concentrations (1, 5, 10 and 25 μM). In 50 mM glycine buffer (pH 7.4), 15 μM ThT fluorescent dye stock solution was prepared. To each test compound containing well, 44 μL of ThT, 20 μl of 215 mM phosphate buffer (pH 7.4), and 8 μl of ethynylbiphenyl compound in different concentrations and 8 μl of 50 μM $A\beta_{1-40/1-42}$ was added. To each ThT background well, 44 μL of ThT, 35 μl of 215 mM phosphate buffer (pH 7.4), and 1 μl of DMSO was added. To the control wells containing only Aβ, 44 μL ThT, 28 μL of 215 mM phosphate buffer, and eight μL $A\beta_{1-40/1-42}$ (final concentration 5 μM) was added. To the control wells containing ethynylbiphenyl compound, 44 μL ThT, 28 μL of 215 mM phosphate buffer, and eight μL ethynylbiphenyl compound (25 μM) was added. In order to determine ThT-interference, the relative fluorescence units (RFU) from these compounds only wells were subtracted from Aβ + compound treated wells. The plate was read every 5 minutes using a BioTek Synergy H1 microplate reader, at 37 °C for 24 h, with ThT excitation measured at 440 nm, excitation and emission at 490 nm. The known Aβ aggregation inhibitor methylene blue was used as reference compounds. Data for each compound was presented based on an average of triplicate reading based on two to three independent experiments.

6.2.2. Transmission electron microscopy (TEM)

The Aβ aggregate morphology was evaluated by carrying out transmission electron microscopy (TEM) in the presence and absence of test compounds. TEM samples were prepared via A$\beta_{1-40/42}$ incubation with compound (25 μM) or control in Costar 384-well flat, clear bottom black plates.[173] To each compound containing well, 44 μL of ThT, 20 μl of 215 mM phosphate buffer (pH 7.4), and 8 μl of biphenyl compound in different concentrations and 8 μl of 50 μM A$\beta_{1-40/42}$. At a concentration of 25 μM for compound, the final A$\beta_{1-40/42}$ to compound ratio was be 1:1. To the control wells containing only Aβ, 44 μL ThT, 28 μL of 215 mM phosphate buffer, and eight μL A$\beta_{1-40/42}$ (final concentration 5 μM) was added. To the control wells containing only compound, 44 μL ThT, 28 μL of 215 mM phosphate buffer, and 8 μL compound (25 uM) was added. The plate was be incubated at 37 °C for 24 h, using a BioTek Synergy H1 microplate reader. To prepare the TEM grids, 20 μL of incubated solution was added over the formvar-coated copper grids (400 mesh) and allowed to air dry overnight. The grids were washed to remove any precipitated buffer salts through two additions of approximately 20 μL Ultrapure Water (UPW), followed by blotting via filter paper and air drying for 30 min. After grids were fully dried, staining of the grids was achieved through the addition of 20 μL of 2% phosphotungstic acid (PTA), causing aggregates to be stained. This PTA was removed through blotting with filer paper and the grids were air-dried overnight. Scanning of these grids was done using a Philips CM 10 transmission electron microscope at 60 kV (Department of Biology, University of Waterloo) and micrographs were obtained using a 14-megapixel AMT camera.[173]

6.3 Computational Chemistry

Molecular docking studies were carried out using the computational chemistry software Discovery Studio (DS) – *Structure-Based-Design* (SBD), version 4.0 from BIOVIA Inc. (San Diego, USA). The coordinates of solid-state NMR structure of A$\beta_{1\text{-}40}$ fibril (pdb id: 2LMN) and magic angle spinning NMR structure of A$\beta_{1\text{-}42}$ fibril (pdb id: 5KK3) were obtained from RCSB protein data bank.[181,183] These structures were used to construct either dimer or tetramer β-sheet assemblies as representative A$\beta_{1\text{-}40}$ and A$\beta_{1\text{-}42}$ dimer or oligomer models. The dimer or oligomer assembly was prepared using the *macromolecules* module in DS by assigning force fields (CHARMm force field). Ethynyl-1,1'-biphenyl compounds were built in 3D using Build Fragment tool, and energy minimization was performed for 1000 iterations using steepest descent and conjugate gradient minimizations respectively. The ligands were energy minimized using the *smart minimizer* protocol (200 steps, RMS gradient 0.1 kcal/mol), CHARMm force field and a distance depended dielectric constant. For the docking of ethynyl-biphenyl derivatives in Aβ-dimer models, the binding site was defined by considering the KLVFF segment to create a 25 Å sphere whereas, for the oligomer docking the binding site for A$\beta_{1\text{-}40}$ tetramer assembly was defined by creating a 20 Å radius sphere after selecting amino acids Phe19, Phe20, Ala21 and Ile31, Ile32 and Gly33 from the central two strands (strands 2 and 3). For the A$\beta_{1\text{-}42}$ tetramer assembly, the binding site was defined by creating a 20 Å radius sphere after selecting amino acids Leu17 and Leu34 from the central two strands (strands 2 and 3). Then the test compounds were docked using the CDOCKER algorithm in DS Studio by employing 100 hotspots and a docking tolerance of 0.25 Å. Docked poses were subjected to smart minimizer algorithm (0.001 kcal/mol, 1000 steps) using CHARMM force field and a distance depended dielectric constant. The binding poses obtained were ranked by assessing the complex energies in kcal/mol (CDOCKER energy and

CDOCKER interaction energy).[181,183] In addition, polar and nonpolar contact of the ethynyl-biphenyl derivatives with either Aβ_{1-40} or Aβ_{1-42} dimer and oligomer assemblies were analyzed, and distance parameters were noted.

References

1. Gaugler, J.; James, B.; Johnson, T.; Scholz, K.; Weuve, J. 2016 Alzheimer's disease facts and figures. *Alzheimer's Dementia* **2016***, 12*, 459–509.

2. Scheltens, P.; Blennow, K.; Breteler, M. M. B.; de Strooper, B.; Frisoni, G. B.; Salloway, S.; Van der Flier, W M Alzheimer's disease. *Lancet* **2016***, 388*, 505–517.

3. Madav, Y.; Wairkar, S.; Prabhakar, B. Recent therapeutic strategies targeting beta amyloid and tauopathies in Alzheimer's disease. *Brain Res. Bull.* **2019***, 146*, 171–184.

4. Wong, S. L.; Gilmour, H.; Ramage-Morin, P. L. Alzheimer's disease and other dementias in Canada. *Health Reports* **2016***, 27*, 11–16.

5. Alves, L.; Correia, A. S. A.; Miguel, R.; Alegria, P.; Bugalho, P. Alzheimer's disease: A clinical practice-oriented review. *Front. Neurol.* **2012***, 3*, 1 – 20.

6. Duboisa, B.; Padovanib, A.; Scheltensc, P.; Rossid, A.; Agnello, G. D. Timely diagnosis for Alzheimer's disease: A literature review on benefits and challenges. *J. Alzheimer's Dis.* **2016***, 49*, 617–631.

7. Swerdlow, R. H. Pathogenesis of Alzheimer's disease. *Clin Interv Aging* **2007***, 2*, 347–359.

8. Sabbagh, M. N.; Lue, L.; Fayard, D.; Shi, J. Increasing precision of clinical diagnosis of Alzheimer's disease using a combined algorithm incorporating clinical and novel biomarker data. *Neurol. Ther.* **2017***, 6*, 83–95.

9. Zhao, W.; Cui, W.; Xu, S.; Cheong, L.; Shen, C.; Examination of Alzheimer's disease by a combination of electrostatic force and mechanical measurement. *J. Microsc.* **2019***, 275*, 66–72.

10. LaFerla, F. M.; Green, K. N.; Oddo, S. Intracellular amyloid-ß in Alzheimer's disease. *Nat. Rev. Neurosci.* **2007***, 8*, 499–509.

11. Amadoro, G.; Corsetti, V.; Atlante, A.; Florenzano, F.; Capsoni, S.; Bussani, R.; Mercanti, D.; Calissano, P. Interaction between NH 2-tau fragment and Aß in Alzheimer's disease mitochondria contributes to the synaptic deterioration. *Neurobiol. Aging* **2012***, 33*, 833.e1–833.e25.

12. Walsh, D. M.; Selkoe, D. J. Deciphering the molecular basis of memory failure in Alzheimer's disease. *Neuron* **2004***, 44*, 181–193.

13. LaFerla, F. M.; Oddo, S. Alzheimer's disease: Aß, tau and synaptic dysfunction. *Trends Mol. Med.* **2005***, 11*, 170–176.

14. Bao, F.; Wicklund, L.; Lacor, P. N.; Klein, W. L.; Nordberg, A.; Marutle, A. Different ß-amyloid oligomer assemblies in Alzheimer brains correlate with age of disease onset and impaired cholinergic activity. *Neurobiol. Aging* **2012***, 33*, 825.e1–825.e13.

15. Arendt, T. Synaptic degeneration in Alzheimer's disease. *Acta Neuropathol.* **2009***, 118*, 167–179.

16. Mohamed, T.; Yeung, J. C. K.; Vasefi, M. S.; Beazely, M. A.; Rao, P. P. N. Development and evaluation of multifunctional agents for potential treatment of Alzheimer's disease:

Application to a pyrimidine-2,4-diamine template. *Bioorg. Med. Chem. Lett.* **2012***, 22*, 4707–4712.

17. Mohamed, T.; Shakeri, A.; Rao, P. P. N. Amyloid cascade in Alzheimer's disease: Recent advances in medicinal chemistry. *Eur. J. Med. Chem.* **2016***, 113*, 258–272.

18. Mohamed, T.; Rao, P. P. N. 2,4-Disubstituted quinazolines as amyloid-ß aggregation inhibitors with dual cholinesterase inhibition and antioxidant properties: Development and structure-activity relationship (SAR) studies. *Eur. J. Med. Chem.* **2017***, 126*, 823–843.

19. Maurer, S. V.; Williams, C. L. The cholinergic system modulates memory and hippocampal plasticity via its interactions with non-neuronal cells. *Front. Immunol.* **2017***, 8*.

20. Mohamed, T.; Rao, P. P. N. Alzheimer's disease: Emerging trends in small molecule therapies. *Curr. Med. Chem.* **2011***, 18*, 4299–4320.

21. Baxter, M. G.; Frick, K. M.; Price, D. L.; Breckler, S. J.; Markowska, A. L.; Gorman, L. K. Presynaptic markers of cholinergic function in the rat brain: Relationship with age and cognitive status. *Neuroscience* **1999***, 89*, 771–780.

22. Parent, M. B.; Baxter, M. G. Septohippocampal Acetylcholine: Involved in but not necessary for learning and memory? *Learn. Mem.* **2004***, 11*, 9–20.

23. Park, G. A. S.; Pappas, B. A.; Murtha, S. M.; Ally, A. Enriched environment primes forebrain choline acetyltransferase activity to respond to learning experience. *Neurosci. Lett.* **1992***, 143*, 259–262.

24. Bierer, L. M.; Haroutunian, V.; Gabriel, S.; Knott, P. J.; Carlin, L. S.; Purohit, D. P.; Perl, D. P.; Schmeidler, J.; Kanof, P.; Davis, K. L. Neurochemical correlates of dementia severity in Alzheimer's disease: relative importance of the cholinergic deficits. *J. Neurochem.* **1995***, 64*, 749–760.

25. Cummings, J.; Lee, G.; Ritter, A.; Zhong, K. Alzheimer's disease drug development pipeline: 2018. *Alzheimers Dement. Transl. Res. Clin. Interv.* **2018***, 4*, 195–214.

26. Vinters, H. V. Emerging concepts in Alzheimer's disease. *Annu. Rev. Pathol. Mech. Dis.* **2015***, 10*.

27. Ahmed, R. R.; Holler, C. J.; Webb, R. L.; Li, F.; Beckett, T. L.; Murphy, M. P. BACE1 and BACE2 enzymatic activities in Alzheimer's disease. *J. Neurochem.* **2010***, 112*, 1045–1053.

28. Plummer, S.; Van den Heuvel, C.; Thornton, E.; Corrigan, F.; Cappai, R. The neuroprotective properties of the amyloid precursor protein following traumatic brain injury. *Aging Dis.* **2016***,* *7*, 163–179.

29. Maynard, C. J.; Cappai, R.; Volitakis, I.; Cherny, R. A.; White, A. R.; Beyreuther, K.; Masters, C. L.; Bush, A. I.; Li, Q. Overexpression of Alzheimer's disease amyloid-ß opposes the age-dependent elevations of brain copper and iron. *J. Biol. Chem.* **2002***, 277*, 44670–44676.

30. Klaver, D.; Hung, A. C.; Gasperini, R.; Foa, L.; Aguilar, M. Small, D. H. Effect of heparin on APP metabolism and Aß production in cortical neurons. *Neurodegenerative Dis.* **2010***, 7*, 187–189.

31. Cheng, F.; Cappai, R.; Lidfeldt, J.; Belting, M.; Fransson, L.; Mani, K. Amyloid precursor protein (APP)/APP-like protein 2 (APLP2) expression is required to initiate endosome-nucleus-autophagosome trafficking of glypican-1-derived heparan sulfate. *J. Biol. Chem.* **2014***, 289*, 20871–20878.

32. Needham, B. E.; Wlodek, M. E.; Ciccotosto, G. D.; Fam, B. C.; Masters, C. L.; Proietto, J.; Andrikopoulos, S.; Cappai, R. Identification of the Alzheimer's disease amyloid precursor protein (APP) and its homologue APLP2 as essential modulators of glucose and insulin homeostasis and growth. *J. Pathol.* **2008***, 215*, 155–163.

33. Gralle, M.; Botelho, M. G.; Wouters, F. S. Neuroprotective secreted amyloid precursor protein acts by disrupting amyloid precursor protein dimers. *J. Biol. Chem.* **2009***, 284*, 15016–15025.

34. Sakono, M.; Zako, T. Amyloid oligomers: Formation and toxicity of Aß oligomers. *FEBS J.* **2010***, 277*, 1348–1358.

35. Bruggink, K. A.; Müller, M.; Kuiperij, H. B.; Verbeek, M. M. Methods for analysis of amyloid-ß aggregates. *J. Alzheimer's Dis.* **2012***, 28*, 735–758.

36. Chow, V. W.; Mattson, M. P.; Wong, P. C.; Gleichmann, M. An overview of APP processing enzymes and products. *Neuromolecular Med.* **2010***, 12*, 1–12.

37. Zhang, X.; Li, Y.; Xu, H.; Zhang, Y. -. The γ-secretase complex: From structure to function. *Front. Cell. Neurosci.* **2014***, 8*.

38. Hunt, C. E.; Turner, A. J. Cell biology, regulation and inhibition of ß-secretase (BACE-1). *FEBS J.* **2009***, 276*, 1845–1859.

39. Guglielmotto, M.; Aragno, M.; Autelli, R.; Giliberto, L.; Novo, E.; Colombatto, S.; Danni, O.; Parola, M.; Smith, M. A.; Perry, G.; Tamagno, E.; Tabaton, M. The up-regulation of BACE1 mediated by hypoxia and ischemic injury: Role of oxidative stress and HIF1a. *J. Neurochem.* **2009***, 108*, 1045–1056.

40. De Strooper, B. Aph-1, Pen-2, and Nicastrin with Presenilin generate an active γ-secretase complex. *Neuron* **2003***, 38*, 9–12.

41. Iwatsubo, T. The γ-secretase complex: Machinery for intramembrane proteolysis. *Curr. Opin. Neurobiol.* **2004***, 14*, 379–383.

42. Adeniji, A. O.; Adams, P. W.; Mody, V. V. Chapter 7 - Amyloid β Hypothesis in the Development of Therapeutic Agents for Alzheimer's Disease. In *Drug Discovery Approaches for the Treatment of Neurodegenerative Disorders,* 2017; pp 109-143.

43. Vingtdeux, V.; Marambaud, P. Identification and biology of α-secretase. *J. Neurochem.* **2012***, 120*, 34–45.

44. Gall, S. M. L.; Bobé, P.; Reiss, K.; Horiuchi, K.; Niu, X.; Lundell, D.; Gibb, D. R.; Conrad, D.; Saftig, P.; Blobel, C. P. ADAMs 10 and 17 represent differentially regulated components of a general shedding machinery for membrane proteins such as transforming growth factor a, l-selectin, and tumor necrosis factor a. *Mol. Biol. Cell* **2009***, 20*, 1772–1784.

45. Kohutek, Z. A.; DiPierro, C. G.; Redpath, G. T.; Hussaini, I. M. ADAM-10-Mediated N-Cadherin Cleavage Is Protein Kinase C-a Dependent and Promotes Glioblastoma Cell Migration. *J. Neurosci.* **2009***, 29*, 4605–4615.

46. Vassar, R. BACE1 inhibitor drugs in clinical trials for Alzheimer's disease. *Alzheimers Res. Ther.* **2014**, *6*.

47. Cole, S. L.; Vassar, R. The Alzheimer's disease ß-secretase enzyme, BACE1. *Mol. Neurodegeneration* **2007**, *2*.

48. Wolfe, M. S. Inhibition and modulation of γ-secretase for Alzheimer's Disease. *Neurotherapeutics* **2008**, *5*, 391–398.

49. Beel, A. J.; Sanders, C. R. Substrate specificity of γ-secretase and other intramembrane proteases. *Cell Mol. Life Sci.* **2008**, *65*, 1311–1334.

50. Zheng, J.; Ma, B.; Nussinov, R. Consensus features in amyloid fibrils: Sheet-sheet recognition via a (polar or nonpolar) zipper structure. *Phys. Biol.* **2006**, *3*, P1–P4.

51. Nakamura, M.; Shishido, N.; Nunomura, A.; Smith, M. A.; Perry, G.; Hayashi, Y.; Nakayama, K.; Hayashi, T. Three histidine residues of amyloid-ß peptide control the redox activity of copper and iron. *Biochemistry* **2007**, *46*, 12737–12743.

52. Gazit, E. Mechanisms of amyloid fibril self-assembly and inhibition: Model short peptides as a key research tool. *FEBS J.* **2005**, *272*, 5971–5978.

53. Smith, D. G.; Cappai, R.; Barnham, K. J. The redox chemistry of the Alzheimer's disease amyloid peptide. *Biochim. Biophys. Acta Biomembr.* **2007**, *1768*, 1976–1990.

54. Bazan, N.; Lukiw, W. Cyclooxygenase-2 and presenilin-1 gene expression induced by interleukin-1 beta and amyloid beta 42 peptide is potentiated by hypoxia in primary human neural cells. *J. Biol. Chem.* **2002***, 277*, 30359–30367.

55. Xu, J.; Chen, S.; Ahmed, S. H.; Chen, H.; Ku, G.; Goldberg, M. P.; Hsu, C. Y. Amyloid-beta peptides are cytotoxic to oligodendrocytes. *J. Neurosci.* **2001***, 21*.

56. Bazan, N. G. Neuroprotectin D1 (NPD1): A DHA-derived mediator that protects brain and retina against cell injury-induced oxidative stress. *Brain Pathol.* **2005***, 15*, 159–166.

57. Yamamoto, N.; Matsubara, E.; Maeda, S.; Minagawa, H.; Takashima, A.; Maruyama, W.; Michikawa, M.; Yanagisawa, K. A ganglioside-induced toxic soluble Aß assembly: Its enhanced formation from Aß bearing the arctic mutation. *J. Biol. Chem.* **2007***, 282*, 2646–2655.

58. Yanagisawa, K. Role of gangliosides in Alzheimer's disease. *Biochim. Biophys. Acta Biomembr.* **2007***, 1768*, 1943–1951.

59. De Felice, F. G.; Velasco, P. T.; Lambert, M. P.; Viola, K.; Fernandez, S. J.; Ferreira, S. T.; Klein, W. L. Aß oligomers induce neuronal oxidative stress through an N-methyl-D-aspartate receptor-dependent mechanism that is blocked by the Alzheimer drug memantine. *J. Biol. Chem.* **2007***, 282*, 11590–11601.

60. Shankar, G. M.; Bloodgood, B. L.; Townsend, M.; Walsh, D. M.; Selkoe, D. J.; Sabatini, B. L. Natural oligomers of the Alzheimer amyloid-ß protein induce reversible synapse loss by

modulating an NMDA-type glutamate receptor-dependent signaling pathway. *J. Neurosci.* **2007***, 27*, 2866–2875.

61. Soto, C. Unfolding the role of protein misfolding in neurodegenerative diseases. *Nat. Rev. Neurosci.* **2003***, 4*, 49–60.

62. Kawahara, M.; Kuroda, Y. Molecular mechanism of neurodegeneration induced by Alzheimer's ß-amyloid protein: Channel formation and disruption of calcium homeostasis. *Brain Res. Bull.* **2000***, 53*, 389–397.

63. LaFerla, F. M.; Green, K. N.; Oddo, S. Intracellular amyloid-ß in Alzheimer's disease. *Nat. Rev. Neurosci.* **2007***, 8*, 499–509.

64. Yan, S. D.; Fu, J.; Soto, C.; Chen, X.; Zhu, H.; Al-Mohanna, F.; Collison, K.; Zhu, A.; Stern, E.; Saido, T.; Tohyama, M.; Ogawa, S.; Roher, A.; Stern, D. An intracellular protein that binds amyloid-ß peptide and mediates neurotoxicity in Alzheimer's disease. *Nature* **1997***, 389*, 689–695.

65. Yang, A. J.; Chandswangbhuvana, D.; Margol, L.; Glabe, C. G. Loss of endosomal/lysosomal membrane impermeability is an early event in amyloid Aß1-42 pathogenesis. *J. Neurosci. Res.* **1998***, 52*, 691–698.

66. Marr, R.; Hafez, D. Amyloid beta and Alzheimer's disease: The role of neprilysin-2 in amyloid-beta clearance. *Front. Aging Neurosci.* **2014***, 6*.

67. Zheng, J.; Ma, B.; Nussinov, R. Consensus features in amyloid fibrils: Sheet-sheet recognition via a (polar or nonpolar) zipper structure. *Phys. Biol.* **2006***, 3*, P1–P4.

68. Bu, X.; Rao, P. P. N.; Wang, Y. Anti-amyloid aggregation activity of natural compounds: Implications for Alzheimer’s drug discovery. *Mol. Neurobiol.* **2016**, *53*, 3565–3575.

69. Pearson, H. A.; Peers, C. Physiological roles for amyloid ß peptides. *J. Physiol.* **2006**, *575*, 5–10.

70. Koudinov, A. R.; Berezov, T. T. Alzheimer's amyloid-beta (Aß) is an essential synaptic protein, not neurotoxic junk. *Acta Neurobiol. Exp.* **2004**, *64*, 71–79.

71. Giuffrida, M. L.; Tomasello, M. F.; Pandini, G.; Caraci, F.; Battaglia, G.; Busceti, C.; Di Pietro, P.; Pappalardo, G.; Attanasio, F.; Chiechio, S.; Bagnoli, S.; Nacmias, B.; Sorbi, S.; Vigneri, R.; Rizzarelli, E.; Nicoletti, F.; Copani, A. Monomeric ß-amyloid interacts with type-1 insulin-like growth factor receptors to provide energy supply to neurons. *Front. Cell. Neurosci.* **2015**, *9*.

72. Palop, J. J.; Mucke, L. Amyloid-B-induced neuronal dysfunction in Alzheimer's disease: From synapses toward neural networks. *Nat. Neurosci.* **2010**, *13*, 812–818.

73. Wang, Y.; Zhou, H.; Zhou, X. Clearance of amyloid-beta in Alzheimer's disease: progress, problems and perspectives. *Drug Discov. Today* **2006**, *11*, 931–938.

74. Xiang, Y.; Bu, X.; Liu, Y.; Zhu, C.; Shen, L.; Jiao, S.; Zhu, X.; Giunta, B.; Tan, J.; Song, W.; Zhou, H.; Zhou, X.; Wang, Y. Physiological amyloid-beta clearance in the periphery and its therapeutic potential for Alzheimer’s disease. *Acta Neuropathol.* **2015**, *130*, 487–499.

75. Zhang-Nunes, S. X.; Maat-Schieman, M. L.; van Duinen, S. G.; Roos, R. A.; Frosch, M. P.; Greenberg, S. M. The cerebral beta-amyloid angiopathies: hereditary and sporadic. *Brain Pathol.* **2006**, *16*, 30–39.

76. Citron, M.; Oltersdorf, T.; Haass, C.; McConlogue, L.; Hung, A. Y.; Seubert, P.; Vigo-Pelfrey, C.; Lieberburg, I.; Selkoe, D. J. Mutation of the ß-amyloid precursor protein in familial Alzheimer's disease increases ß-protein production. *Nature* **1992**, *360*, 672–674.

77. Shepherd, C.; McCann, H.; Halliday, G. M. Variations in the neuropathology of familial Alzheimer's disease. *Acta Neuropathol.* **2009**, *118*, 37–52.

78. Wolfe, M. S. When loss is gain: Reduced presenilin proteolytic function leads to increased Aß42/Aß40. Talking Point on the role of presenilin mutations in Alzheimer disease. *EMBO Rep.* **2007**, *8*, 136–140.

79. Houlden, H.; Baker, M.; McGowan, E.; Lewis, P.; Hutton, M.; Crook, R.; Wood, N. W.; Kumar-Singh, S.; Geddes, J.; Swash, M.; Scaravilli, F.; Holton, J. L.; Lashley, T.; Tomita, T.; Hashimoto, T.; Verkkoniemi, A.; Kalimo, H.; Somer, M.; Paetau, A.; Martin, J. -.; Van Broeckhoven, C.; Golde, T.; Hardy, J.; Haltia, M.; Revesz, T. Variant Alzheimer's disease with spastic paraparesis and cotton wool plaques is caused by PS-1 mutations that lead to exceptionally high amyloid-ß concentrations. *Ann. Neurol.* **2000**, *48*, 806–808.

80. Näslund, J.; Schierhorn, A.; Hellman, U.; Lannfelt, L.; Roses, A. D.; Tjernberg, L. O.; Silberring, J.; Gandy, S. E.; Winblad, B.; Greengard, P.; Nordstedt, C.; Terenius, L. Relative abundance of Alzheimer Aß amyloid peptide variants in Alzheimer disease and normal aging. *Proc. Natl. Acad. Sci. U. S. A.* **1994**, *91*, 8378–8382.

81. Miklossy, J.; Taddei, K.; Suva, D.; Verdile, G.; Fonte, J.; Fisher, C.; Gnjec, A.; Ghika, J.; Suard, F.; Mehta, P. D.; McLean, C. A.; Masters, C. L.; Brooks, W. S.; Martins, R. N. Two novel presenilin-1 mutations (Y256S and Q222H) are associated with early-onset Alzheimer's disease. *Neurobiol. Aging* **2003**, *24*, 655–662.

82. Corder, E. H.; Saunders, A. M.; Strittmatter, W. J.; Schmechel, D. E.; Gaskell, P. C.; Small, G. W.; Roses, A. D.; Haines, J. L.; Pericak-Vance, M. A. Gene dose of apolipoprotein E type 4 allele and the risk of Alzheimer's disease in late onset families. *Science* **1993**, *261*, 921–923.

83. Saunders, A. M.; Strittmatter, W. J.; Schmechel, D.; St. George-Hyslop, P. H.; Pericak-Vance, M. A.; Joo, S. H.; Rosi, B. L.; Gusella, J. F.; Crapper-Mac Lachlan, D. R.; Alberts, M. J.; Hulette, C.; Crain, B.; Goldgaber, D.; Roses, A. D. Association of apolipoprotein E allele ϵ4 with late-onset familial and sporadic Alzheimer’s disease. *Neurology* **1993**, *43*, 1467–1472.

84. Gatz, M.; Reynolds, C. A.; Fratiglioni, L.; Johansson, B.; Mortimer, J. A.; Berg, S.; Fiske, A.; Pedersen, N. L. Role of genes and environments for explaining Alzheimer disease. *Arch. Gen. Psychiatry* **2006**, *63*, 168–174.

85. Mahley, R. W. Central nervous system lipoproteins: ApoE and regulation of cholesterol metabolism. *Arterioscler. Thromb. Vasc. Biol.* **2016**, *36*, 1305–1315.

86. Yassine, H. N.; Braskie, M. N.; Mack, W. J.; Castor, K. J.; Fonteh, A. N.; Schneider, L. S.; Harrington, M. G.; Chui, H. C. Association of docosahexaenoic acid supplementation with Alzheimer disease stage in Apolipoprotein e ϵ4 carriers: A review. *JAMA Neurol.* **2017**, *74*, 339–347.

87. Poirier, J.; Miron, J.; Picard, C.; Gormley, P.; Théroux, L.; Breitner, J.; Dea, D. Apolipoprotein E and lipid homeostasis in the etiology and treatment of sporadic Alzheimer's disease. *Neurobiol. Aging* **2014***, 35*, S3–S10.

88. Grimm, M. O. W.; Zimmer, V. C.; Lehmann, J.; Grimm, H. S.; Hartmann, T. The impact of cholesterol, DHA, and sphingolipids on Alzheimer's disease. *BioMed Res. Int.* **2013***, 2013*.

89. Harris, J. R.; Milton, N. G. N. Cholesterol in Alzheimer's disease and other amyloidogenic disorders. *Sub-Cell. Biochem.* **2010***, 51*, 47–75.

90. Kawas, C. H.; Corrada, M. M. Alzheimer's and dementia in the oldest-old: A century of challenges. *Curr. Alzheimer Res.* **2006***, 3*, 411–419.

91. Kivipelto, M.; Ngandu, T.; Fratiglioni, L.; Viitanen, M.; Kåreholt, I.; Winblad, B.; Helkala, E.; Tuomilehto, J.; Soininen, H.; Nissinen, A. Obesity and vascular risk factors at midlife and the risk of dementia and Alzheimer disease. *Arch. Neurol.* **2005***, 62*, 1556–1560.

92. Qiu, C.; Winblad, B.; Marengoni, A.; Klarin, I.; Fastbom, J.; Fratiglioni, L. Heart failure and risk of dementia and Alzheimer disease: A population-based cohort study. *Arch. Intern. Med.* **2006***, 166*, 1003–1008.

93. Fratiglioni, L.; Paillard-Borg, S.; Winblad, B. An active and socially integrated lifestyle in late life might protect against dementia. *Lancet Neurol.* **2004***, 3*, 343–353.

94. Guo, Z.; Cupples, L. A.; Kurz, A.; Auerbach, S. H.; Volicer, L.; Chui, H.; Green, R. C.; Sadovnick, A. D.; Duara, R.; DeCarli, C.; Johnson, K.; Go, R. C.; Growdon, J. H.; Haines, J.

L.; Kukull, W. A.; Farrer, L. A. Head injury and the risk of AD in the MIRAGE study. *Neurology* **2000***, 54*, 1316–1323.

95. Duron, E.; Hanon, O. Atrial fibrillation and cognitive function. *Psychol. Neuropsychiatr. Vieil.* **2010***, 8*, 209–214.

96. Engelhart, M. J.; Geerlings, M. I.; Meijer, J.; Kiliaan, A.; Ruitenberg, A.; Van Swieten, J. C.; Stijnen, T.; Hofman, A.; Witteman, J. C. M.; Breteler, M. M. B. Inflammatory proteins in plasma and the risk of dementia: the Rotterdam study. *Arch. Neurol.* **2004***, 61*, 668–672.

97. Bots, M. L.; Breteler, M. M. B.; Van Kooten, F.; Haverkate, F.; Meijer, P.; Koudstaal, P. J.; Grobbee, D. E.; Kluft, C. Coagulation and fibrinolysis markers and risk of dementia. *Haemostasis* **1998***, 28*, 216–222.

98. Kalmijn, S.; Launer, L. J.; Lindemans, J.; Bots, M. L.; Hofman, A.; Breteler, M. M. B. Total homocysteine and cognitive decline in a community-based sample of elderly subjects: The Rotterdam study. *Am. J. Epidemiol.* **1999***, 150*, 283–289.

99. Luchsinger, J. A.; Mayeux, R. Dietary factors and Alzheimer's disease. *Lancet Neurol.* **2004***, 3*, 579–587.

100. Tyas, S. L.; Manfreda, J.; Strain, L. A.; Montgomery, P. R. Risk factors for Alzheimer's disease: A population-based, longitudinal study in Manitoba, Canada. *Int. J. Epidemiol.* **2001***, 30*, 590–597.

101. Atri, A. The Alzheimer's disease clinical spectrum: diagnosis and management. *Med. Clin. North Am.* **2019***, 103*, 263–293.

102. McKhann, G. M.; Knopman, D. S.; Chertkow, H.; Hyman, B. T.; Jack Jr., C. R.; Kawas, C. H.; Klunk, W. E.; Koroshetz, W. J.; Manly, J. J.; Mayeux, R.; Mohs, R. C.; Morris, J. C.; Rossor, M. N.; Scheltens, P.; Carrillo, M. C.; Thies, B.; Weintraub, S.; Phelps, C. H. The diagnosis of dementia due to Alzheimer's disease: recommendations from the National Institute on Aging-Alzheimer's Association workgroups on diagnostic guidelines for Alzheimer's disease. *Alzheimer's Dementia* **2011***, 7*, 263–269.

103. Lalkhen, A. G.; McCluskey, A. Clinical tests: Sensitivity and specificity. *Contin. Educ. Anaesth. Crit. Care Pain* **2008***, 8*, 221–223.

104. Knopman, D. S.; DeKosky, S. T.; Cummings, J. L.; Chui, H.; Corey-Bloom, J.; Relkin, N.; Small, G. W.; Miller, B.; Stevens, J. C. Practice parameter: Diagnosis of dementia (an evidence-based review): Report of the quality standards subcommittee of the American academy of neurology. *Neurology* **2001***, 56*, 1143–1153.

105. Nasreddine, Z. S.; Phillips, N. A.; Bédirian, V.; Charbonneau, S.; Whitehead, V.; Collin, I.; Cummings, J. L.; Chertkow, H. The Montreal Cognitive Assessment, MoCA: A brief screening tool for mild cognitive impairment. *J. Am. Geriatr. Soc.* **2005***, 53*, 695–699.

106. Sikkes, S. A. M.; De Lange-De Klerk, E S M; Pijnenburg, Y. A. L.; Scheltens, P.; Uitdehaag, B. M. J. A systematic review of Instrumental Activities of Daily Living scales in dementia: Room for improvement. *J. Neurol. Neurosurg. Psychiatry* **2009***, 80*, 7–12.

107. Sarazin, M.; Berr, C.; De Rotrou, J.; Fabrigoule, C.; Pasquier, F.; Legrain, S.; Michel, B.; Puel, M.; Volteau, M.; Touchon, J.; Verny, M.; Dubois, B. Amnestic syndrome of the medial

temporal type identifies prodromal AD: A longitudinal study. *Neurology* **2007***, 69*, 1859–1867.

108. Sharma, N.; Singh, A. N. Exploring biomarkers for Alzheimer’s disease. *J. Clin. Diagn. Res.* **2016***, 10*, KE01–KE06.

109. Blennow, K.; Zetterberg, H. Biomarkers for Alzheimer's disease: current status and prospects for the future. *J. Intern. Med. (GBR)* **2018***, 284*, 643–663.

110. Visser, P. J.; Verhey, F.; Knol, D. L.; Scheltens, P.; Wahlund, L. -.; Freund-Levi, Y.; Tsolaki, M.; Minthon, L.; Wallin, A. K.; Hampel, H.; Bürger, K.; Pirttila, T.; Soininen, H.; Rikkert, M. O.; Verbeek, M. M.; Spiru, L.; Blennow, K. Prevalence and prognostic value of CSF markers of Alzheimer's disease pathology in patients with subjective cognitive impairment or mild cognitive impairment in the DESCRIPA study: a prospective cohort study. *Lancet Neurol.* **2009***, 8*, 619–627.

111. Shaw, L. M.; Vanderstichele, H.; Knapik-Czajka, M.; Clark, C. M.; Aisen, P. S.; Petersen, R. C.; Blennow, K.; Soares, H.; Simon, A.; Lewczuk, P.; Dean, R.; Siemers, E.; Potter, W.; Lee, V. M. Y.; Trojanowski, J. Q. Cerebrospinal fluid biomarker signature in alzheimer's disease neuroimaging initiative subjects. *Ann. Neurol.* **2009***, 65*, 403–413.

112. Buerger, K.; Ewers, M.; Pirttilä, T.; Zinkowski, R.; Alafuzoff, I.; Teipel, S. J.; DeBernardis, J.; Kerkman, D.; McCulloch, C.; Soininen, H.; Hampel, H. CSF phosphorylated tau protein correlates with neocortical neurofibrillary pathology in Alzheimer's disease. *Brain* **2006***, 129*, 3035–3041.

113. Skillbäck, T.; Rosén, C.; Asztely, F.; Mattsson, N.; Blennow, K.; Zetterberg, H. Diagnostic performance of cerebrospinal fluid total tau and phosphorylated tau in Creutzfeldt-Jakob disease: Results from the Swedish Mortality Registry. *JAMA Neurol.* **2014***, 71*, 476–483.

114. Blennow, K. CSF biomarkers for mild cognitive impairment. *J. Intern. Med. (GBR)* **2004***, 256*, 224–234.

115. Nakamura, T.; Shoji, M.; Harigaya, Y.; Watanabe, M.; Hosoda, K.; Cheung, T. T.; Shaffer, L. M.; Golde, T. E.; Younkin, L. H.; Younkin, S. G.; Hirai, S. Amyloid ß protein levels in cerebrospinal fluid are elevated in early-onset Alzheimer's disease. *Ann. Neurol.* **1994***, 36*, 903–911.

116. Motter, R.; Vigo-Pelfrey, C.; Kholodenko, D.; Barbour, R.; Johnson-Wood, K.; Galasko, D.; Chang, L.; Miller, B.; Clark, C.; Green, R.; Olson, D.; Southwick, P.; Wolfert, R.; Munroe, B.; Lieberburg, I.; Seubert, P.; Schenk, D. Reduction of ß-amyloid peptide42 in the cerebrospinal fluid of patients with Alzheimer's disease. *Ann. Neurol.* **1995***, 38*, 643–648.

117. Strozyk, D.; Blennow, K.; White, L. R.; Launer, L. J. CSF Aß 42 levels correlate with amyloid-neuropathology in a population-based autopsy study. *Neurology* **2003***, 60*, 652–656.

118. Lewczuk, P.; Lelental, N.; Spitzer, P.; Maler, J. M.; Kornhuber, J. Amyloid-ß 42/40 cerebrospinal fluid concentration ratio in the diagnostics of Alzheimer's disease: Validation of two novel assays. *J. Alzheimer's Dis.* **2014***, 43*, 183–191.

119. Cui, J.; Zufferey, V.; Kherif, F. In vivo brain neuroimaging provides a gateway for integrating biological and clinical biomarkers of Alzheimer's disease. *Curr. Opin. Neurol.* **2015***, 28*, 351–357.

120. Prvulovic, D.; Hampel, H. Amyloid ß (Aß) and phospho-tau (p-tau) as diagnostic biomarkers in Alzheimer's disease. *Clin. Chem. Lab. Med.* **2011***, 49*, 367–374.

121. Burton, E. J.; Barber, R.; Mukaetova-Ladinska, E. B.; Robson, J.; Perry, R. H.; Jaros, E.; Kalaria, R. N.; O'Brien, J. T. Medial temporal lobe atrophy on MRI differentiates Alzheimer's disease from dementia with Lewy bodies and vascular cognitive impairment: A prospective study with pathological verification of diagnosis. *Brain* **2009***, 132*, 195–203.

122. McNeill, R.; Sare, G. M.; Manoharan, M.; Testa, H. J.; Mann, D. M. A.; Neary, D.; Snowden, J. S.; Varma, A. R. Accuracy of single-photon emission computed tomography in differentiating frontotemporal dementia from Alzheimer's disease. *J. Neurol. Neurosurg. Psychiatry* **2007***, 78*, 350–355.

123. Bohnen, N. I.; Djang, D. S. W.; Herholz, K.; Anzai, Y.; Minoshima, S. Effectiveness and safety of 18F-FDG PET in the evaluation of dementia: A review of the recent literature. *J. Nucl. Med.* **2012***, 53*, 59–71.

124. Prvulovic, D.; Hampel, H. Amyloid ß (Aß) and phospho-tau (p-tau) as diagnostic biomarkers in Alzheimer's disease. *Clin. Chem. Lab. Med.* **2011***, 49*, 367–374.

125. Crump, C. J.; Johnson, D. S.; Li, Y. Development and mechanism of γ-secretase modulators for Alzheimer's disease. *Biochemistry* **2013***, 52*, 3197–3216.

126. Weggen, S.; Eriksen, J. L.; Das, P.; Sagi, S. A.; Wang, R.; Pietrzik, C. U.; Findlay, K. A.; Smith, T. E.; Murphy, M. P.; Bulter, T.; Kang, D. E.; Marquez-Sterling, N.; Golde, T. E.; Koo, E. H. A subset of NSAIDs lower amyloidogenic Aß42 independently of cyclooxygenase activity. *Nature* **2001***, 414*, 212–216.

127. Bieschke, J.; Herbst, M.; Wiglenda, T.; Friedrich, R. P.; Boeddrich, A.; Schiele, F.; Kleckers, D.; Lopez Del Amo, J M; Grüning, B. A.; Wang, Q.; Schmidt, M. R.; Lurz, R.; Anwyl, R.; Schnoegl, S.; Fändrich, M.; Frank, R. F.; Reif, B.; Günther, S.; Walsh, D. M.; Wanker, E. E. Small-molecule conversion of toxic oligomers to nontoxic ß-sheet g-rich amyloid fibrils. *Nat. Chem. Biol.* **2012***, 8*, 93–101.

128. Butini, S.; Guarino, E.; Campiani, G.; Brindisi, M.; Coccone, S. S.; Fiorini, I.; Novellino, E.; Belinskaya, T.; Saxena, A.; Gemma, S. Tacrine based human cholinesterase inhibitors: Synthesis of peptidic-tethered derivatives and their effect on potency and selectivity. *Bioorg. Med. Chem. Lett.* **2008***, 18*, 5213–5216.

129. Sterling, J.; Herzig, Y.; Goren, T.; Finkelstein, N.; Lerner, D.; Goldenberg, W.; Miskolczi, I.; Molnar, S.; Rantal, F.; Tamas, T.; Toth, G.; Zagyva, A.; Zekany, A.; Lavian, G.; Gross, A.; Friedman, R.; Razin, M.; Huang, W.; Krais, B.; Chorev, M.; Youdim, M. B.; Weinstock, M. Novel dual inhibitors of AChE and MAO derived from hydroxy aminoindan and phenethylamine as potential treatment for Alzheimer's disease. *J. Med. Chem.* **2002***, 45*, 5260–5279.

130. Greenblatt, H. M.; Guillou, C.; Guénard, D.; Argaman, A.; Botti, S.; Badet, B.; Thal, C.; Silman, I.; Sussman, J. L. The complex of a bivalent derivative of galanthamine with Torpedo

acetylcholinesterase displays drastic deformation of the active-site gorge: Implications for structure-based drug design. *J. Am. Chem. Soc.* **2004***, 126*, 15405–15411.

131. Habtemariam, S. Natural products in Alzheimer's disease therapy: Would old therapeutic approaches fix the broken promise of modern medicines? *Molecules* **2019***, 24*.

132. Yanagisawa, D.; Taguchi, H.; Yamamoto, A.; Shirai, N.; Hirao, K.; Tooyama, I. Curcuminoid binds to amyloid-ß1-42 oligomer and fibril. *J. Alzheimer's Dis.* **2011***, 24*, 33–42.

133. Lim, G. P.; Chu, T.; Yang, F.; Beech, W.; Frautschy, S. A.; Cole, G. M. The curry spice curcumin reduces oxidative damage and amyloid pathology in an Alzheimer transgenic mouse. *J. Neurosci.* **2001***, 21*, 8370–8377.

134. Baur, J. A.; Sinclair, D. A. Therapeutic potential of resveratrol: The in vivo evidence. *Nat. Rev. Drug Discov.* **2006***, 5*, 493–506.

135. Huang, T.; Lu, K.; Wo, Y. P.; Wu, Y.; Yang, Y. Resveratrol protects rats from Aß-induced neurotoxicity by the reduction of iNOS expression and lipid peroxidation. *PLoS ONE* **2011***, 6*, e29102.

136. Lee, Y.; Lee, Y. M.; Lee, C.; Jung, J. K.; Han, S. B.; Hong, J. T. Therapeutic applications of compounds in the Magnolia family. *Pharmacol. Ther.* **2011***, 130*, 157–176.

137. Kim, B. H.; Cho, J. Y. Anti-inflammatory effect of honokiol is mediated by PI3K/Akt pathway suppression. *Acta Pharmacol. Sin.* **2008***, 29*, 113–122.

138. Xu, Q.; Yi, L.; Pan, Y.; Wang, X.; Li, Y.; Li, J.; Wang, C.; Kong, L. Antidepressant-like effects of the mixture of honokiol and magnolol from the barks of Magnolia officinalis in stressed rodents. *Prog. Neuro-Psychopharmacol. Biol. Psychiatry* **2008**, *32*, 715–725.

139. Kuribara, H.; Kishi, E.; Kimura, M.; Weintraub, S. T.; Maruyama, Y. Comparative assessment of the anxiolytic-like activities of honokiol and derivatives. *Pharmacol. Biochem. Behav.* **2000**, *67*, 597–601.

140. Cui, H. S.; Huang, L. S.; Sok, D.; Shin, J.; Kwon, B.; Youn, U. J.; Bae, K. Protective action of honokiol, administered orally, against oxidative stress in brain of mice challenged with NMDA. *Phytomedicine* **2007**, *14*, 696–700.

141. Hoi, C. P.; Ho, Y. P.; Baum, L.; Chow, A. H. L. Neuroprotective effect of honokiol and magnolol, compounds from Magnolia officinalis, on beta-amyloid-induced toxicity in PC12 cells. *Phytother. Res.* **2010**, *24*, 1538–1542.

142. Lin, Y.; Chen, H.; Ko, C.; Chan, M. Neuroprotective activity of honokiol and magnolol in cerebellar granule cell damage. *Eur. J. Pharmacol.* **2006**, *537*, 64–69.

143. Liou, K.; Shen, Y.; Chen, C.; Tsao, C.; Tsai, S. Honokiol protects rat brain from focal cerebral ischemia-reperfusion injury by inhibiting neutrophil infiltration and reactive oxygen species production. *Brain Res.* **2003**, *992*, 159–166.

144. Wang, X.; Duan, X.; Yang, G.; Zhang, X.; Deng, L.; Zheng, H.; Deng, C.; Wen, J.; Wang, N.; Peng, C.; Zhao, X.; Wei, Y.; Chen, L. Honokiol crosses BBB and BCSFB, and inhibits

brain tumor growth in rat 9l intracerebral gliosarcoma model and human U251 xenograft glioma model. *PLoS ONE* **2011**, *6*, e18490.

145. Jain, Z. J.; Gide, P. S.; Kankate, R. S. Biphenyls and their derivatives as synthetically and pharmacologically important aromatic structural moieties. *Arab. J. Chem.* **2017**, *10*, S2051–S2066.

146. McMurray, J. J. V.; Packer, M.; Desai, A. S.; Gong, J.; Lefkowitz, M. P.; Rizkala, A. R.; Rouleau, J.; Shi, V. C.; Solomon, S. D.; Swedberg, K.; Zile, M. R. Dual angiotensin receptor and neprilysin inhibition as an alternative to angiotensin-converting enzyme inhibition in patients with chronic systolic heart failure: Rationale for and design of the Prospective comparison of ARNI with ACEI to Determine Impact on Global Mortality and morbidity in Heart Failure trial (PARADIGM-HF). *Eur. J. Heart Fail.* **2013**, *15*, 1062–1073.

147. Coskun, G. P.; Djikic, T.; Hayal, T. B.; Türkel, N.; Yelekçi, K.; Sahin, F.; Küçükgüzel, S. G. Synthesis, molecular docking and anticancer activity of diflunisal derivatives as cyclooxygenase enzyme inhibitors. *Molecules* **2018**, *23*, E1969.

148. Uusi-Oukari, M.; Vähätalo, L.; Liljeblad, A. Modifications of diflunisal and meclofenamate carboxyl groups affect their allosteric effects on GABAA receptor ligand binding. *Neurochem. Res.* **2014**, *39*, 1183–1191.

149. Albertsson, A.; Varma, I. K. Recent developments in ring opening polymerization of lactones for biomedical applications. *Biomacromolecules* **2003**, *4*, 1466–1486.

150. Stevens, C. B.; Hanna Jr., J. M.; Lammi, R. K. Synthesis of tetrahydroxybiphenyls and tetrahydroxyterphenyls and their evaluation as amyloid-ß aggregation inhibitors. *Bioorg. Med. Chem. Lett.* **2013***, 23*, 1703–1706.

151. García-López, J.; Greaney, M. F. Synthesis of biaryls using aryne intermediates. *Chem. Soc. Rev.* **2016***, 45*, 6766–6798.

152. Deep, A.; Jain, S.; Sharma, P. C.; Mittal, S. K.; Phogat, P.; Malhotra, M. Synthesis, characterization and antimicrobial evaluation of 2,5-disubstituted-4-thiazolidinone derivatives. *Arab. J. Chem.* **2014***, 7*, 287–291.

153. Deep, A.; Jain, S.; Sharma, P. C.; Verma, P.; Kumar, M.; Dora, C. P. Design and biological evaluation of biphenyl-4-carboxylic acid hydrazide-hydrazone for antimicrobial activity. *Acta Pol. Pharm. Drug Res.* **2010***, 67*, 255–259.

154. Ervin, K. M.; Gilles, M. K.; Bierbaum, V. M.; Lineberger, W. C.; Barney Ellison, G.; Gronert, S.; Barlow, S. E.; Harrison, A. G.; DePuy, C. H.; Harrison, A. G. Bond strengths of ethylene and acetylene. *J. Am. Chem. Soc.* **1990***, 112*, 5750–5759.

155. Rossi, R.; Carpita, A.; Lezzi, A. Palladium-catalyzed syntheses of naturally-occurring acetylenic thiophens and related compounds. *Tetrahedron* **1984***, 40*, 2773–2779.

156. Wade, A.; Symons, A. M.; Martin, L.; Parke, D. V. Metabolic oxidation of the ethynyl group in 4 ethynylbiphenyl. *Biochem. J.* **1979***, 184*, 509–517.

157. White, I. N. H. Suicidal destruction of cytochrome P-450 by ethynyl substituted compounds. *Pharm. Res.* **1984***, 1*, 141–148.

158. Saxena, J.; Meloni, D.; Huang, M.; Heck, D. E.; Laskin, J. D.; Heindel, N. D.; Young, S. C. Ethynylphenyl carbonates and carbamates as dual-action acetylcholinesterase inhibitors and anti-inflammatory agents. *Bioorg. Med. Chem. Lett.* **2015***, 25*, 5609–5612.

159. Wilcken, R.; Zimmermann, M. O.; Bauer, M. R.; Rutherford, T. J.; Fersht, A. R.; Joerger, A. C.; Boeckler, F. M. Experimental and theoretical evaluation of the ethynyl moiety as a halogen bioisostere. *ACS Chem. Biol.* **2015***, 10*, 2725–2732.

160. Chan, K.; Jensen, N. S.; Silber, P. M.; O'Brien, P. J. Structure-activity relationships for halobenzene induced cytotoxicity in rat and human hepatoctyes. *Chem.-Biol. Interact.* **2007***, 165*, 165–174.

161. Park, J. H.; Liu, Y.; Lemmon, M. A.; Radhakrishnan, R. Erlotinib binds both inactive and active conformations of the EGFR tyrosine kinase domain. *Biochem. J.* **2012***, 448*, 417–423.

162. Rankovic, Z. CNS drug design: balancing physicochemical properties for optimal brain exposure. *J. Med. Chem.* **2015***, 58*, 2584–2608.

163. Lipinski, C. A.; Lombardo, F.; Dominy, B. W.; Feeney, P. J. Experimental and computational approaches to estimate solubility and permeability in drug discovery and development settings. *Adv. Drug Deliv. Rev.* **1997***, 23*, 3–25.

164. Leeson, P. D.; Young, R. J. Molecular property design: does everyone get it? *ACS Med. Chem. Lett.* **2015***, 6*, 722–725.

165. Shultz, M. D. Two decades under the influence of the rule of five and the changing properties of approved oral drugs. *J. Med. Chem.* **2019***, 62*, 1701–1714.

166. Pajouhesh, H.; Lenz, G. R. Medicinal chemical properties of successful central nervous system drugs. *NeuroRx* **2005***, 2*, 541–553.

167. DeRuiter, J. Alkynes. *Principles of Drug Action 1,* 2005; pp 1–6.

168. Strotman, N. A.; Chobanian, H. R.; He, J.; Guo, Y.; Dormer, P. G.; Jones, C. M.; Steves, J. E. Catalyst-controlled regioselective suzuki couplings at both positions of dihaloimidazoles, dihalooxazoles, and dihalothiazoles. *J. Org. Chem.* **2010***, 75*, 1733–1739.

169. Morri, A. K.; Thummala, Y.; Doddi, V. R. The Dual Role of 1,8-Diazabicyclo[5.4.0]undec-7-ene (DBU) in the Synthesis of Terminal Aryl- and Styryl-Acetylenes via Umpolung Reactivity. *Org. Lett.* **2015***, 17*, 4640–4643.

170. Zhao, M.; Kuang, C.; Yang, Q.; Cheng, X. Cs2CO3-mediated synthesis of terminal alkynes from 1,1-dibromo-1-alkenes. *Tetrahedron Lett.* **2011***, 52*, 992–994.

171. Pearson, D. L.; Tour, J. M. Rapid syntheses of oligo(2,5-thiophene ethynylene)s with thioester termini: potential molecular scale wires with alligator clips. *J. Org. Chem.* **1997***, 62*, 1376–1387.

172. Tilley, J. W.; Zawoiski, S. A convenient palladium-catalyzed coupling approach to 2,5-disubstituted pyridines. *J. Org. Chem.* **1988***, 53*, 386–390.

173. Hudson, S. A.; Ecroyd, H.; Kee, T. W.; Carver, J. A. The thioflavin T fluorescence assay for amyloid fibril detection can be biased by the presence of exogenous compounds. *FEBS J.* **2009***, 276*, 5960-5972.

174. Zhao, D.; Chen, Y.; Liu, Q.; Zhao, Y.; Li, Y. Exploring the binding mechanism of thioflavin-T to the ß-amyloid peptide by blind docking method. *Sci. China Chem.* **2012***, 55*, 112–117.

175. Paredes, A. M. Microscopy: transmission electron microscopy. In encyclopedia of food microbiology: Second edition, 2014; pp 711–720.

176. Curtis, S. W.; Conneely, K. N.; Marder, M. E.; Terrell, M. L.; Marcus, M.; Smith, A. K. Intergenerational effects of endocrine-disrupting compounds: A review of the Michigan polybrominated biphenyl registry. *Epigenomics* **2018***, 10*, 845–858.

177. Hens, B.; Hens, L. Persistent threats by persistent pollutants: Chemical nature, concerns and future policy regarding PCBs—What are we heading for? *Toxics* **2017***, 6*, 1–21.

178. Cámara, B.; Herrera, C.; Gonzalez, M.; Couve, E.; Hofer, B.; Seeger, M. From PCBs to highly toxic metabolites by the biphenyl pathway. *Environ. Microbiol.* **2004***, 6*, 842–850.

179. Paravastu, A. K.; Leapman, R. D.; Yau, W.; Tycko, R. Molecular structural basis for polymorphism in Alzheimer's ß-amyloid fibrils. *Proc. Natl. Acad. Sci. U. S. A.* **2008***, 105*, 18349–18354.

180. Wälti, M. A.; Ravotti, F.; Arai, H.; Glabe, C. G.; Wall, J. S.; Böckmann, A.; Güntert, P.; Meier, B. H.; Riek, R. Atomic-resolution structure of a disease-relevant Aß(1-42) amyloid fibril. *Proc. Natl. Acad. Sci. U. S. A.* **2016***, 113*, E4976–E4984.

181. Colvin, M. T.; Silvers, R.; Ni, Q. Z.; Can, T. V.; Sergeyev, I.; Rosay, M.; Donovan, K. J.; Michael, B.; Wall, J.; Linse, S.; Griffin, R. G. Atomic resolution structure of monomorphic Aß42 amyloid fibrils. *J. Am. Chem. Soc.* **2016***, 138*, 9663–9674.

182. Faroon, O.; Ruiz, P. Polychlorinated biphenyls: New evidence from the last decade. *Toxicology and Industrial Health* **2016***, 32*, 1825–1847.

183. Rao, P. P. N.; Mohamed, T.; Teckwani, K.; Tin, G. Curcumin binding to beta amyloid: A computational study. *Chem. Biol. Drug Des.* **2015***, 86*, 813–820.

Appendix – Analytical spectra for some compounds (5h and 14)

Representative ^{1}H NMR, MS and LCMS data for compound **5h** and **14.**

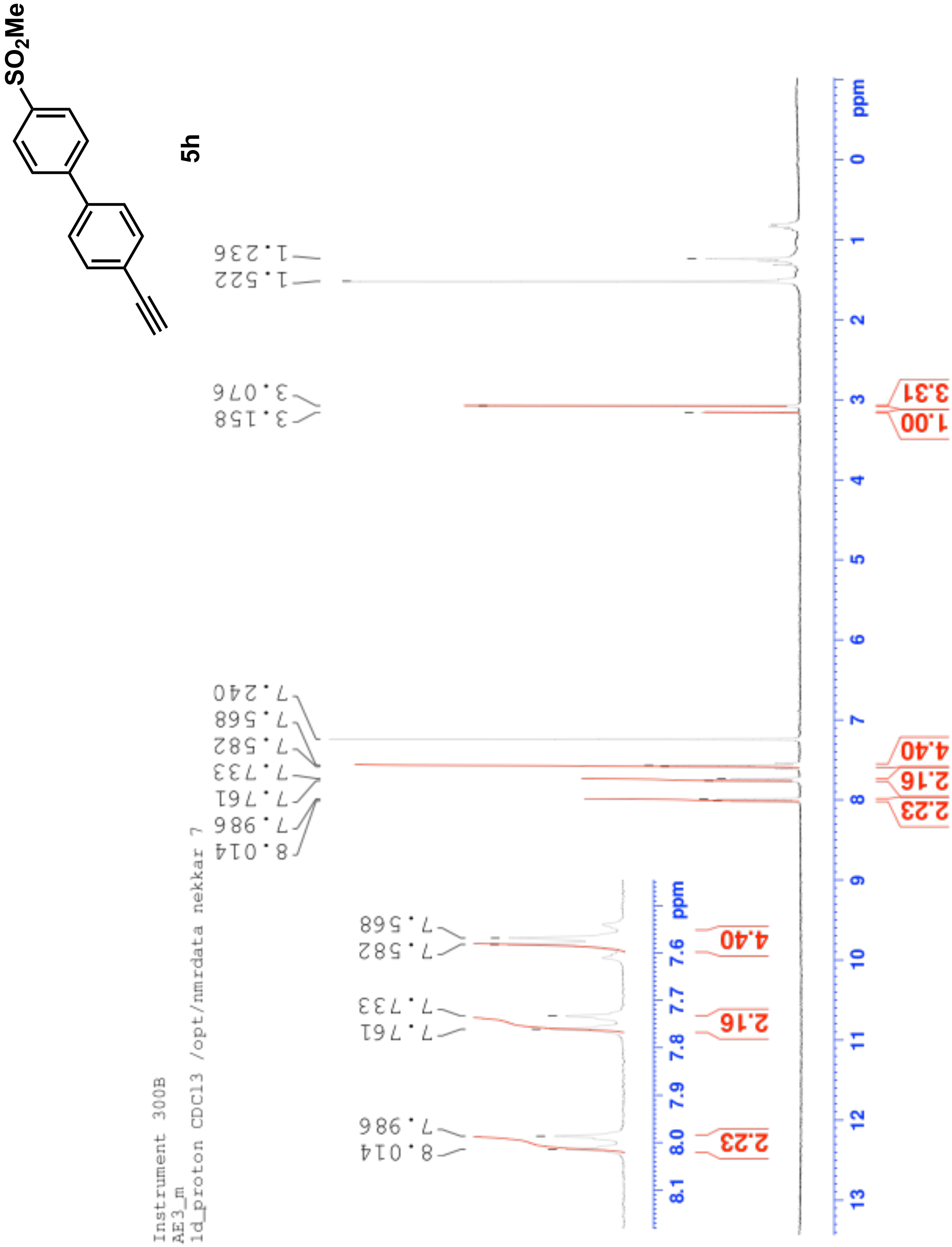

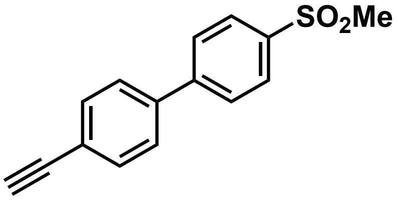

5h

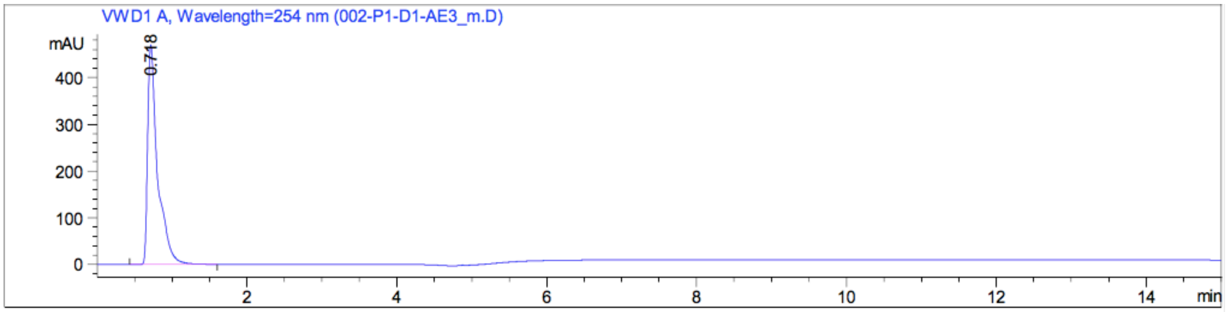

```
Peak  Ret Time  Type   Width       Area        Height       Area
  #    [min]           [min]     [mAU*s]       [mAU]          %
----|-------|----|-------|----------|----------|--------|
   1   0.718  BB     0.1322  4311.37158   469.41299  100.0000

Totals :                     4311.37158   469.41299
```

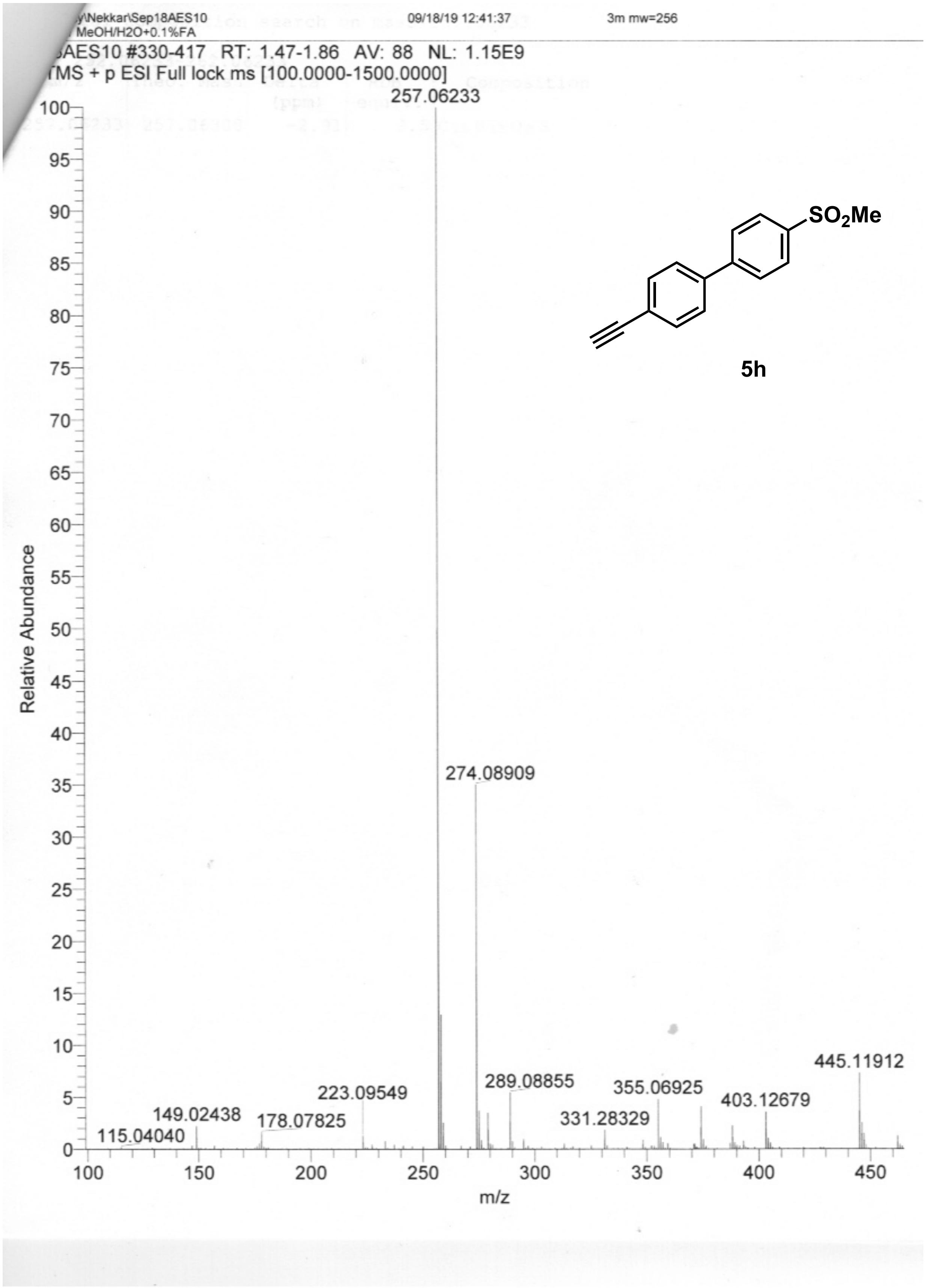
y\Nekkar\Sep18AES10
MeOH/H2O+0.1%FA
09/18/19 12:41:37
3m mw=256
3AES10 #330-417 RT: 1.47-1.86 AV: 88 NL: 1.15E9
TMS + p ESI Full lock ms [100.0000-1500.0000]
Relative Abundance
m/z
257.06233
274.08909
445.11912
355.06925
289.08855
403.12679
223.09549
331.28329
149.02438
178.07825
115.04040
SO2Me
0
5
10
15
20
25
30
35
40
45
50
55
60
65
70
75
80
85
90
95
100
100
150
200
250
300
350
400
450

5h

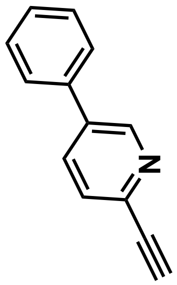

14

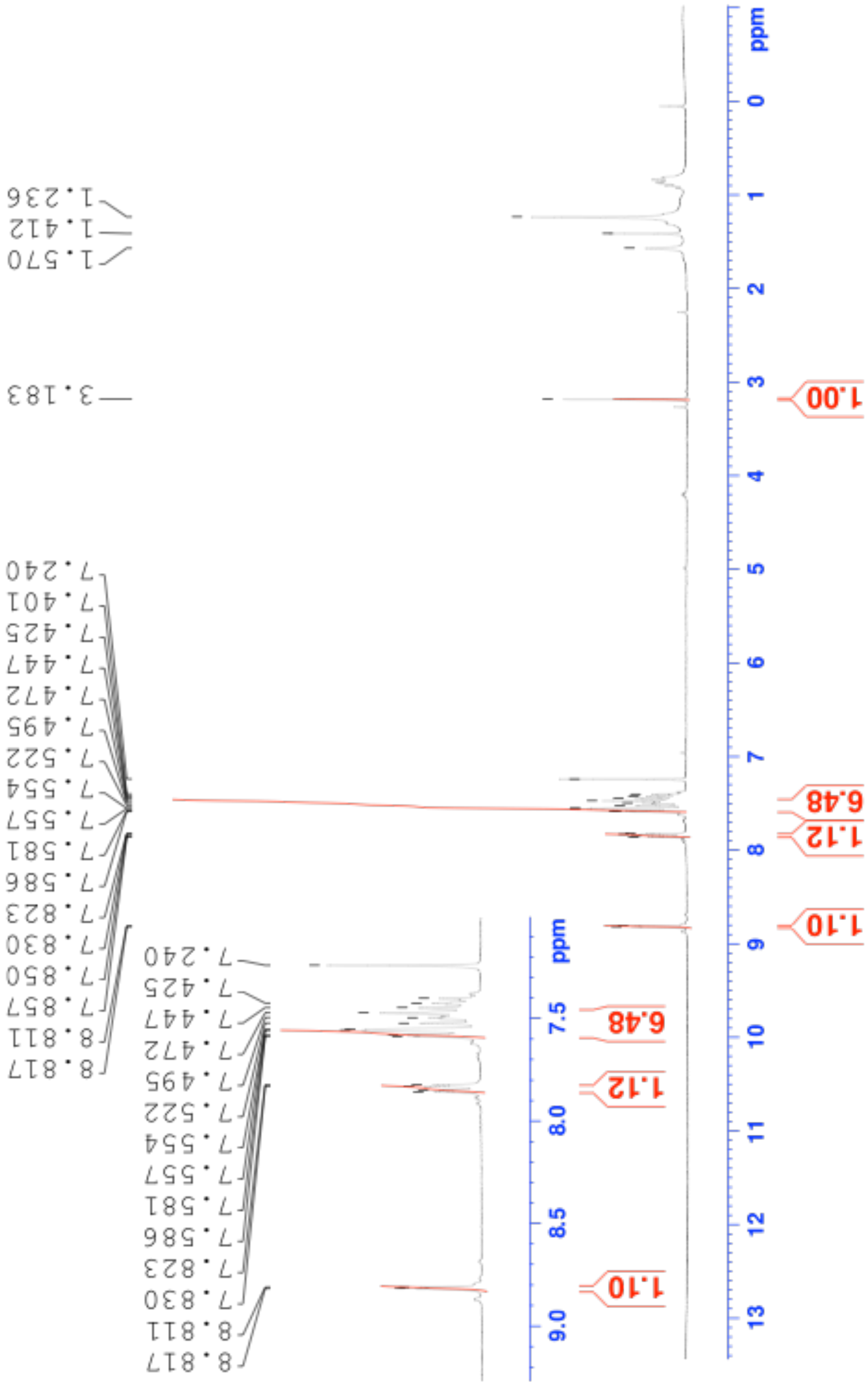

Instrument 300B
AE3_n
1d_proton CDCl3 /opt/nmrdata nekkar 13

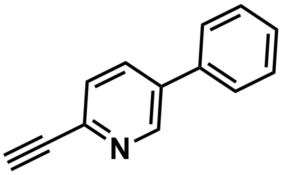

14

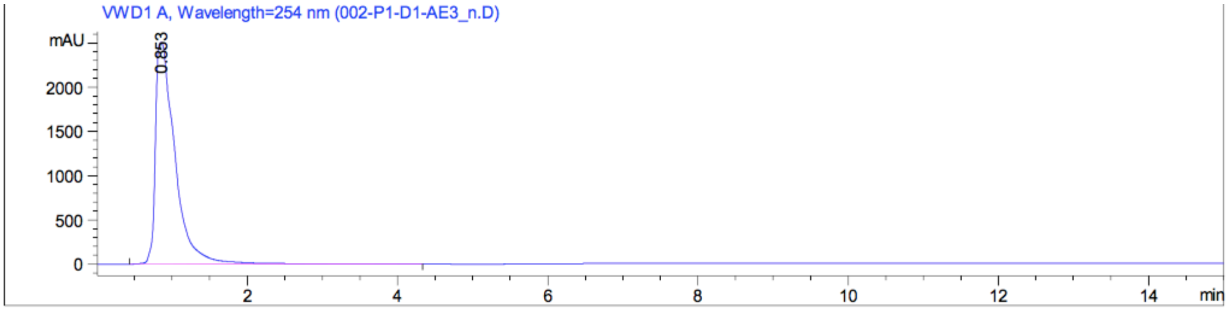

```
Signal 3: VWD1 A, Wavelength=254 nm

Peak RetTime Type  Width     Area      Height     Area
  #   [min]        [min]   [mAU*s]     [mAU]       %
----|-------|----|-------|----------|----------|--------|
   1   0.853 BB    0.2546 4.54388e4 2505.09741 100.0000

Totals :                  4.54388e4 2505.09741
```

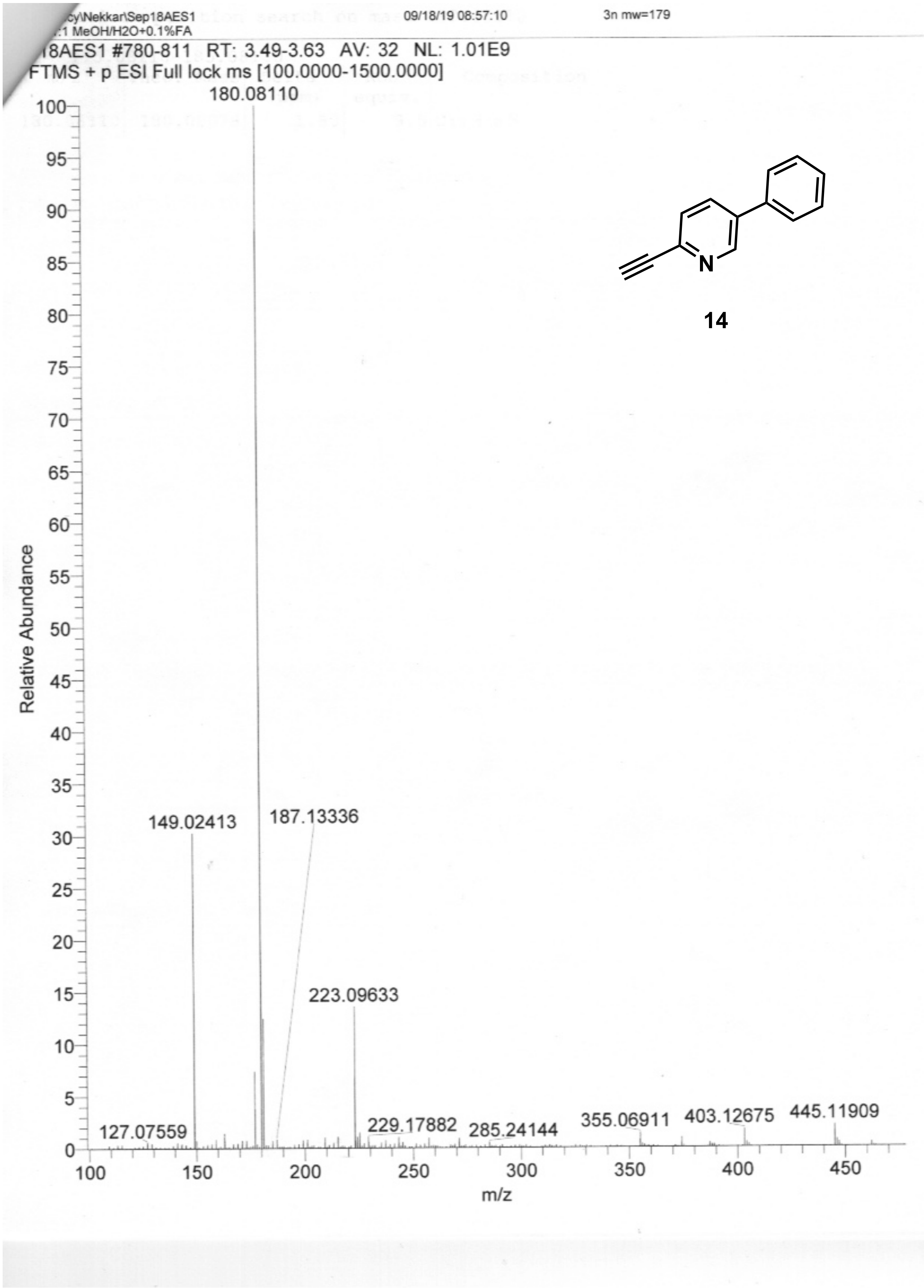

cy\Nekkar\Sep18AES1 09/18/19 08:57:10 3n mw=179

:1 MeOH/H2O+0.1%FA

18AES1 #780-811 RT: 3.49-3.63 AV: 32 NL: 1.01E9

FTMS + p ESI Full lock ms [100.0000-1500.0000]

14